The University Of Sheffield.

UNIVERSITY OF SHEFFIELD

Computational Gradient Elasticity and Gradient Plasticity with Adaptive Splines

Isa Kolo

A THESIS SUBMITTED IN PARTIAL FULFILMENT FOR THE DEGREE OF DOCTOR OF PHILOSOPHY

IN THE

DEPARTMENT OF CIVIL AND STRUCTURAL ENGINEERING

March, 2019

Computational Gradient Elasticity and Gradient Plasticity with Adaptive Splines

Isa Kolo

A thesis submitted in partial fulfillment
of the requirements for the degree of
Doctor of Philosophy

University of Sheffield
2019

ABSTRACT

Classical continuum mechanics theories are largely insufficient in capturing *size effects* observed in many engineering materials: metals, composites, rocks etc. This is attributed to the absence of a *length scale* that accounts for microstructural effects inherent in these materials. Enriching the classical theories with an internal length scale solves this problem. One way of doing this, in a theoretically sound manner, is introducing higher order gradient terms in the constitutive relations. In elasticity, introducing a length scale removes the singularity observed at crack tips using the classical theory. In plasticity, it eliminates the spurious mesh sensitivity observed in *softening* and *localisation* problems by defining the width of the localisation zone thereby maintaining a well-posed boundary value problem. However, this comes at the cost of more demanding solution techniques.

Higher-order continuity is usually required for solving *gradient-enhanced* continuum theories, a requirement difficult to meet using traditional finite elements. Hermitian finite elements, mixed methods and meshless methods have been developed to meet this requirement, however these methods have their drawbacks in terms of efficiency, robustness or implementational convenience. *Isogeometric analysis*, which exploits spline-based shape functions, naturally incorporates higher-order continuity, in addition to capturing the exact geometry and expediting the design-through-analysis process. Despite its potentials, it is yet to be fully explored for gradient-enhanced continua. Hence, this thesis develops an isogeometric analysis framework for gradient elasticity and gradient plasticity.

The linearity of the gradient elasticity formulation has enabled an operator-split approach so that instead of solving the fourth-order partial differential equation *monolithically*, a set of two partial differential equations is solved in a *staggered* manner. A detailed convergence analysis is carried out for the original system and the split set using NURBS and T-splines. Suboptimal convergence rates in the monolithic approach

and the limitations of the staggered approach are substantiated.

Another advantage of the spline-based approach adopted in this work is the ease with which different orders of interpolation can be achieved. This is useful for consistency, and relevant in gradient plasticity where the local *(explicit formulation)* or nonlocal *(implicit formulation)* effective plastic strain needs to be discretised in addition to the displacements. Using different orders of interpolation, both formulations are explored in the second-order and a fourth-order implicit gradient formulation is proposed. Results, corroborated by dispersion analysis, show that all considered models give good regularisation with mesh-independent results. Compared with finite element approaches that use Hermitian shape functions for the plastic multiplier or mixed finite element approaches, isogeometric analysis has the distinct advantage that no interpolation of derivatives is required.

In localisation problems, numerical accuracy requires the finite element size employed in simulations to be smaller than the internal length scale. Fine meshes are also needed close to regions of geometrical singularities or high gradients. Maintaining a fine mesh globally can incur high computational cost especially when considering large structures. To achieve this efficiently, selective *refinement* of the mesh is therefore required. In this context, splines need to be adapted to make them analysis-suitable. Thus, an *adaptive* isogeometric analysis framework is also developed for gradient elasticity and gradient plasticity. The proposed scheme does not require the mesh size to be smaller than the length scale, even during analysis, until a localisation band develops upon which adaptive refinement is performed. Refinement is based on a multi-level mesh with truncated hierarchical basis functions interacting through an inter-level subdivision operator. Through Beziér extraction, truncation of the bases is simplified by way of matrix multiplication, and an element-wise standard finite element data structure is maintained.

In sum, a *robust computational framework* for engineering analysis is established, combining the flexibility, exact geometry representation, and expedited design-through-analysis of *isogeometric analysis*, size-effect capabilities and mesh-objective results of *gradient-enhanced continua*, the standard convenient data structure of *finite element analysis* and the improved efficiency of *adaptive hierarchical refinement*.

ACKNOWLEDGMENTS

In the name of God, the Most Gracious, the Most Merciful

"*For, should you try to count God's blessings, you could never compute them! Behold, God is indeed much-forgiving, a dispenser of grace.*" Qur'an 16:18

And truly...

"Nothing is easy except what You have made easy

If You wish, You can make the difficult to be easy."

All praise is due to the Creator of the heavens and the earth Who gave me the health and ability to complete this fulfilling and rewarding journey – "Our Lord, all praise is due only to You, praise which is abundant, excellent and blessed." May the peace and blessings of God be on the final messenger, prophet Muhammad, peace be upon him.

A number of very nice people have helped in making this undertaking fruitful. Chiefly, I am deeply indebted to my good-natured and outstanding supervisor, Professor René de Borst, for accepting my application, offering unconditional and comprehensive support, diligent coaching and meticulousness, creating a great learning environment and support system, open, swift and comforting email policy, and many more. His patience and generosity are rare to come across. It has been an invaluable experience.

My second supervisor, Professor Harm Askes' strategic support and benevolent disposition is immensely appreciated - an inherent teacher with total willingness to address any needs. This has always been very comforting and reassuring. The yellow book I received on my first day proved to be very helpful.

Courses delivered by, and interactions with Dr. Erik Jan Lingen of Dynaflow Research Group have been very educative and I believe my programming skills have improved. His very approachable and simple style has made it fun at times.

An esteemed associate, treasured mentor and intermittent constructive critic, Dr. Lin Chen has always offered very useful help and advice, from IGA to professional practices. It has been a pleasure working together and being in very close proximity. I

will better take note of what constitutes, or not, professional practice in the future, God-willing.

The ever-ready support and unconditional kindness of Dr. Fathima Mehmanzai has been a significant pillar of support throughout my journey. I would also like to extend my appreciation to other members of the PoroFrac research team for their company and support despite being on a different research trajectory: Dr. Tartarini, Sepideh, Farshid, Tim and Dr. Motlagh.

My short research trip to Eindhoven was a very pleasant experience. I am sincerely grateful to Dr. Clemens Verhoosel, Professor Harald van Brummelen, Linda Essink and the members of their research group for their kindness, support and for creating an enabling environment.

Comments and suggestions from Dr. Inna Gitman, Dr. Stefanos Papanicolopulos and Professor Luca Susmel, as well as reviewers initiated healthy academic meditation for which I am very appreciative. I would also like to express my profound gratitude to Dr. Taofeeq-ibn-Mohammed and Dr. Khameel Mustapha for their time and comments close to the end of this work.

The Department of Civil and Structural Engineering, under the auspices of Professor Harm Askes, provided financial support for my studies. I am extremely thankful.

Ever since I was born, or more accurately, even before I came into the world, two extraordinary people have spearheaded my nurturing and development, financially, socially, spiritually, intellectually, emotionally and physically. First my unique and splendid mum, Hajiya Sa'adatu Kolo, and my fabulous dad, Alhaji Mohammed Kolo, are a couple I am proud to be nurtured by. Their perpetual selfless sacrifice and deep-rooted doggedness to ensure and see that I, as well as my siblings, succeed, is a bounty from God, all thanks and praises are due to Him. I can't thank them enough, I pray that He has mercy on them the way they nurtured me right from my toddler years, amen. My amazing, marvellous and God-given siblings – Amina, Mohammed, Fatima and Aliyu – are a priceless treasure I would not exchange for a mountain of gold. I thank God for them, may God bless them all, amen. This team is my blood and have always stood by me in all imaginable ways.

May God have mercy on my grand-mum, Hajiya, who as a sign of support, gave me an

adorable warm jacket to protect me from the cold overseas, when first leaving to study abroad. The journey reached a milestone in her absence. May God forgive and bless her, and illuminate her grave, amen.

All praise is due to God for the Message Islamic Information Centre, the Nigerian Muslim Forum UK (Sheffield Chapter) and their respective beautiful people. From friends to teachers to icons of good, may God bless them all, amen. This has helped prevent the spiritual battery from getting very low. I would like to express special appreciation to my housemate, Baraa, for the company and inestimable kindness especially when I fell ill. May God bless him, amen.

Stalwart friends, accommodating to-be and many more have always given the needed support. May God reward you well, amen.

To the listed and unlisted, who have contributed to the success of this work, directly or indirectly, *jazakumullahu khayran*, may God reward you with goodness, and give you guidance to the best of the best, amen.

Isa Kolo
Sheffield, UK
March 2019

STATEMENT OF ORIGINALITY

Unless otherwise stated in the text, the work described in this thesis was carried out by the candidate. None of this work has already been accepted for any degree, nor is it concurrently submitted in candidature for any degree.

Candidate: _____

Isa Kolo

CONTENTS

LIST OF FIGURES

LIST OF TABLES

Chapter 1

INTRODUCTION

1.1 Background and motivation

With the ever-growing capacity of computers, numerical simulation is increasingly becoming an integral part of engineering. From automotive crash tests or collapse of civil structures to design of prototypes, a virtual computer environment presents a readily available and often cheap alternative for engineering analysis [32]. In computational mechanics, materials can be assumed to be composed of a continuous body, and equations derived from the conservation laws are used to describe material behaviour. This is the basic premise of *classical continuum mechanics*, and as long as the level of observation remains sufficiently large, the assumptions and relations still hold.

Experiments have shown that, for many engineering materials (metals, composites, rocks, concrete, ceramics, alloys, polymers), geometrically similar specimens of the same material, but of different sizes, exhibit different mechanical behaviour. This phenomenon is called the *size effect* (figure 1.1). The source of this behaviour has been traced to the underlying micro-structure of the material. Classical continuum mechanics theories are insufficient for accurately capturing the size effect since they are based on the assumption that the material is significantly larger than its micro-structure.

The effects of micro-structure also become significant in *localisation* of deformation. This occurs when, despite the monotonic external loading being applied, there emerges a narrow region in a structure where all further deformation concentrates [39], cf. figure 1.2. When employing the finite element method with classical continuum theories, the width of the localisation zone tends to depend on the finite element mesh. The localisation zone width progressively decreases as the mesh size decreases until a line of zero thickness is almost reached. The observed mesh-sensitivity is physically un-

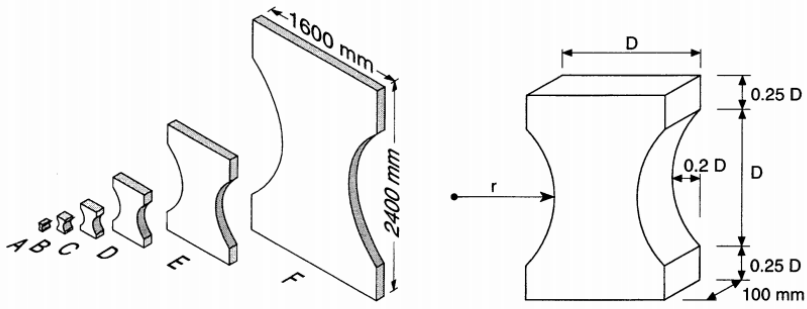

Specimens with sizes in a scale range of 1:32 and specimen proportions.

type	A	B	C	D	E	F
D [mm]	50	100	200	400	800	1600
r [mm]	36.25	72.5	145	290	580	1160

(a) Specimen dimensions

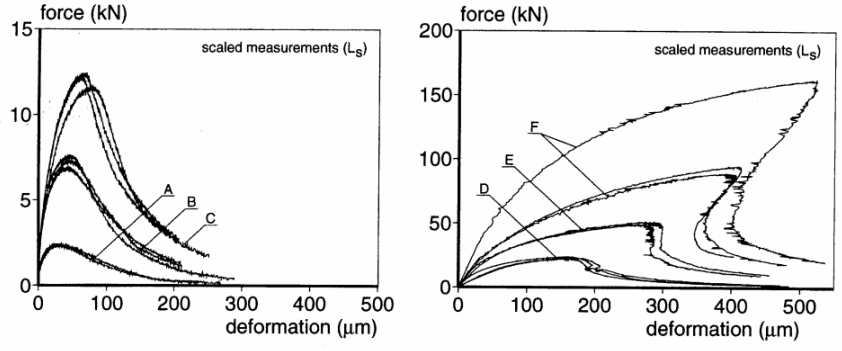

(b) Load-displacement curves showing softening behaviour

Figure 1.1: Size effect in rock (sandstone) under tension [138].

acceptable because it indicates a successive decrease in energy released until there is no released energy, i.e. when the localisation zone becomes a line with zero thickness. The mathematical basis behind this is that the boundary value problem describing the classical continuum becomes ill-posed. In static problems, the elliptic equations of the boundary value problem become hyperbolic; in dynamics or wave propagation problems, the hyperbolic equations of the initial boundary value problem become elliptic [39].

Ill-posed problems can also be encountered, generally, when classical continuum

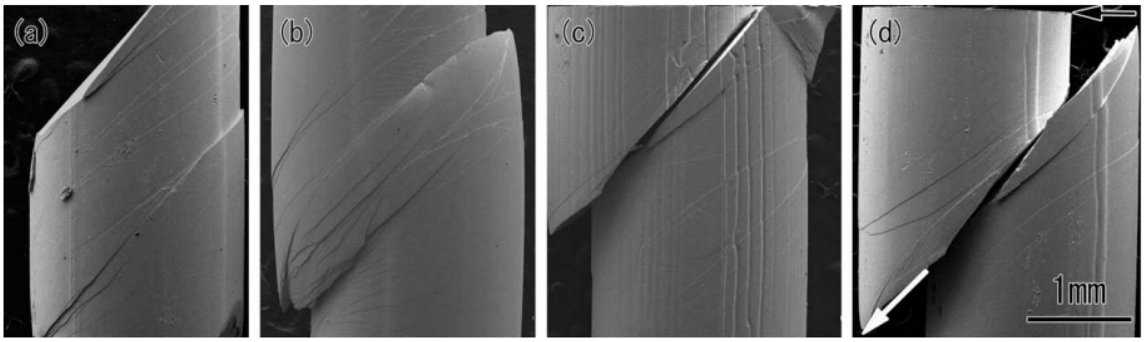

Figure 1.2: Localisation in an alloy (metallic glass) under compression [148].

models are employed for materials with a *softening* behaviour, i.e. after reaching the elastic limit and ultimate load, the load-carrying capacity of the material progressively decreases until failure, see figure 1.1(b) left. This applies, for example, in the case of continuum damage mechanics and softening plasticity [37, 72, 73].

Introducing a *length scale* - a parameter with the unit of length - into the field equations or material description, implicitly or explicitly, directly or indirectly linked to the micro-structure, solves the aforementioned problems [113]. This in turn provides a more accurate and more robust prediction of material behaviour and failure - an important aspect of engineering design.

1.2 The physics of length scales and strain gradients

The length scale embodies information about the microstructure of a material. There is no consensus on its physical interpretation; it tends to be material/context dependent. In gradient elasticity, the length scale has been related to the average cell size for materials with a dominant microstructure such as bones and foams, based on bending and torsion experiments. At the atomic scale size, it has been related to lattice spacing for dislocation cores. In adopting gradient-enhanced beam theories for flexural wave propagation in carbon nanotubes, the length scale was directly related to inter-atomic spacing of the associated discrete lattice model [11]. This latter case is illustrated in figure 1.3 in which the length scale is directly related to d, the inter-atomic spacing.

A model consisting of particle and strings is in harmony with elasticity, where the material returns to its initial state after unloading.

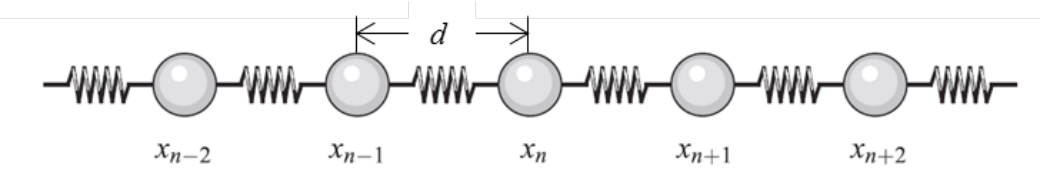

Figure 1.3: One-dimensional discrete model consisting of particles $x_{(\bullet)}$ and strings [11].

In gradient plasticity, the length scale has been directly related to grain size or grain boundary thickness for polycrystalline specimens or the dislocation spacing/source distance in single crystals [4, 11]. *Dislocation* is an irregularity in a material crystal at atomic level. In ductile materials like metals, dislocations are the carriers of plastic deformation. Moreover, gradient effects can be physically explained by the existence of two kinds of stored dislocations: *statistically stored dislocations* (SSDs) and *geometrically necessary dislocations* (GNDs). SSDs are stored dislocations as a result of dislocations trapping one another in a random way. GNDs are the stored dislocations that relieve the incompatibilities of plastic deformation within a polycrystal caused by non-uniform dislocation slip. The cumulative effect of SSDs cancels out in a homogeneous strain field, cf. figure 1.4, while GNDs are needed to make the plastic strain field non-uniform, thereby producing a gradient of the plastic strain [4]. Material deformation enhances dislocation formation, dislocation motion and dislocation storage. Hardening in turn results from the stored dislocations (SSDs and GNDs). SSDs have been determined to be dependent on the effective plastic strain while GNDs are dependent on the gradient of the effective plastic strain [4, 8]. This explains why several strain gradient plasticity theories are based on GNDs to characterise size effect [4]. Furthermore, according to [141], L_s or the mean distance between SSDs characterises the length scale in gradient plasticity and is the major factor influencing the evolution of the length scale.

The usual mechanical tests at the macro level (large scale) are not sufficient to determine/calibrate the length scale. Experiments at scales where the non-homogeneity

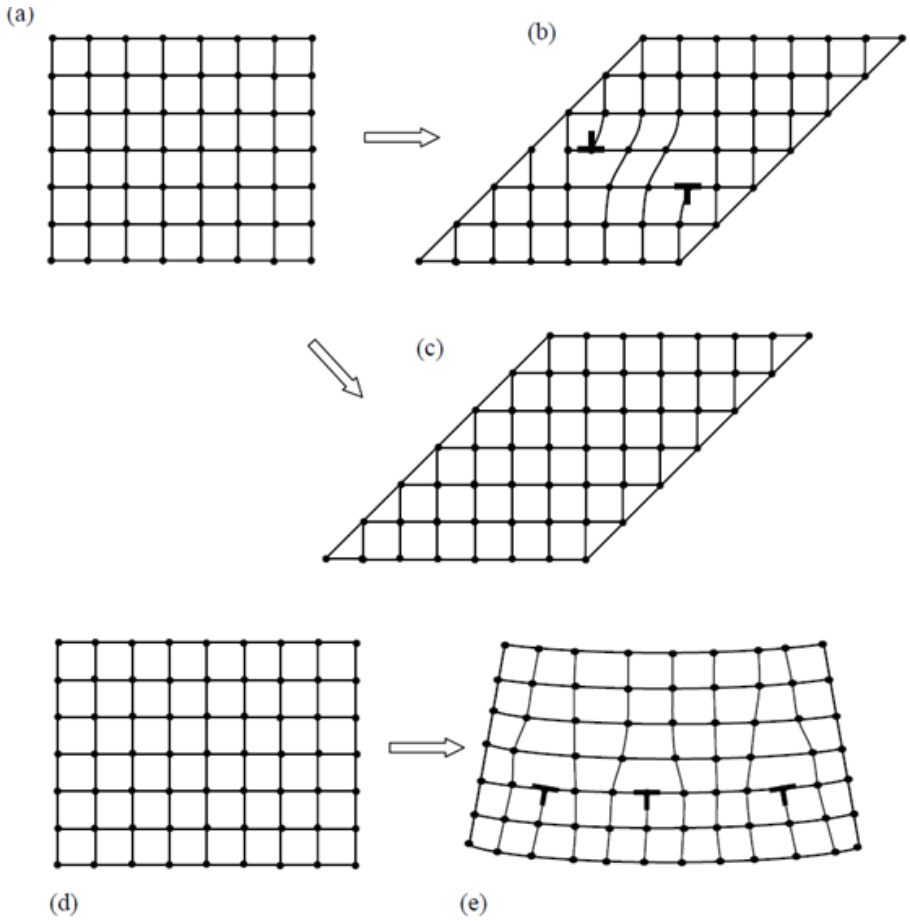

Figure 1.4: Dislocations and strain gradient effects in plasticity based on square lattices with atoms. (a) and (d) are the initial lattices before undergoing plastic deformation. When (a) deforms homogeneously, there can be SSDs (b) or no dislocations (c); the strain is homogeneous in both cases, thus the cumulative contribution of the SSDs in (b) to the overall deformation cancels out. When (d) deforms non-homogeneously, GNDs form and they are characterised by the presence of lattice curves (strain gradients) [4].

of the material becomes pronounced are needed – this is when the strain gradient effect becomes dominant, cf. figure 1.4(e). Thus, typically, experiments such as micro/nano-indentation tests, micro-bending tests and micro-torsion tests along with digital image correlation techniques are required to determine the length scale. These tests have been used to determine the length scale in gradient elasticity [64], gradient plasticity [5, 51, 135], and gradient damage [54] models. Numerically, Molecular Dynamics tests [87] and homogenisation techniques [111] have also been used to determine gradient

elasticity constants.

While the motivation for a length scale in gradient elasticity is different from gradient plasticity, it remains a material property linked to the material microstructure. It is a representation of the dominant source of heterogeneity at the scale of observation. This assumption is maintained throughout this thesis but no attempt has been made to work with exact or experimentally derived values of the length scale. This is beyond the scope of the current work.

1.3 Regularisation techniques

There are various ways of introducing a length scale, also called *regularisation* or *localisation limiting*. The main approaches can be grouped into the following [118, 128], see figure 1.5:

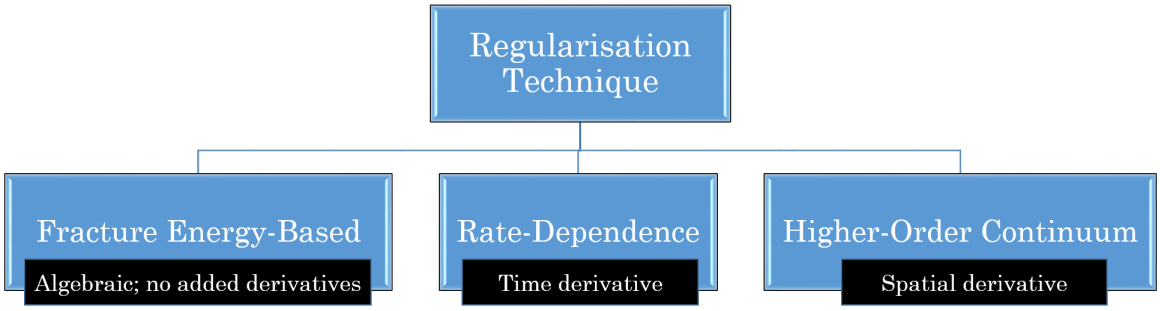

Figure 1.5: Regularisation techniques

- Fracture energy-based approaches: Through the element size, the softening behaviour of the stress-strain curve is adjusted in order to ensure proper dissipation of internal energy at failure. Smeared crack models constitute an example of models based on fracture energy [20].

- Rate-dependent models: This involves the inclusion of rate-dependence in the constitutive equations either through viscosity or material rate dependence [142].

- Higher-order continuum models: This involves the use of higher-order equations and boundary conditions obtained by (a) taking into account the strains of a surrounding point to compute its stress either by integral formulations (non-local) [19] or higher-order gradients (gradient-enhanced) [35]; or (b) adding micro-rotational degrees of freedom to the continuum description [33].

See [39] and Chapter 2 of [106] for a concise description of all approaches. Other methods such as the use of thermal conduction to regularise softening [23, 90] can also be found in the literature.

While approaches based on fracture energy are able to capture size effect and solve mesh-dependency of results, the fracture energy release rate takes place in a different area for each mesh [106]. This is because the boundary value problem still remains ill-posed. Addition of rate dependence makes the problem to be well-posed. However, this is limited to transient loading conditions and the effect of regularisation is rapidly lost as the rate-independent limit is approached. The addition of micro-rotational degrees of freedom, also called *micro-polar* or *Cosserat* continuum, is only applicable to problems where shear deformation dominates. It fails in the case of pure tension [35, 106].

Non-local and *gradient-enhanced* continuum models make the problem well-posed, are motivated from the micro-structure (physically sound), and can handle problems with tensile or shear loading. In non-local models which involve integrals, the time-consuming task of determining the neighbourhood for each integration point is required. Furthermore, the implementation of the consistent tangent operator into finite element codes is cumbersome because it involves spatial interaction between material points that can be at arbitrary distance from each other. In other words, the mechanical nonlocality results in mathematical nonlocality. In gradient-enhanced models, the non-local integral averaging is replaced by computing spatial derivatives. This preserves the mechanical nonlocality and removes the mathematical nonlocality making gradient-enhanced models more efficient and more suitable for implementation [9].

1.4 The adopted approach and the problem

1.4.1 Discretisation with splines

This thesis focuses on adopting gradient-enhanced higher-order continuum models and their solution using the finite element method. While this has a sound theoretical basis [3], it can be mathematically intensive. Adding higher-order gradients to the constitutive equations places more requirements on the continuity of the shape functions used for discretisation. This raises issues and inconveniences when using the traditional finite element method which typically employs C^0-continuous Lagrange shape functions [11, 36].

Methods such as Hermitian finite elements and mixed finite element methods have been developed to meet higher-order continuity requirement. However, these methods are not robust as they are susceptible to unreliable solutions and too many constraints [36, 39]. In the context of gradient plasticity, for Hermitian and mixed finite elements to be robust, the balance of interpolations, suitable integration quadrature and additional boundary conditions are required [36]. If these are not met, the solution can be unreliable. Moreover, patch tests are required for these elements and only few of these elements pass the test and fulfil the required conditions. Meshless methods are another option. However, implementational convenience is an issue, for example, with respect to essential boundary conditions [9, 58]. This makes it worth-while to explore other methods.

With the advent of isogeometric analysis [63], which naturally exploits higher-order spline-based shape functions, came many possibilities in the realm of basis functions with higher-order continuity. In addition to capturing the exact geometry for analysis (which eliminates geometric discretisation errors), one easily attains C^{p-1} continuity by employing a Non-Uniform Rational B-Spline (NURBS) of order p. Isogeometric analysis was developed as an extension of the finite element method where basis functions used for geometrical modelling are also used for analysis. It presents a platform to fast-track the design-through-analysis process by bypassing the cumbersome meshing process, see figure 1.6.

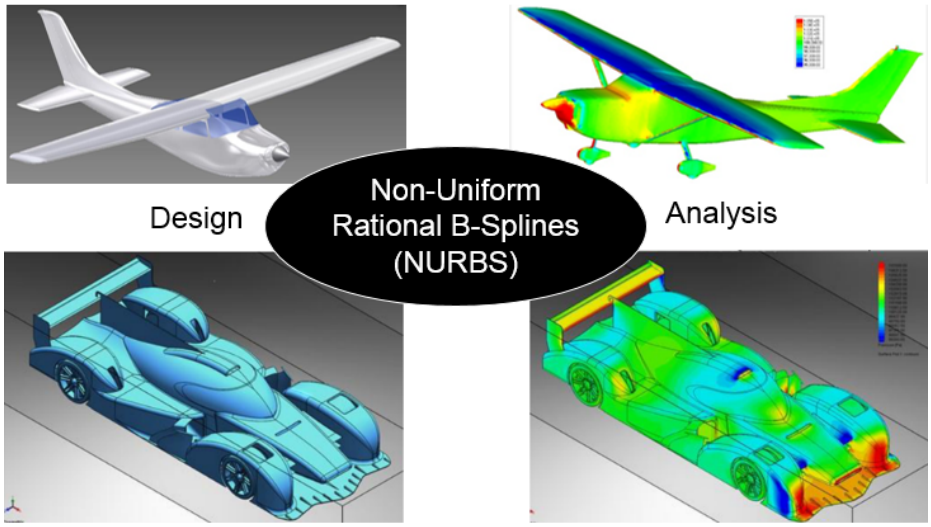

Figure 1.6: In isogeometric analysis, the spline-based shape functions used for design are employed for analysis as well

1.4.2 Adaptive mesh refinement

Sometimes in numerical analysis, accuracy necessitates a fine mesh close to certain geometrical features, e.g. the point of singularity of the L-shaped beam in figure 1.7. However, maintaining a fine mesh globally can be overly expensive. The tensor product structure of NURBS, which restricts local refinement, makes it necessary to adapt splines to make them analysis-suitable. This has attracted several research efforts [60]. Computations using higher-order gradient models also stand to benefit from local refinement, for example, in resolving areas around localisation bands [39, 76]. Mesh refinement strategies generally ensure efficient computations especially in problems with geometrical singularities, localisation and/or strong gradients.

1.4.3 Problem statement

Gradient elasticity captures size effect and removes the singularity observed at crack tips using the classical theory [11]. Gradient plasticity eliminates the spurious mesh sensitivity observed in softening and localisation problems by defining the width of the localisation zone thereby maintaining a well-posed boundary value problem [35]. Isogeometric analysis naturally provides the higher-order continuity required in solv-

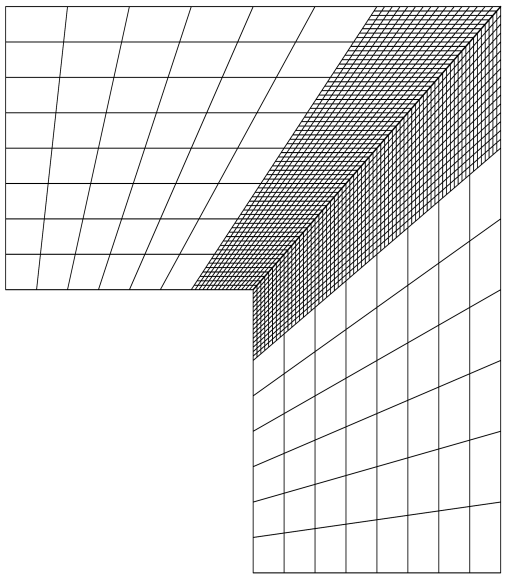

Figure 1.7: In numerical simulation, refinement is needed close to the inner corner of an L-shaped beam for accuracy.

ing gradient elasticity and gradient plasticity formulations but this has not been well explored. In addition, there is no efficient isogeometric analysis framework backed by extensive studies for these models.

1.5 Aims and scope

The aim of this work is to establish an efficient computational framework for engineering analysis by exploiting spline-based shape functions. The objectives of this work include:

- development, implementation and assessment of an isogeometric analysis framework for gradient-enhanced elasticity and gradient-enhanced plasticity models. This facilitates consistent higher-order discretisation of variables, ensures the preservation of exact geometry and expedites the design-through-analysis process.

- development of a suitable adaptive scheme to enable efficient computations.

In principle, almost all materials can be considered within a gradient-enhanced

elastoplastic framework. One would just need to accordingly tailor (i) the yield criterion, (ii) the plasticity flow rule (for determining the magnitude and direction of the plastic strain rate), and (iii) the hardening/softening law for evolution of the yield stress. This thesis adopts a Von Mises yield criterion (which works for metals) and an associated flow rule, i.e. the yield function coincides with the plastic potential used to define the direction of flow. See [105] for example, for a non-associative Drucker-Prager gradient-dependent yield function relevant for geo-materials.

An assumption of small deformations is made throughout this work. Only static monotonic loading is considered. A deterministic description of isotropic and homogeneous continuum media is adopted.

1.6 Implementation and code

All formulations in this thesis have been implemented using Jem/Jive C++ libraries [42]. This is an open source, research-oriented C++ programming toolkit for solving partial differential equations. It has support for several shape functions, supports sparse matrix operations and incorporates many solvers. The models in this work have been implemented in this environment taking advantage of several relevant functions, models and modules. While codes based on C++ have been written to solve the problems, MATLAB has been largely used for post-processing of results.

1.7 Thesis outline

A progressive approach has been adopted in this work. The work starts, in Chapter 2, with two formulations of gradient elasticity - one requiring $\mathcal{C}^1$-continuous shape functions (monolithic approach) and the other, an operator-split (staggered) approach where standard $\mathcal{C}^0$-continuous shape functions are sufficient. The aim is to see how the staggered approach compares to the original fourth-order partial differential equation using the monolithic approach. The two formulations are discretised using isogeometric analysis with NURBS and from the comparison of results, it is shown that the higher-order formulation is more versatile as the operator-split approach, strictly-speaking, works only for infinite bodies where boundary conditions do not need to be

imposed. T-spline discretisation that provides better and more flexible geometry description is also presented.

For localisation problems using classical plasticity, mesh-dependency is observed. Chapter 3 addresses localisation problems with splines by adopting the explicit gradient plasticity formulation. Here, the yield function depends on the Laplacian of the plastic strain in addition to its usual dependence on the plastic strain. This explicit addition of the Laplacian of the strain gives a rigorous regularisation of the boundary value problem. One-dimensional and two-dimensional problems are presented.

The formulation of implicit gradient plasticity is detailed in Chapter 4. A second-order formulation using Green's nonlocal weighting function as well as a fourth-order formulation using Gaussian nonlocal weighting function are presented. While the implicit formulation gives better computational stability, the standard yield function needs to be modified for full regularisation. The two formulations are shown to give full regularisation and are compared with the explicit gradient formulation through dispersion analysis.

With a computationally stable spline-based gradient plasticity formulation in place, adaptive hierarchical refinement of NURBS is incorporated in Chapter 5. Refinement is based on the concept of elements and their child elements, which are activated or deactivated accordingly, in a hierarchical mesh. For gradient elasticity, elements are marked for refinement using error in energy norm while a heuristic marking strategy based on the effective plastic strain is presented for gradient plasticity. Transfer of both old and current history variables between meshes is outlined and also tested, first using classical plasticity. Next, an example for gradient plasticity is presented which shows a nice match with standard gradient plasticity results.

Chapter 6 highlights the conclusions of the work and gives suggestions for future research directions.

1.8 Thesis highlights

The main highlights of this work are summarised as follows:

- A comparison has been presented using isogeometric analysis for the fourth-order gradient-elastic formulation between the monolithic solution and the staggered

solution approach where boundary condition effects have been substantiated indicating the limitations of the staggered approach. For the monolithic solution, theoretical convergence rates were achieved for polynomials of order three and above. For polynomial order of two, suboptimal convergence rate was observed, confirming earlier studies for the Cahn-Hilliard equation.

- An isogeometric analysis approach to explicit and implicit gradient plasticity has been developed using equal as well as unequal orders of interpolation within the Beziér extraction framework which maintains standard finite element data structure. A fourth-order implicit gradient formulation was also formulated using the Gaussian weighting function.

- Dispersion analysis has been performed for second-order explicit and implicit gradient plasticity formulations as well as the proposed fourth-order formulation which has more regularisation potential. The upward curving of the shear band near the free boundary for the implicit gradient formulations has been highlighted and is related to the emergence of stationary Rayleigh waves.

- It has been observed that the explicit gradient plasticity formulation does not guarantee convergence. Convergence was achieved only for low hardening modulus to elastic modulus ratio. On the other hand, the implicit formulation is computationally more stable. However, it is necessary to modify the yield function of the implicit formulation to achieve full regularisation.

- A hierarchical refinement framework based on isogeometric analysis has been developed for gradient-elasticity and gradient-plasticity to enable efficient computations. For hierarchical refinement in gradient plasticity, a heuristic element marking strategy was proposed based on the measure of non-local plastic strain and the length scale. Hence, computations do not necessarily need to start with a fine mesh that can accommodate the localisation band, refinement is triggered when required.

Chapter 2

CONVERGENCE ANALYSIS OF LAPLACIAN-BASED GRADIENT ELASTICITY IN AN ISOGEOMETRIC FRAMEWORK[1]

2.1 Introduction

Classical continuum mechanics assumes that the solid or the structure under consideration is of a dimension that is significantly larger than its underlying microstructure, so that microstructural effects can be ignored. When the effects of microstructure become dominant – as is the case with localised shear bands in softening geomaterials [97] – classical continuum mechanics is no longer sufficient. Experiments have shown that specimens of a material with the same geometry, but different dimensions, exhibit different mechanical behaviour. This is called the size effect and has been recorded for quasi-brittle materials (concrete, rock, ceramics) [21], metals [81], composites [102] and micron-scale structures [80]. Indeed, the size effect, which has been attributed to the existence of a material microstructure, is not captured by classical continuum theories. Thus, enriching the classical continuum model with an internal length scale which is related to its material microstructure, enhances its applicability. This is the motivation behind the work of Mindlin [94] and Eringen and Suhubi [49], although earlier work along the same lines has been done by the Cosserat brothers [31]. A review and historical perspective is given in [11].

In Mindlin's theory [94], twelve independent degrees of freedom at two scales of deformation were identified: three displacement components and nine microdeformation components. Three possible assumptions that can relate the microscopic deformation

[1]Based on: I. Kolo, H. Askes, and R. de Borst. Convergence analysis of Laplacian-based gradient elasticity in an isogeometric framework. *Finite Elements in Analysis and Design*, 135:56–67, 2017

gradient and the macroscopic displacement were outlined. The strain energy density can be expressed as a function of strains and second derivatives of macroscopic displacements thereby obscuring the multiscale nature of the theory [93, 94, 137]. This special case defines gradient elasticity. In statics, there are two additional parameters with the dimension of length which could be related to the underlying material microstructure [26, 136]. These two parameters result from grouping the five elastic constants in the isotropic Mindlin theory. A simplification is achieved when these two length scales are equal – an approach credited to Aifantis [2, 6]. A proper theoretical framework was provided in [53] and [101] using the principle of minimum potential energy and principle of virtual work respectively.

The Aifantis theory modifies the classical stress-strain relation by making the stress also dependent on the Laplacian of the strain, thus resulting in a fourth-order governing partial differential equation. To solve the equation, standard C^0-continuous elements cannot be used. This is because higher order terms appear in the weak form, thus requiring the derivatives of displacements to be continuous – C^1-continuity requirement. In principle, the problem can be solved by Hermitian finite elements [108, 147], mixed methods [7, 88, 107, 127, 146], meshless methods [10] and subdivision surfaces [30]. However, all these methods have their drawbacks in terms of efficiency or implementational convenience. For Hermitian and mixed finite elements to be robust, the balance of interpolations, suitable integration quadrature and additional boundary conditions may be required [36]. If these are not met, the solution can be unreliable. Moreover, patch tests are required for these elements and sometimes, only few of these elements pass the test and fulfil the required conditions. Meshless methods are another option. However, implementational convenience is an issue, for example, with respect to essential boundary conditions [9, 58]. Thus, it remains worthwhile to explore new methods for the implementation of gradient elasticity.

An alternative approach is to use an operator split that creates two second-order partial differential equations. In this staggered approach [121], the solution from the first equation (classical elasticity) serves as input for the second equation which solves for the gradient-enriched variables. Since this is a set of two second order partial differential equations, it can be solved with C^0-continuous elements. It is noted that the

approach suggested in Reference [121] is, strictly speaking, only applicable to an infinite body where no enforcement of boundary conditions is required [82]. Although it removes strain singularities, Skalka et al. [131] found it incapable of predicting the desired stress field around a crack in composite foams (cusp-like closure at crack tip), again pointing out issues with boundary conditions i.e. difference in boundary conditions compared with the fourth-order partial differential equation. These differences have also been pointed out in [11, 13].

These restrictions have motivated Skalka et al. [131] to propose a similar strategy for Eringen's model [46], i.e. a decoupling or one-way coupling for the two second order partial differential equations. An iterative procedure was proposed for Eringen's model (also formulated by Askes and Gutiérrez [12] as implicit gradient elasticity) with the length scale replaced by a parameter increment which is chosen to be arbitrarily small. However, the choice of the number of iterations and the convergence criterion are tied to crack properties; for an arbitrary geometry, the choices seem unclear and may likely incur high computational cost. Eringen's theory is an approximation of an earlier nonlocal integral formulation[1, 47, 48]. However, it has been shown that for certain loading conditions, fully nonlocal stress-strain laws used in modelling Euler-Bernoulli elastic beams give solutions that coincide with the standard local solution, and hence do not capture size effects [109]. This can only be avoided either by combining local and nonlocal curvatures in the constitutive equation or using a gradient elastic model [22, 27].

The staggered approach has been widely adopted because it can be implemented easily in existing finite element packages since standard C^0-continuous finite elements can be used. Herein, we compare the two approaches to see how the staggered approach compares to the original fourth-order partial differential equation using the monolithic approach. When comparing the two solution strategies, a method which fulfils the C^1-continuity requirement is needed. Isogeometric Analysis [63] is an extension of finite element analysis where the spline-based shape functions used to approximate the geometry are used for the analysis as well. Although coined and standardised in [63], other works along the same lines exist [61, 149]. The original drive behind isogeometric analysis was to integrate the design and analysis processes, which has

the additional benefit of capturing the exact geometry, unlike standard finite element analysis. Moreover, it comes with the advantage of ease in achieving higher degree of continuity. This is due to the Non-Uniform Rational B-Splines (NURBS) shape functions. Isogeometric analysis has been used where higher continuity is required such as in solving the Cahn-Hilliard equation [56, 69, 84], gradient damage models [139] and also in the context of gradient elasticity [50, 86, 101, 123]. Herein, we employ a Bézier extraction framework for both NURBS and T-splines and consider the gradient elasticity formulation with and without operator-split. In [69], the direct fourth order Cahn-Hilliard equation and a mixed formulation with coupled equations have been studied using isogeometric analysis. The study concluded that direct discretisations of higher order partial differential equations are more efficient than mixed formulations. This is because the direct discretisation requires less degrees of freedom to obtain a given level of accuracy; however, approximations of sufficient order are required to obtain optimal convergence rates.

This chapter compares convergence rates for the Aifantis gradient elasticity theory with and without operator split. The chapter is organised as follows: section 2.2 presents the Aifantis gradient elasticity formulation including the operator-split. Section 2.3 starts with a brief description of NURBS and Bézier extraction in isogeometric analysis [24] before discretisation of the gradient elasticity formulation with and without operator split. In section 2.4, the two discretisation approaches are compared in terms of error norms and convergence rates. T-splines are introduced in section 2.5 and finally, some more examples using gradient elasticity are presented.

2.2 Laplacian-based gradient elasticity formulations

2.2.1 Aifantis' gradient elasticity formulation

The gradient elasticity theory of Aifantis [2, 6] is considered herein. The theory extends the classical linear elastic constitutive relations by introducing the Laplacian of the strain as follows:

$$\sigma_{ij} = D_{ijkl}(\varepsilon_{kl} - \ell^2 \varepsilon_{kl,mm}) \tag{2.1}$$

where σ_{ij} is the stress tensor, ε_{kl} is the strain tensor, and ℓ is a length scale parameter. D_{ijkl} is the constitutive tensor, and for an isotropic linear elastic material, it is given by:

$$D_{ijkl} = \lambda\delta_{ij}\delta_{kl} + \mu\delta_{ik}\delta_{jl} + \mu\delta_{il}\delta_{jk} \tag{2.2}$$

λ and μ are Lamé constants, and δ_{ij} is the Kronecker delta. The accompanying equilibrium equations are:

$$\sigma_{ij,j} + b_i = 0 \tag{2.3}$$

where a comma denotes partial differentiation and b_i are the body forces. Substituting the stress-strain relation, eq.(2.1), and assuming small displacement gradients, one obtains the following fourth-order partial differential equation:

$$D_{ijkl}(u_{k,jl} - \ell^2 u_{k,jlmm}) + b_i = 0 \tag{2.4}$$

where u_k are the displacement components.

2.2.2 Ru-Aifantis theorem: Operator-split

In the staggered approach of the Ru-Aifantis theorem, the fourth-order equation in eq.(2.4) is split into two second order partial differential equations [11, 16]:

$$D_{ijkl}u^c_{k,jl} + b_i = 0 \tag{2.5}$$

$$u_k - \ell^2 u_{k,mm} = u^c_k \tag{2.6}$$

where u^c_k is the displacement field that obeys the classical elasticity equation eq.(2.5), hence the superscript $(\bullet)^c$. Eq.(2.5) is first solved for u^c_k and the result is used in eq.(2.6) to solve for u_k. Thus, there is one-way coupling between them.

2.3 Isogeometric finite element discretisation

In traditional finite element analysis, Lagrange polynomials serve as the basis or shape functions. Isogeometric analysis replaces these Lagrange polynomials with splines

which are also used in generating the geometry. This implies that both geometry and finite element analysis are based on spline functions and hence the name isogeometric analysis. NURBS or Non-Uniform Rational B-splines is the most widely used spline technology and this influenced its choice as a starting point in the seminal work where isogeometric analysis was proposed [63].

2.3.1 NURBS shape functions

A NURBS curve, $\mathbf{T}(\xi)$, is defined by a set of control points $\mathbf{P} = \{P_a\}_{a=1}^{n} \in \mathbb{R}^d$, a knot vector with increasing parametric coordinate values $\mathbf{\Xi} = \{\xi_1, \xi_2, \ldots, \xi_{n+p+1}\}$, and a set of rational basis functions $\mathbf{R} = \{R_{a,p}^n\}_{a=1}^{n}$ with p being the polynomial degree, and n the number of basis functions:

$$\mathbf{T}(\xi) = \sum_{a=1}^{n} P_a R_{a,p}(\xi) \tag{2.7}$$

The individual coordinates of the knot vector are called knots which are analogous to nodes in standard finite elements and the interval between knots is a knot span. Unlike nodes, knots are usually not interpolatory. If the first and last knots are repeated $p+1$ times, the knots become interpolatory, and the knot vector is said to be open. The basis functions of a NURBS curve are expressed as:

$$R_{a,p}(\xi) = \frac{w_a B_{a,p}(\xi)}{\mathbf{W}(\xi)} \tag{2.8}$$

where $B_{a,p}$ is the B-spline basis function, w_a is the corresponding weight and $\mathbf{W}$ is the weight function given by:

$$\mathbf{W}(\xi) = \sum_{b=1}^{n} w_b B_{b,p}(\xi) \tag{2.9}$$

The B-spline basis is defined for $p = 0$, as:

$$B_{a,0}(\xi) = \begin{cases} 1, & \xi_a \leq \xi \leq \xi_{a+1} \\ 0, & \text{otherwise} \end{cases} \tag{2.10}$$

and by the Cox-de Boor recursion formula for $p > 0$:

$$B_{a,p}(\xi) = \frac{\xi - \xi_a}{\xi_{a+p} - \xi_a} B_{a,p-1}(\xi) + \frac{\xi_{a+p+1} - \xi}{\xi_{a+p+1} - \xi_{a+1}} B_{a+1,p-1}(\xi) \tag{2.11}$$

A NURBS geometry in $\mathbb{R}^d$ is obtained from projective transformations of B-splines in $\mathbb{R}^{d+1}$ through the weights. A NURBS curve (univariate) can be extended to a surface (bivariate) through a tensor product of the bases [63]:

$$N_{a,b}^{p,q}(\xi,\eta) = \frac{B_{a,p}(\xi) A_{b,q}(\eta) w_{a,b}}{\sum_{c=1}^{nB} \sum_{d=1}^{nA} B_{c,p}(\xi) A_{d,q}(\eta) w_{c,d}} \tag{2.12}$$

where $N_{a,b}^{p,q}$ is the two-dimensional NURBS basis function; η, $A_{b,q}$, and q are the knot vector, B-spline basis and the polynomial degree in the second spatial dimension respectively. The number of basis functions in the ξ and η directions are nB and nA respectively. Thus a NURBS surface, $\mathbf{S}$, is defined by replacing $R_{a,p}$ in eq.(2.7) by $N_{a,b}^{p,q}$:

$$\mathbf{S}(\xi,\eta) = \sum_{a=1}^{nA} \sum_{b=1}^{nB} P_{a,b} N_{a,b}^{p,q}(\xi,\eta) \tag{2.13}$$

A subdomain with uniform elements and material models is termed a patch. A knot vector divides a patch into elements, and hence, insertion of knots is analogous to h-refinement in standard finite elements. A knot could be inserted multiple times – knot multiplicity (k) is the number of times a certain knot is inserted. The continuity between elements is of order C^{p-k} or C^{p-1} when there are no repeated knots.

2.3.2 Isogeometric analysis via Bézier extraction

Through multiple knot insertion in a procedure referred to as Bézier decomposition, a NURBS mesh can be decomposed into C^0-continuous Bézier elements (Figure 2.1), thereby providing an element structure that can be easily incorporated in existing finite element codes. This is achieved through a linear operator $\mathbf{C}$ such that:

$$\mathbf{N}(\xi) = \mathbf{C}\mathbf{B}(\xi) \tag{2.14}$$

where $\mathbf{N}$ contains the NURBS basis functions, $\mathbf{B}$ contains the Bézier basis functions, and $\mathbf{C}$ is termed the Bézier extraction operator. For each nonzero knot span, the NURBS curve is decomposed into C^0-continuous Bézier elements [24]. It follows from

eq.(2.13) that to represent any field variable using NURBS, the control point is replaced with any variable of interest:

$$\mathbf{X}(\xi,\eta) = \sum_{a=1}^{nA}\sum_{b=1}^{nB} x_{a,b} N_{a,b}^{p,q}(\xi,\eta) \tag{2.15}$$

where $\mathbf{X}$ is the variable of interest (e.g. displacement) and x is the value (displacement) at the control point. With this, both the geometry and solution of desired variables (analysis) use the same basis or shape functions.

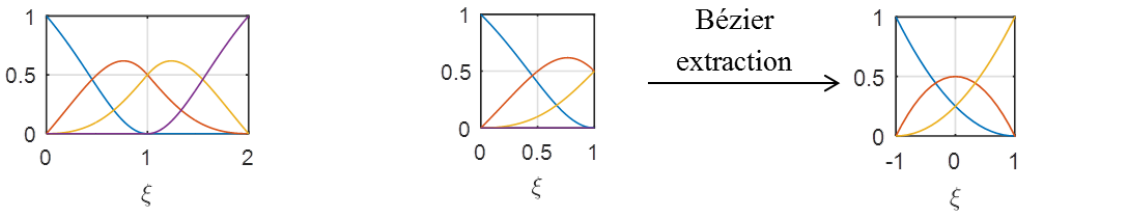

NURBS basis functions across domain (2 elements)

NURBS basis functions within element 1

Bézier element equivalent (parent domain)

Figure 2.1: Bézier decomposition and extraction for a quadratic NURBS curve with knot vector $\boldsymbol{\Xi} = \{0,0,0,1,2,2,2\}$. The interior knot divides the curve into two elements. A knot of value $\{1\}$ is inserted so that the multiplicity of the interior knot equals the polynomial degree, 2. Each element is then decomposed into equivalent Bézier curves which are C^0-continuous between elements. Through the Bézier extraction operator, the Bézier finite elements ensue and are used directly in analysis.

It is important to note that, notwithstanding Bézier extraction being local to the element, the C^{p-k}-continuity of NURBS is maintained within a single patch. However, when more than one patch is used to represent the geometry, special techniques need to be adopted to raise the C^0-continuity that exists between patches [50].

2.3.3 Spatial discretisation

Direct discretisation

The fourth-order equation – eq.(2.4) – can be written in Voigt matrix notation as follows:

$$(\mathbf{L}^T\mathbf{D}\mathbf{L})(\mathbf{u} - \ell^2\nabla^2\mathbf{u}) + \mathbf{b} = 0 \tag{2.16}$$

where $\nabla^2 \equiv \nabla^T \cdot \nabla$ is the Laplacian operator with $\nabla = [\frac{\partial}{\partial x}, \frac{\partial}{\partial y}, \frac{\partial}{\partial z}]^T$, and $\mathbf{L}$ is the differential operator:

$$\mathbf{L} = \begin{bmatrix} \frac{\partial}{\partial x} & 0 & 0 & \frac{\partial}{\partial y} & \frac{\partial}{\partial z} & 0 \\ 0 & \frac{\partial}{\partial y} & 0 & \frac{\partial}{\partial x} & 0 & \frac{\partial}{\partial z} \\ 0 & 0 & \frac{\partial}{\partial z} & 0 & \frac{\partial}{\partial x} & \frac{\partial}{\partial y} \end{bmatrix}^T \tag{2.17}$$

Eq.(2.16) is obtained directly by substituting the matrix-vector form of eq.(2.1),

$$\boldsymbol{\sigma} = \mathbf{D}(\boldsymbol{\varepsilon} - \ell^2 \nabla^2 \boldsymbol{\varepsilon}) \tag{2.18}$$

and the kinematic relation for small displacement gradients

$$\boldsymbol{\varepsilon} = \mathbf{L}\mathbf{u} \tag{2.19}$$

into the equilibrium equation in Voigt notation:

$$\mathbf{L}^T \boldsymbol{\sigma} + \mathbf{b} = \mathbf{0} \tag{2.20}$$

We recall that, unlike finite elements where variables are computed at the nodes, variables are computed at the control points in isogeometric analysis. Thus, the displacements $\mathbf{u} = [u_x, u_y, u_z]^T$ are related to the discrete displacements $\mathbf{a} = [a_{1x}, a_{1y}, a_{1z}, a_{2x}, a_{2y}, a_{2z}, \ldots]^T$ in the control points via:

$$\mathbf{u} = \mathbf{N}_u \mathbf{a} \tag{2.21}$$

where $\mathbf{N}_u$ is the matrix which contains the NURBS shape functions:

$$\mathbf{N}_u = \begin{bmatrix} N_1 & 0 & 0 & N_2 & 0 & 0 & \cdots & N_{ns} & 0 & 0 \\ 0 & N_1 & 0 & 0 & N_2 & 0 & \cdots & 0 & N_{ns} & 0 \\ 0 & 0 & N_1 & 0 & 0 & N_2 & \cdots & 0 & 0 & N_{ns} \end{bmatrix} \tag{2.22}$$

and ns is the number of shape functions at each control point. The number of rows corresponds to the number of degrees of freedom per control point.

To discretise eq.(2.16), we premultiply it by a test function $\tilde{\mathbf{u}}$ and integrate over the domain $\boldsymbol{\Omega}$:

$$\int_{\Omega} \tilde{\mathbf{u}}^T \Big[\mathbf{L}^T \mathbf{D} \mathbf{L} (\mathbf{u} - \ell^2 \nabla^2 \mathbf{u}) + \mathbf{b} \Big] d\Omega = 0 \tag{2.23}$$

The first term is integrated by parts and the use of Green's theorem yields [10]:

$$\begin{aligned} \int_{\Omega} \tilde{\boldsymbol{\varepsilon}}^T \mathbf{D} \boldsymbol{\varepsilon} d\Omega \; + \sum_{i=1}^{3} \int_{\Omega} \ell^2 \frac{\partial \tilde{\boldsymbol{\varepsilon}}^T}{\partial x_i} \mathbf{D} \frac{\partial \boldsymbol{\varepsilon}}{\partial x_i} d\Omega = \\ \int_{\Omega} \tilde{\mathbf{u}}^T \mathbf{b} d\Omega \; + \int_{\Gamma_n} \tilde{\mathbf{u}}^T \mathbf{t} d\Gamma + \sum_{i=1}^{3} \oint_{\Gamma} \ell^2 (\mathbf{n} \cdot \nabla \tilde{\mathbf{u}})^T \mathbf{D} \frac{\partial \boldsymbol{\varepsilon}}{\partial x_i} d\Gamma \end{aligned} \tag{2.24}$$

where $\mathbf{t}$ represents the prescribed tractions on the Neumann part of the boundary Γ_n and $\mathbf{n}$ is the normal vector to the boundary, cf. [127]. Next, the derivatives of $\tilde{\boldsymbol{\varepsilon}}$ are assumed to vanish on the boundary. Hence, the last term in eq.(2.24) vanishes.

In a Bubnov-Galerkin sense, the test and trial functions are discretised in the same space, so that

$$\tilde{\mathbf{u}} = \mathbf{N}_{\mathbf{u}} \tilde{\mathbf{a}} \tag{2.25}$$

Substituting eq.(2.25) into eq. (2.24), and requiring the result to hold for all admissible $\tilde{\mathbf{a}}$, the following ensues:

$$[\mathbf{K}_1 + \mathbf{K}_2] \mathbf{a} = \mathbf{f}^{ext} \tag{2.26}$$

where $\mathbf{K}_1$ is the standard stiffness matrix expressed as:

$$\mathbf{K}_1 = \int_{\Omega} \mathbf{B}^T \mathbf{D} \mathbf{B} d\Omega \tag{2.27}$$

and $\mathbf{B} = \mathbf{L}\mathbf{N}_u$. The higher order derivatives of the shape functions are assembled in $\mathbf{K}_2$ and are given by:

$$\mathbf{K}_2 = \sum_{i=1}^{3} \int_{\Omega} \ell^2 \frac{\partial \boldsymbol{B}^T}{\partial x_i} \mathbf{D} \frac{\partial \boldsymbol{B}}{\partial x_i} d\Omega \tag{2.28}$$

The external force vector $\mathbf{f}^{ext}$ reads:

$$\mathbf{f}^{ext} = \int_{\Omega} \mathbf{N_u}^T \mathbf{b} d\Omega \; + \int_{\Gamma_n} \mathbf{N_u}^T \mathbf{t} d\Gamma \tag{2.29}$$

As evident from eq.(2.26), C^1-continuous shape functions are required since second spatial derivatives have to be computed. This is provided automatically by the NURBS shape functions which are used in isogeometric analysis. The finite element implementation via Bézier extraction is achieved using the Jive open source C++ library [42].

Operator split: One-way coupling

An alternative approach is to split the fourth-order partial differential equation into a sequence of two second-order partial differential equations. In matrix-vector format, this is expressed as:

$$\mathbf{L}^T\mathbf{D}\mathbf{L}\mathbf{u}^c + \mathbf{b} = 0 \tag{2.30}$$

$$\mathbf{u} - \ell^2\nabla^2\mathbf{u} = \mathbf{u}^c \tag{2.31}$$

cf. eqs. (2.5) and (2.6). After resolution of eq.(2.30), eq.(2.31) can be solved for the non-local displacements $\mathbf{u}$.

To discretise eq.(2.30), we first premultiply it by the test function $\tilde{\mathbf{u}}^c$ and integrate by parts to obtain the weak form:

$$\int_\Omega (\mathbf{L}\tilde{\mathbf{u}}^c)^T\mathbf{D}\mathbf{L}\mathbf{u}^c d\Omega = \int_\Omega (\tilde{\mathbf{u}}^c)^T\mathbf{b}d\Omega \; + \int_{\Gamma_n} (\tilde{\mathbf{u}}^c)^T\mathbf{t}d\Gamma \tag{2.32}$$

where $\mathbf{t}$ are the prescribed tractions on the Neumann part of the boundary Γ_n. The test function and trial functions are discretised as in the previous section using NURBS shape functions:

$$\tilde{\mathbf{u}}^c = \mathbf{N}_\mathbf{u}\tilde{\mathbf{a}}^c \tag{2.33}$$

$$\mathbf{u}^c = \mathbf{N}_\mathbf{u}\mathbf{a}^c \tag{2.34}$$

where $\tilde{\mathbf{a}}^c$ and $\mathbf{a}^c$ are the displacements at the control points. For eq.(2.32) to hold for any $\tilde{\mathbf{a}}^c$, we derive:

$$\int_\Omega \mathbf{B}^T\mathbf{D}\mathbf{B}d\Omega\, \mathbf{a}^c = \mathbf{f}^{ext} \tag{2.35}$$

with $\mathbf{f}^{ext}$ the external force. $\mathbf{K}_1$ and $\mathbf{B}$ represent the standard stiffness and strain-displacement matrices, respectively, defined in the previous section.

Eq.(2.31) can also be expressed in terms of strains pre-multiplied by **DL**. This renders a stress form of the equation [13]:

$$\boldsymbol{\sigma} - \ell^2 \nabla^2 \boldsymbol{\sigma} = \mathbf{D}\mathbf{L}\mathbf{u}^c \tag{2.36}$$

With the use of a test function $\tilde{\boldsymbol{\sigma}}$, one obtains the weak form:

$$\int_\Omega \left[\tilde{\boldsymbol{\sigma}}^T \boldsymbol{\sigma} \; + \ell^2 \sum_{i=1}^{3} \int_\Omega \frac{\partial \tilde{\boldsymbol{\sigma}}^T}{\partial x_i} \frac{\partial \boldsymbol{\sigma}}{\partial x_i} \right] d\Omega - \oint_\Gamma \tilde{\boldsymbol{\sigma}}^T \ell^2 (\mathbf{n} \cdot \nabla \boldsymbol{\sigma}) d\Gamma = \int_\Omega \tilde{\boldsymbol{\sigma}}^T \mathbf{D}\mathbf{L}\mathbf{u}^c d\Omega \tag{2.37}$$

where $\mathbf{n}$ is the normal vector to the boundary Γ. Assuming natural boundary conditions ($\mathbf{n} \cdot \nabla \boldsymbol{\sigma} = 0$) implies that the boundary integral term vanishes. When the usual essential boundary condition is applied, i.e. $\boldsymbol{\sigma} = \boldsymbol{\sigma}^c$, we have $\tilde{\boldsymbol{\sigma}} = \mathbf{0}$, and again, the boundary integral term vanishes.

Discretisation is achieved using the shape functions for the stresses:

$$\boldsymbol{\sigma} = \mathbf{N}_\sigma \mathbf{s} \tag{2.38}$$

$$\tilde{\boldsymbol{\sigma}} = \mathbf{N}_\sigma \tilde{\mathbf{s}} \tag{2.39}$$

where $\mathbf{s}$, $\tilde{\mathbf{s}}$ are control point variables. For three spatial dimensions, $\mathbf{N}_\sigma$ is a 6-row matrix which is an extension of the 3-row matrix $\mathbf{N}_\mathbf{u}$:

$$\mathbf{N}_\sigma = \begin{bmatrix} N_1 & 0 & 0 & 0 & 0 & 0 & N_2 & 0 & 0 & 0 & 0 & 0 & \cdots \\ 0 & N_1 & 0 & 0 & 0 & 0 & 0 & N_2 & 0 & 0 & 0 & 0 & \cdots \\ 0 & 0 & N_1 & 0 & 0 & 0 & 0 & 0 & N_2 & 0 & 0 & 0 & \cdots \\ 0 & 0 & 0 & N_1 & 0 & 0 & 0 & 0 & 0 & N_2 & 0 & 0 & \cdots \\ 0 & 0 & 0 & 0 & N_1 & 0 & 0 & 0 & 0 & 0 & N_2 & 0 & \cdots \\ 0 & 0 & 0 & 0 & 0 & N_1 & 0 & 0 & 0 & 0 & 0 & N_2 & \cdots \end{bmatrix} \tag{2.40}$$

Eq.(2.37) is therefore discretised as [16]:

$$\int_\Omega \left[{\mathbf{N}_\sigma}^T \mathbf{N}_\sigma \; + \ell^2 \sum_{i=1}^{3} \int_\Omega \frac{\partial {\mathbf{N}_\sigma}^T}{\partial x_i} \frac{\partial \mathbf{N}_\sigma}{\partial x_i} \right] d\Omega \, \mathbf{s} = \int_\Omega {\mathbf{N}_\sigma}^T \mathbf{D}\mathbf{B} d\Omega \, \mathbf{a}^c \tag{2.41}$$

This discretisation is also implemented via Bézier extraction using the Jive C++ library. $\mathbf{N}_\sigma$ and $\mathbf{N}_\mathbf{u}$ could in principle be chosen independently but the requirement in

this case is only C^0-continuity for the shape functions. This is one attractive attribute of the Ru-Aifantis theorem which propelled its application to remove singularities in crack problems [16].

It is important to note that the second reaction-diffusion equation is associated with nonlocal or gradient-enriched strains and thus, the related gradient-enriched stresses are not necessarily in equilibrium [11, 13]. This was also pointed out by [82] where it was argued that the operator split is only valid where the body under consideration is infinite, eliminating the need to enforce any boundary conditions.

2.4 Errors and Convergence rates

To determine the convergence rate, the L_2 norm of the stress error is considered:

$$\|e\|_{L_2} = \left[\int_{\Omega} (\boldsymbol{\sigma} - \hat{\boldsymbol{\sigma}})^T (\boldsymbol{\sigma} - \hat{\boldsymbol{\sigma}}) \right]^{\frac{1}{2}} d\Omega \tag{2.42}$$

where $\boldsymbol{\sigma}$ is the exact solution and $\hat{\boldsymbol{\sigma}}$ is the approximated solution. For 2D classical elasticity, the theoretical convergence rate for the stress based on the total number of the degrees of freedom ($nDOF$) is $O(nDOF^{-\frac{p}{2}})$; based on a defined mesh-parameter (h), it is $O(h^p)$ for a polynomial order of p. Prior to gradient elasticity, the convergence rates for classical elasticity are briefly presented.

A plane-strain, thick hollow cylinder subjected to external pressure is considered [50, 147]. Only a quarter of the cylinder is analysed due to symmetry (shaded region in Figure 2.2). The problem is illustrated in Figure 2.2 where $r_i = 0.05$ m is the inner radius, $r_o = 0.5$ m is the outer radius and $P = 1.0$ MPa is the applied external pressure. Young's modulus, $E = 8100$ MPa and Poisson's ratio, $\nu = 0.35$.

2.4.1 Classical elasticity

In this case where the length scale $\ell = 0$, it suffices to restrict the x-displacement [u_x(0,y)=0] at the left end and the y-displacement [$u_y(x, 0)$=0] at the bottom to achieve symmetry. Six meshes with $2^k \times 2^k$ elements, $k = 2 - 7$ have been considered. Three polynomial orders of the NURBS shape functions have been investigated: $p = 2, 3, 4$. The exact solution (plane-strain) is [57]:

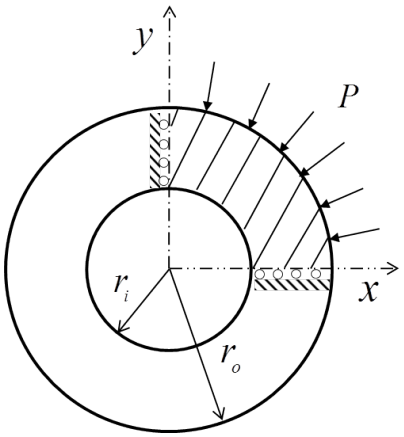

Figure 2.2: Geometry and boundary conditions for a thick-walled cylinder subjected to an external pressure, P

$$
\begin{aligned}
u_r &= -(1+\nu)\frac{Prr_o^2}{E(r_o^2-r_i^2)}\left\{1-2\nu+\frac{r_i^2}{r^2}\right\} \\
\sigma_{rr} &= \frac{Pr_o^2}{r_o^2-r_i^2}\left(\frac{r_i^2}{r^2}-1\right) \\
\sigma_{\theta\theta} &= \frac{Pr_o^2}{r_o^2-r_i^2}\left(\frac{r_i^2}{r^2}+1\right)
\end{aligned}
\tag{2.43}
$$

The results are presented in Figure 2.3 where h_{max} is the maximum diagonal between two opposite knot locations in the physical space. It is apparent from the computed convergence rates, denoted by m, that the theoretical predictions are obtained. For example, the values of $m \approx -1.5 = -\frac{p}{2}$ and $m \approx 3 = p$ are obtained in the case of cubic NURBS ($p = 3$) considering total degrees of freedom ($nDOF$) and mesh parameter (h_{max}) respectively.

While the fourth order (direct) equation for the cylinder has an exact solution [147], for the set of second order equations, the solution can only be approximated [16]. This has been achieved using Richardson extrapolation [119], which involves using the solution of three (uniformly refined) meshes to approximate the exact solution. For a quadrilateral, it is required that each successive mesh doubles the number of elements in each direction, see Figure 2.4. Indeed the solution is approximated at points present in all three meshes (red boxes in Figure 2.4) as:

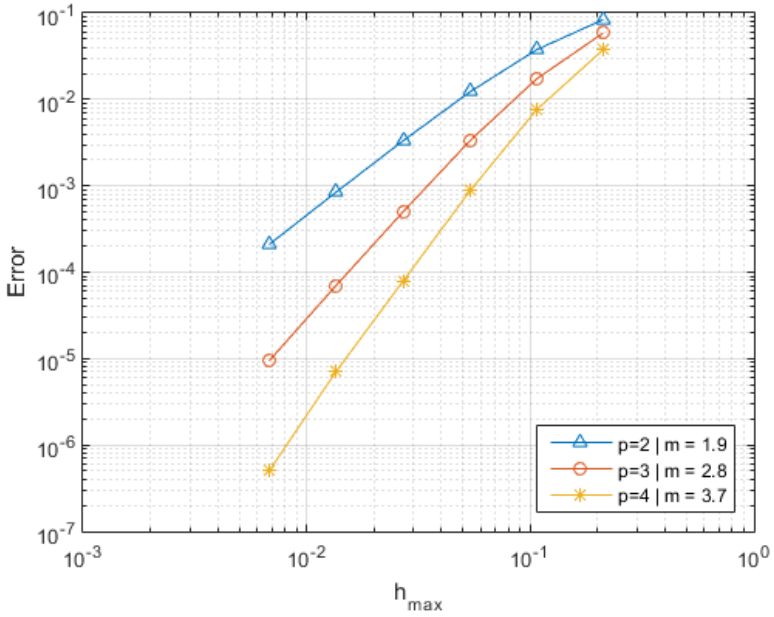

(a)

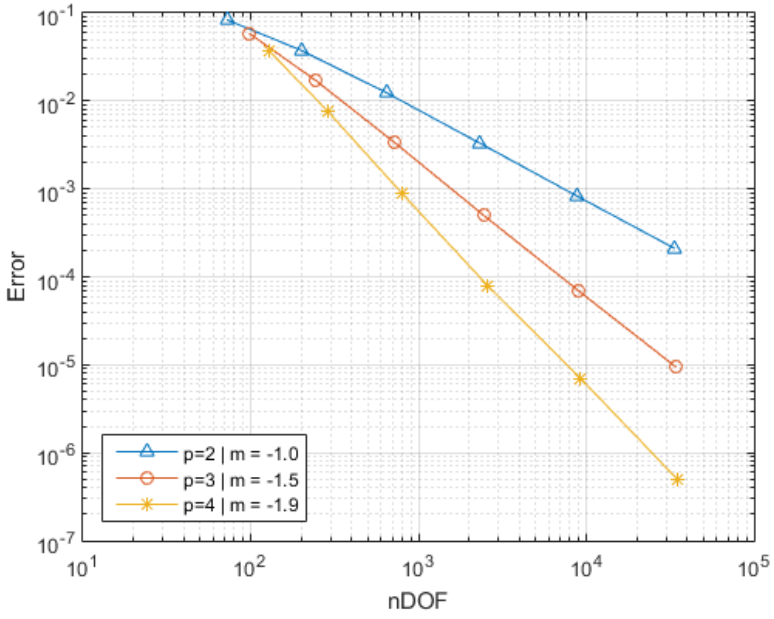

(b)

Figure 2.3: L^2 norm of the stress error against: (a) maximum mesh parameter; (b) total number of degrees of freedom for quadratic ($p = 2$), cubic ($p = 3$) and quartic NURBS ($p = 4$). Convergence rate is the slope (m). Results are for classical elasticity.

$$f_{exact}(i,j) = \frac{1}{3} f_{\Delta x}(i,j) - 2 f_{\frac{\Delta x}{2}}(i,j) + \frac{8}{3} f_{\frac{\Delta x}{4}}(i,j) \tag{2.44}$$

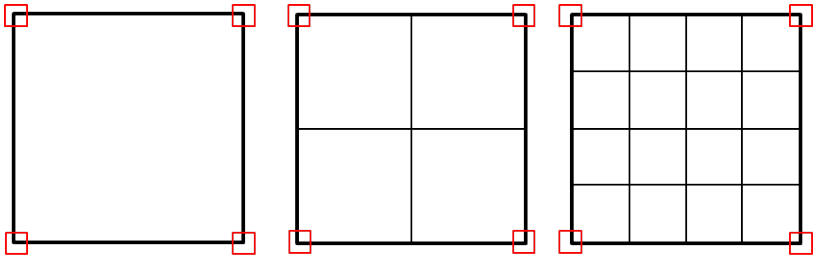

(a) (b) (c)

Figure 2.4: Richardson extrapolation. Three meshes: (a) $f_{\Delta x}$, (b) $f_{\frac{\Delta x}{2}}$, (c)$f_{\frac{\Delta x}{4}}$ are used to approximate the solution of a second order partial differential equation. The approximation points of interest (red boxes) must be present in all meshes.

Since Richardson extrapolation is mesh-based, variables are involved at vertex points rather than at integration points. A suitable error estimation technique is provided by the L_2-relative norm of the stress [16]:

$$\|e\|_{L_2-relative} = \sqrt{\frac{\sum_{i=1}^{nDOF} (\sigma_i^e - \sigma_i^c)^2}{\sum_{i=1}^{nDOF} (\sigma_i^e)^2}} \tag{2.45}$$

where σ^e is the exact solution, σ^c is the numerical solution and $nDOF$ is the total number of stress components. Note that for the set of second-order equations, this is the total degrees of freedom in the discretisation of the second partial differential equation. The results based on Richardson extrapolation for classical elasticity are shown in Figure 2.5. The three finest meshes are used in approximating the solution. Again, from the slopes which represent the convergence rates, the theoretical values are retrieved fairly well. It is observed that use of the exact solution leads to slightly better results. The existence of an exact solution only for the direct and not the staggered solution approach, is another indication that the staggered approach is not equivalent to the direct approach [13].

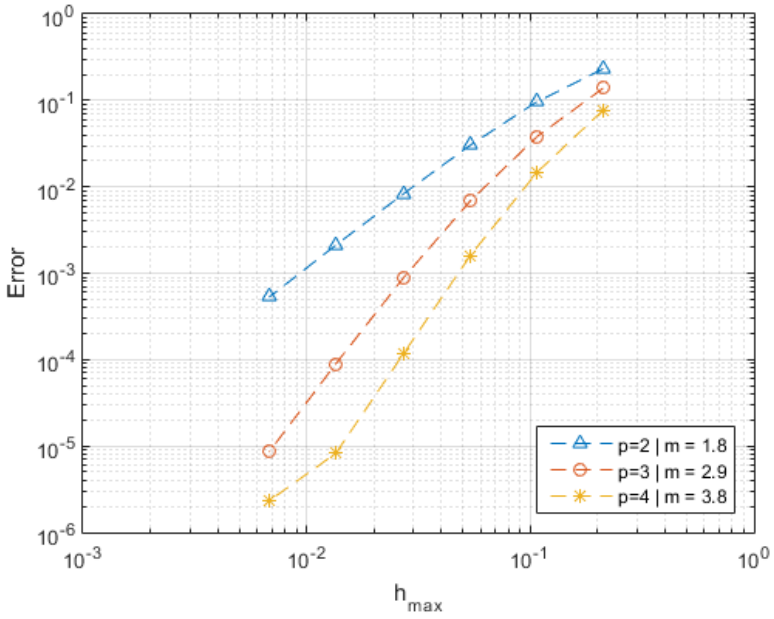

(a)

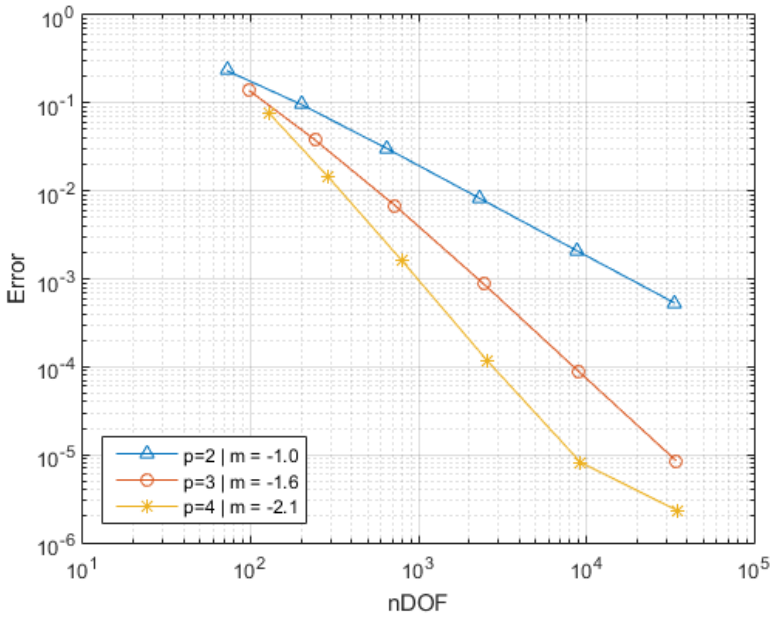

(b)

Figure 2.5: L^2-relative norm of the stress error against: (a) mesh parameter; (b) total number of degrees of freedom for quadratic ($p = 2$), cubic ($p = 3$) and quartic NURBS ($p = 4$). The slope (m) represents the convergence rate. Richardson extrapolation is used to approximate the exact solution. Results are for classical elasticity.

2.4.2 Gradient elasticity

The length scale parameter is taken as $\ell = 0.01$ m. Additional boundary conditions must be imposed at the left and at the bottom [147]. The set of control points immediately next to the boundaries are used as follows [50]:

$$\begin{aligned} &\frac{\partial u_y}{\partial x} = 0; \quad \text{enforced as} \quad u_y(2,j) = u_y(1,j) \quad \text{at the left boundary} \\ &\frac{\partial u_x}{\partial y} = 0; \quad \text{enforced as} \quad u_x(i,2) = u_x(i,1) \quad \text{at the bottom boundary} \end{aligned} \tag{2.46}$$

where $i = \{1, 2, ...\}$ (from left to right) and $j = \{1, 2, ...\}$ (from bottom to top) are the respective x and y indices of the control points at each boundary. When the operator split is used, the first equation maintains the same boundary conditions as described for classical elasticity. In the second equation, which solves for the stresses that include the gradient effect, the additional fourth-order boundary condition is imposed as $\tau_{xy} = 0$ on the left and bottom boundaries while a Neumann boundary condition is maintained elsewhere, i.e. $\mathbf{n} \cdot \nabla \boldsymbol{\sigma} = 0$ where $\boldsymbol{\sigma} = [\sigma_{xx}, \sigma_{yy}, \tau_{xy}]^T$.

The exact solution for the fourth-order partial differential equation is given in [147] while the solution for the case with operator split (staggered approach) is approximated using Richardson extrapolation. The results based on error estimates discussed in the previous section are shown in Figure 2.6. The relative L^2-error norm of the stresses is used for the staggered approach while the L^2-error norm is used for the fourth-order partial differential equation (direct discretisation). The results suggest that Richardson extrapolation may not be fully appropriate for obtaining a reference solution.

On the other hand, the solutions for the direct case show the same convergence rate as with classical elasticity. It is noted that in estimating the convergence rates, emphasis has been placed on points along the major trend line. Another point of interest is the comparison of the convergence rates for the direct and the staggered approaches. The classical elasticity solution applies in this case to the first step of the staggered approach. Results are presented in Figure 2.7 using the L^2-norm of displacement error. The theoretical convergence rate for displacement is $O(h^{p+1})$ or based on the degrees of freedom, $O(nDOF^{-\frac{p+1}{2}})$, where p is the polynomial order [150]. Results in Figure 2.7 show a close match with theoretical prediction especially for $p = 3$ and $p = 4$. Gradient

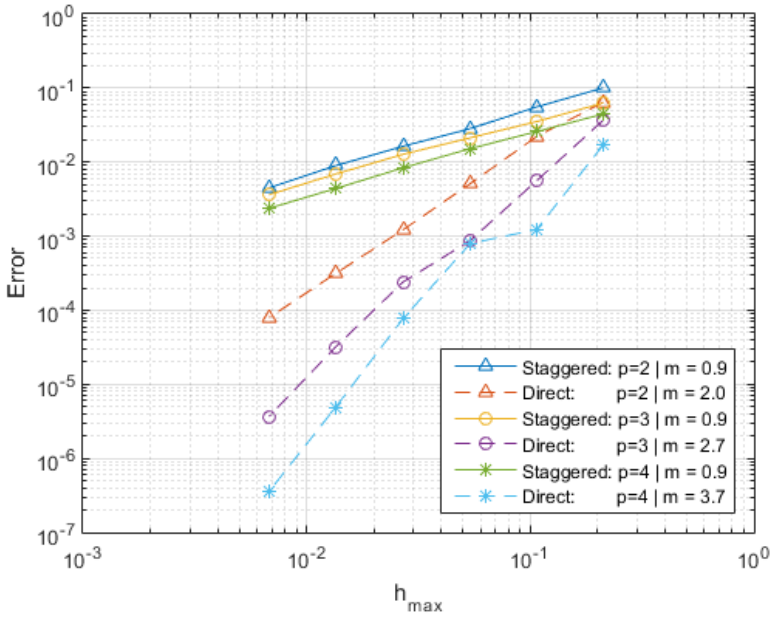

(a)

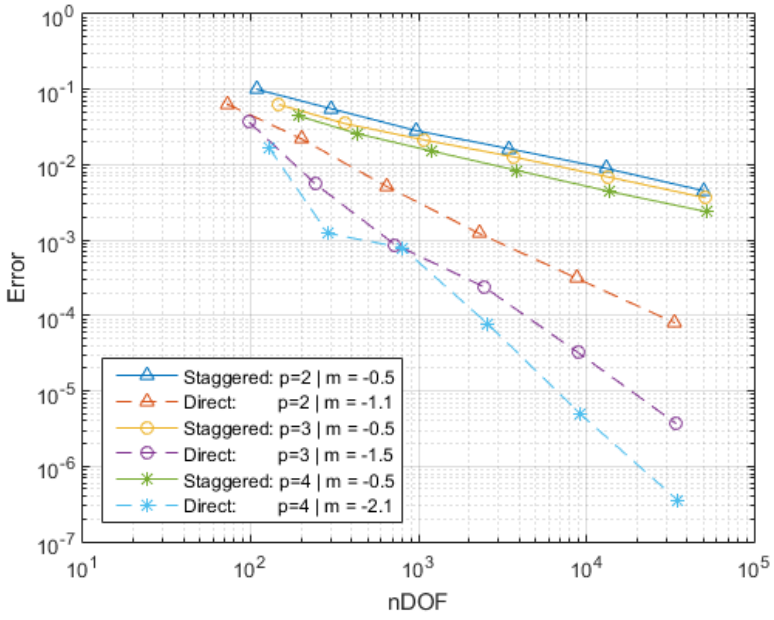

(b)

Figure 2.6: Error in the stress against: (a) mesh parameter; (b) total number of degrees of freedom for quadratic ($p = 2$), cubic ($p = 3$) and quartic NURBS ($p = 4$). The slope (m) represents the convergence rate. While the exact solution of the fourth order partial differential equation (Direct) is based on the exact solution, the solution for the approach with the operator split (Staggered) is based on Richardson extrapolation.

elasticity (Direct) has a suboptimal convergence rate (m) for $p = 2$ but when $p = 4$, m for the gradient case surpasses that of classical elasticity (Staggered). This indicates that, for both cases, the theoretical prediction holds. The suboptimal convergence rate observed for the direct discretisation is in accordance with the explanation given by Kästner et al. [69]. Considering a linear fourth-order partial differential equation for an infinitely continuous reference solution ($r = \infty$), the convergence rate is given by:

$$\|u - \hat{u}\|_{H^0 \equiv L^2} \leq C_0 h^{min\{p+1, 2(p-1)\}} \|u\|_{H^r} \tag{2.47}$$

where u is the exact displacement, $\hat{u}$ is the numerical solution and p is the polynomial order. Optimal convergence rate is thus the minimum of $\{p + 1, 2(p - 1)\}$ which is $2(p - 1) = 2$ for a polynomial order of two. This is in line with the result depicted in Figure 2.7(a).

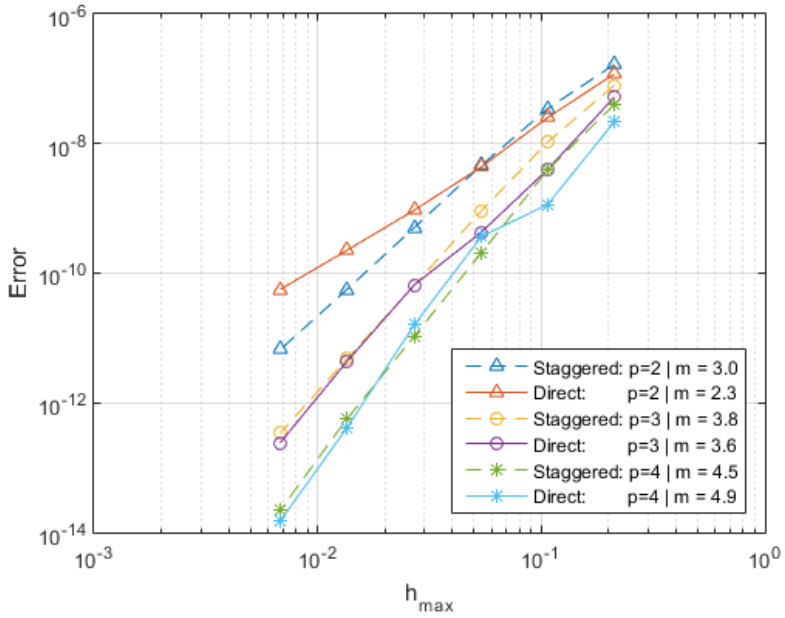

(a)

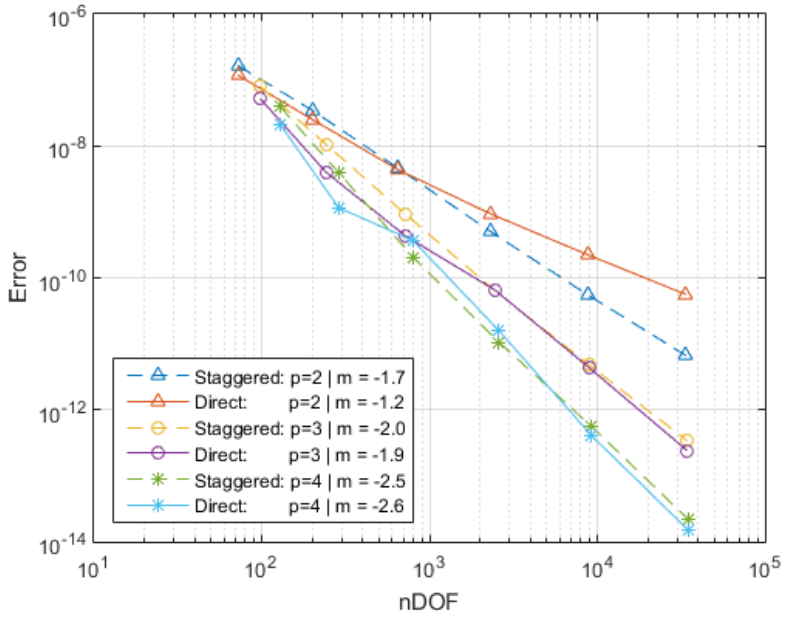

(b)

Figure 2.7: L^2 norm of the displacement error against: (a) maximum mesh parameter; (b) total number of degrees of freedom for quadratic ($p = 2$), cubic ($p = 3$) and quartic NURBS ($p = 4$). The slope (m) is the convergence rate.

2.5 Gradient elasticity with T-Splines

2.5.1 T-splines and T-mesh

The T-spline technology is based on the notion of a T-mesh [124, 126] which is composed of quadrilateral-shaped elements [124, 125] in two-dimensions (Figure 2.8). Each element in the T-mesh has one or more edges split by T-junctions. T-junctions are analogous to hanging nodes in finite elements where an internal node has less than four linked neighbours. Each T-vertex is associated with a control point and control weight. Valid knot intervals are defined which ensure that opposite sides of an element in the T-mesh have knot intervals summing to the same value (i.e. $a_1 + a_2 = b$ in Figure 2.8).

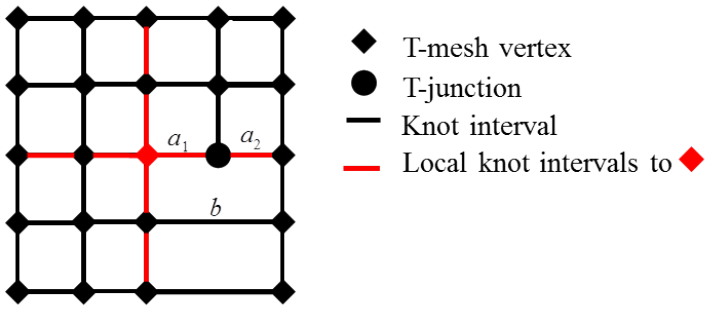

Figure 2.8: Illustration of T-mesh and local knot intervals, p=3

To define the T-spline basis function, local knot interval vectors are used. Unlike NURBS, T-splines are not based on a global tensor product. Each vertex has its local interval vector which is a sequence of knot intervals, $\mathbf{\Delta\Xi} = \{\Delta\xi_1, \Delta\xi_2, \ldots, \Delta\xi_{p+1}\}$ such that $\Delta\xi_i = \xi_{i+1} - \xi_i$ [124], where p is the polynomial degree $(p+1 = 4)$. A set of local knot intervals for each vertex A is constructed by moving in each topological direction from the vertex until $p - 1 = 2$ vertices or perpendicular edges are intersected. In the case where a T-mesh boundary is crossed before $p - 1 = 2$ knot intervals are intersected, the local knot interval is set to zero. This makes the T-mesh boundary to have open knot vectors.

From the local knot interval vectors, a local knot vector is defined as $\mathbf{\Xi}_\mathrm{A} = \{\Xi_A^i\}_{i=1}^d$ and $\Xi_A^i = \{\xi_1^i, \xi_2^i, \ldots, \xi_{p+2}^i\}$ where $\xi_1^i = 0, \xi_2^i = \Delta\xi_1^i$ and for $n \geq 3$, $\xi_n^i = \Delta\xi_{n-1}^i + \Delta\xi_{n-2}^i + \ldots + \Delta\xi_1^i$. Each T-spline basis function is defined over a local basis function domain

$\hat{\boldsymbol{\Omega}}_A \in \mathbb{R}^d$ by the local knot vector:

$$\hat{\boldsymbol{\Omega}}_A = \bigotimes_{i=1}^{d} \hat{\Omega}_A^i \tag{2.48}$$

where $\hat{\Omega}_A^i = \left[0, \Delta\xi_{p+1}^i + \ldots + \Delta\xi_2^i + \Delta\xi_1^i\right] \subset \mathbb{R}$ for polynomial degree (p). A coordinate system called the basis coordinate system is defined for each local basis function: $\boldsymbol{\xi}_\mathrm{A} = (\xi_A^1, \xi_A^2) = (\xi_A, \eta_A)$. With this localisation, the basis function of a T-spline is defined over each local basis function domain in the same way as NURBS, by employing Cox-de-Boor recursion formula. Also, Bézier extraction is extensible to T-splines [125].

2.5.2 Thick hollow cylinder subjected to external pressure

The problem of a thick hollow cylinder subjected to external pressure is revisited. The T-spline geometry generated using the Rhino T-Spline plug-in [15] is presented in Figure 2.9. Both classical and gradient elasticity are considered. For the additional boundary condition required in gradient elasticity, the immediate vertex after the boundary is used as with NURBS. Two finer meshes have been generated to qualitatively show the errors in the displacement, see Figure 2.10. Evidently, the convergence rate is similar to that obtained with NURBS but T-splines are more efficient since less degrees of freedom are used to obtain a given error level. A representative plot of σ_{xx} is presented in Figure 2.11 for the direct and the staggered approach. Slight differences can be observed close to the inner boundary.

2.5.3 L-shaped panel subjected to traction

An L-shaped panel subjected to traction is considered next, Figure 2.12. The length and traction are $a = 30$ m and $t = 1$ MPa respectively. Essential boundary conditions are imposed as displacements on the top ($u_y = 0$) and right edge ($u_x = 0$). As in the previous problem, $E = 8100$ MPa, $\nu = 0.35$ and $\ell = 0.01$ m. The T-mesh with local refinement is depicted in Figure 2.12(b). This illustrates the flexibility of T-splines, and the ensuing lower computational cost.

The three stress components using direct discretisation and using the operator split are shown in Figure 2.13. There is only a slight variation in the stress distribution

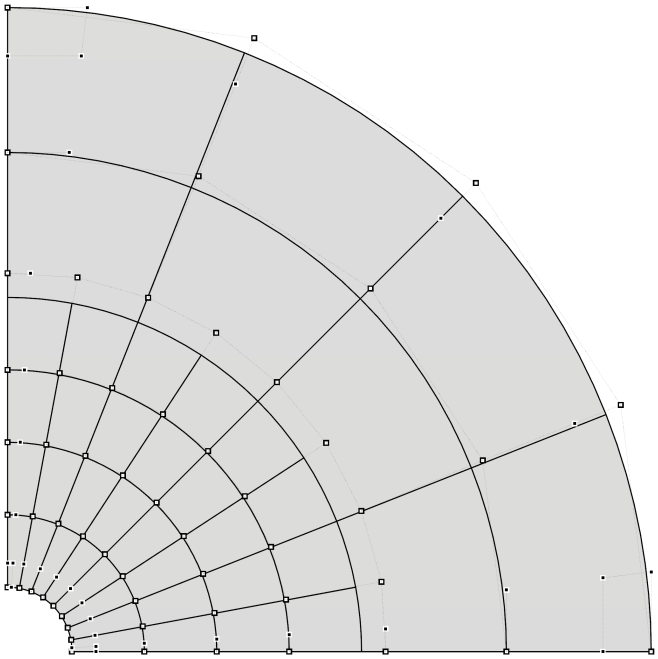

Figure 2.9: T-Spline representation of quarter cylinder.

between the two discretisation schemes. The difference is minimal due to absence of any boundary condition required in the second step of the operator-split approach. This is in line with the argument that the latter works best when there is no need to impose boundary conditions [82], i.e. $\mathbf{n} \cdot \nabla \boldsymbol{\sigma} = 0$ everywhere.

The effect of varying the length scale parameter (ℓ) on σ_{xy} is shown in Figure 2.14. For lower values of ℓ, the region of high stress is obviously more localised. Results are presented for both discretisation schemes. It is noted that even when $\ell = 0$, the stress contours are not exactly identical. This could be attributed to the difference in discretised variable – while displacement is discretised in the direct approach, the stress is discretised in the staggered approach.

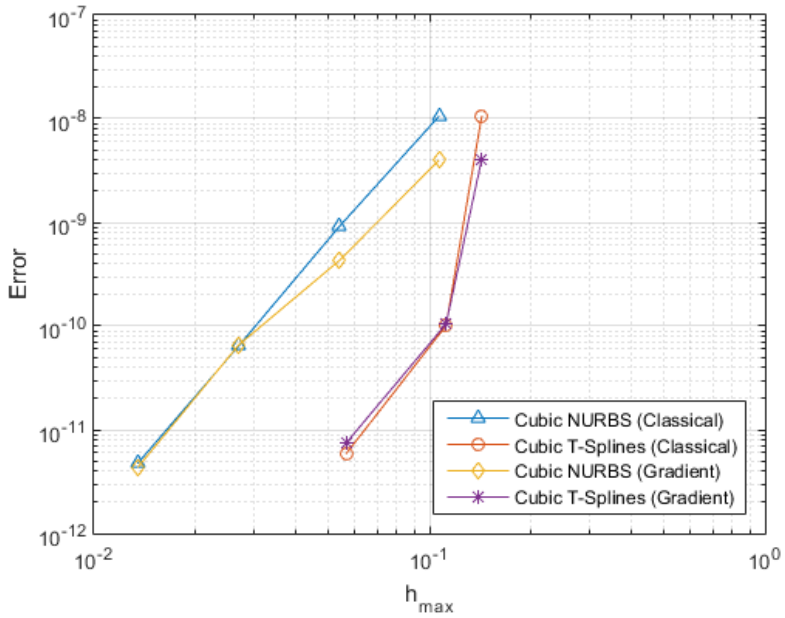

(a)

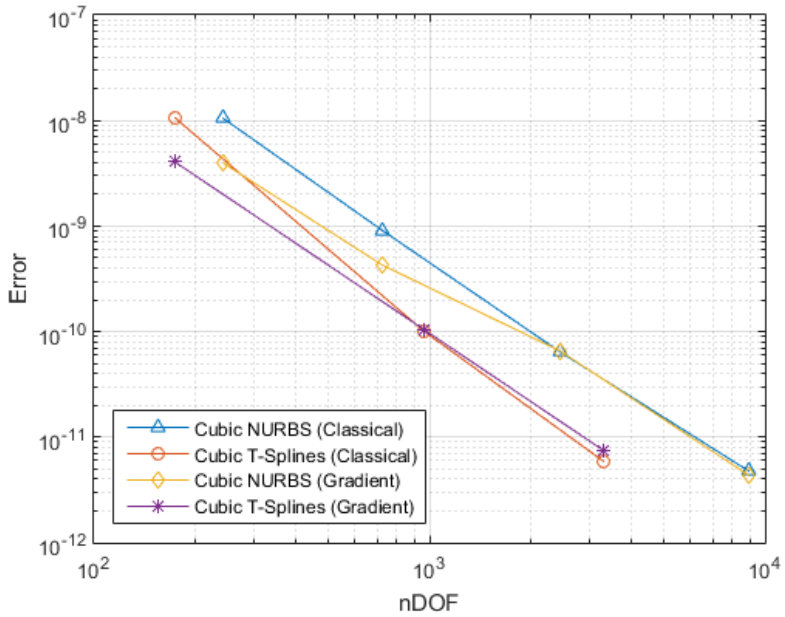

(b)

Figure 2.10: L^2 norm of the displacement error against: (a) maximum mesh parameter; (b) total number of degrees of freedom for cubic NURBS and T-Splines.

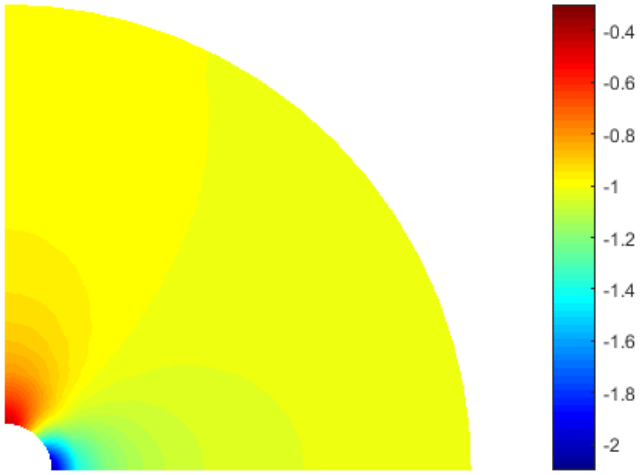

(a)

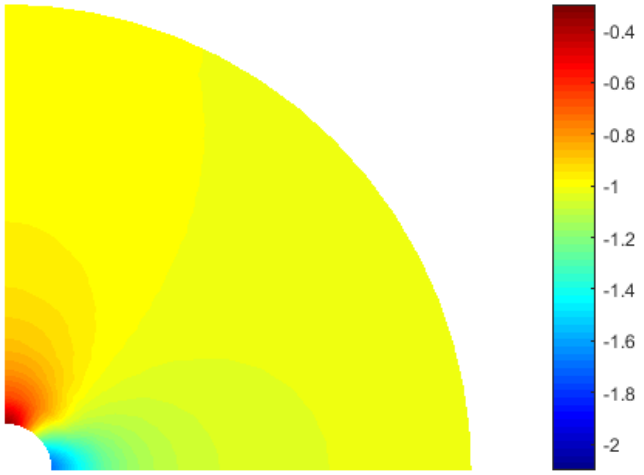

(b)

Figure 2.11: σ_{xx}-components of stress [MPa]: (a) direct discretisation; (b) staggered approach.

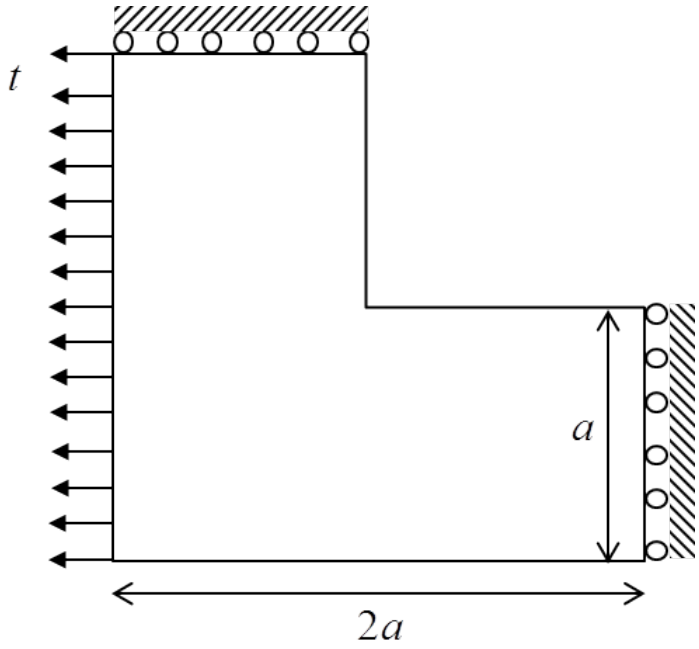

(a)

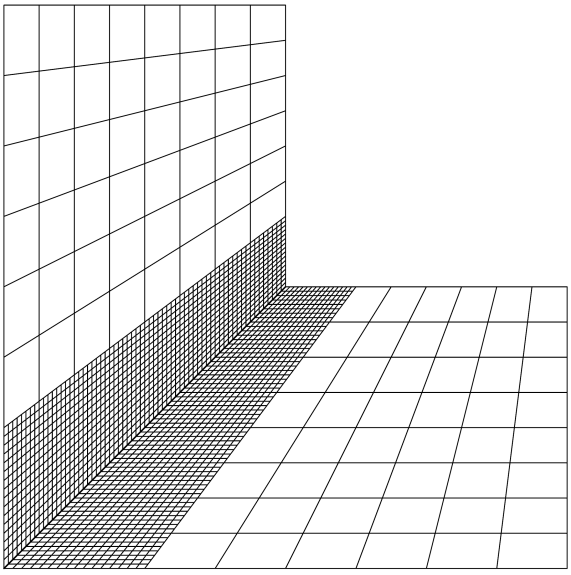

(b)

Figure 2.12: L-shaped panel: (a) Geometry and boundary conditions; (b) T-mesh.

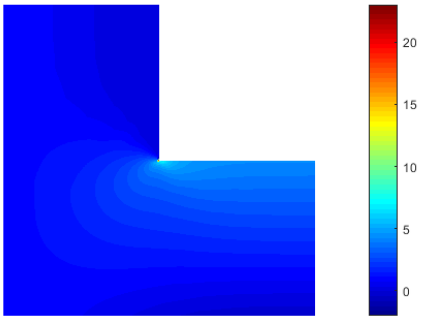

(a) σ_{xx} direct

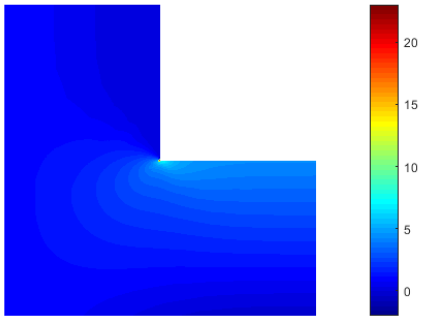

(b) σ_{xx} staggered

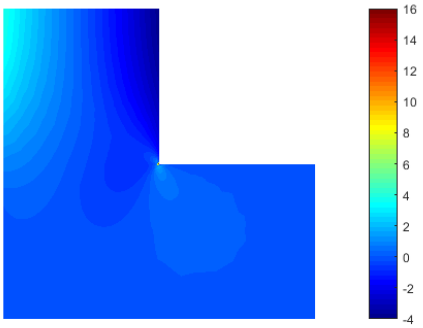

(c) σ_{yy} direct

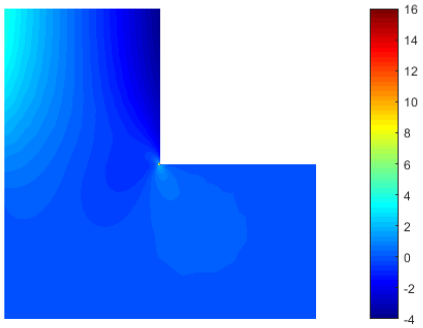

(d) σ_{yy} staggered

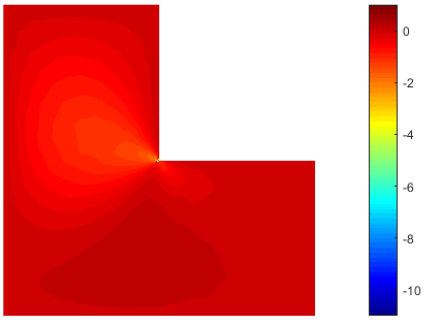

(e) σ_{xy} direct

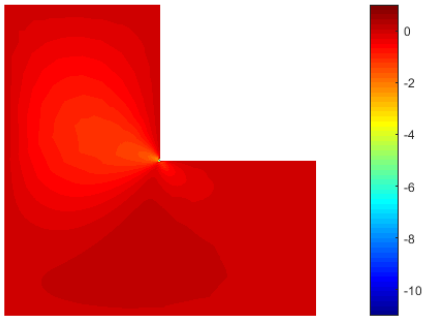

(f) σ_{xy} staggered

Figure 2.13: Stresses [MPa] in L-shaped panel using the Staggered – $(\cdot)^S$ and Direct – $(\cdot)^D$ approaches: (a) σ^D_{xx}; (b) σ^S_{xx}; (c) σ^D_{yy}; (d) σ^S_{yy}; (e) σ^D_{xy}; (f) σ^S_{xy}. Lenth scale ℓ = 0.01 m

.

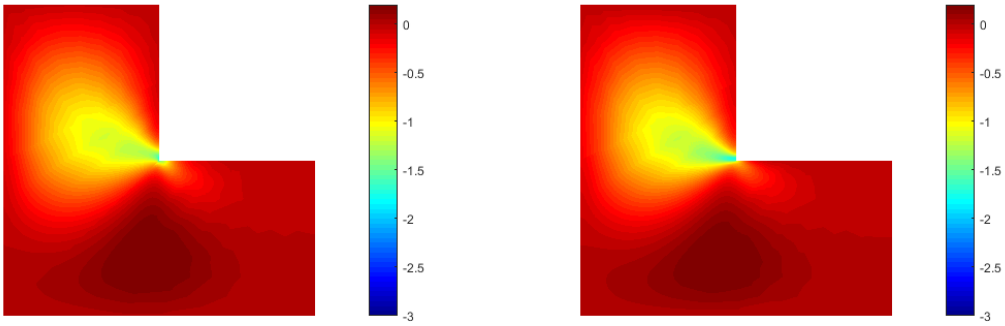

(a) direct ℓ = 1.0 m

(b) staggered ℓ = 1.0 m

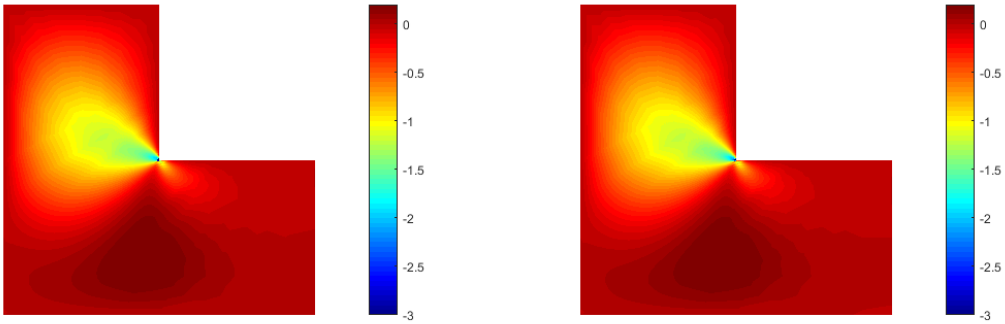

(c) direct ℓ = 0.1 m

(d) staggered ℓ = 0.1 m

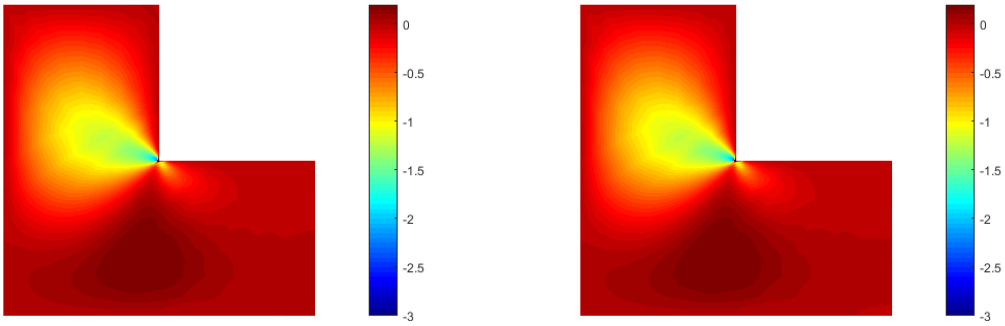

(e) direct ℓ = 0.0 m

(f) staggered ℓ = 0.0 m

Figure 2.14: σ_{xy} [MPa] distribution in L-shaped panel with varying length scales (ℓ) for Staggered – $(\cdot)^S$ and Direct – $(\cdot)^D$ approach: (a) $\ell^D = 1.0$ m; (b) $\ell^S = 1.0$ m; (c) $\ell^D = 0.1$ m; (d) $\ell^S = 0.1$ m; (e) $\ell^D = 0.0$ m; (f) $\ell^S = 0.0$ m.

2.6 Conclusion

This chapter presents a convergence analysis of the Laplacian-based gradient elasticity theory. Both direct discretisation of the fourth-order partial differential equation and an operator split approach have been considered. The analyses have been carried out in an isogeometric framework for global refinement using NURBS shape functions, and for local refinement using T-splines. These shape functions naturally provide the smoothness required for the direct discretisation of the fourth-order partial differential equation. Direct discretisation shows better convergence rates for polynomial orders greater than two and follows theoretical predictions. For a polynomial order equal to two, recent results for the (fourth-order) Cahn-Hilliard equation are confirmed, i.e. that the convergence rate is suboptimal [43]. Results from the numerical examples support the argument that, strictly speaking, the opera- tor split approach only applies to an infinite body where boundary conditions do not need to be imposed.

In this chapter, we have studied a gradient elasticity formulation which can remove singularities as illustrated using an L-shaped geometry. In the next chapter, a different motivation for gradient enhancement is considered – obtaining mesh-objective results for softening plasticity.

Chapter 3

AN ISOGEOMETRIC ANALYSIS APPROACH TO GRADIENT-DEPENDENT PLASTICITY[1]

3.1 Introduction

In the numerical analysis of strain-softening solids, the use of conventional rate-independent constitutive models can lead to mesh-dependent results. This is because strain softening triggers the development of localised zones, and the absence of an internal length scale in conventional strain-softening models makes these localisation bands to have a zero width. As a consequence, the width of the localised zone that results from simulations equals the smallest width allowed by the discretisation. The origin of the problem lies in the governing boundary value problem which becomes ill-posed at the onset of strain softening, or in some cases when stress-strain relations with a non-symmetric tangential operator are employed, possibly in combination with a large-strain description. In quasi-static problems the character of the partial differential equations then locally changes from elliptic into hyperbolic, giving rise to the possibility of displacement discontinuities [18, 35, 36, 39].

Among other approaches, higher-order continuum theories, which incorporate a material length scale, can maintain well-posedness, even when a localisation zone develops. Thus, they can offer a regularisation of the governing field equations. Gradient plasticity models form one class of such theories. It is noted that some works have also tried to address the problem using gradient elasticity and/or classical plasticity [23, 79, 90, 120]. The regularisation technique adopted in [79] to solve mesh dependency succeeded in the initial post peak, but stress locking and lack of clear conver-

[1]Based on: I. Kolo and R. de Borst. An isogeometric analysis approach to gradient-dependent plasticity. *International Journal for Numerical Methods in Engineering*, 113(2):296–310, 2018

gence were observed in the far post peak. Herein, we focus on a gradient plasticity model in which the yield function depends on second-order spatial derivatives of the hardening parameter, in particular on its Laplacian. As a result, the consistency condition becomes a partial differential equation [98].

In numerical implementations of this gradient-enhanced plasticity theory, the hardening parameter, which is an invariant measure of the plastic strain, is considered as a fundamental unknown and hence becomes an independent degree of freedom that is discretised in addition to the displacements. Different from standard plasticity models, both the equilibrium equation and the consistency condition are now cast in a weak format, and are solved simultaneously. The second-order derivatives of the hardening parameter which appear in the consistency parameter can, in principle, be reduced by an order through a standard application of Gauss' theorem. However, there is an issue at the internal boundary in the body between the elastic and the plastified parts, where a boundary condition on the hardening parameter has to be enforced. As in [35, 36] this internal boundary condition is not enforced explicitly, but is met by interpolating the hardening parameter by $\mathcal{C}^1$-continuous shape functions on the entire domain.

Interpolating the hardening parameter with $\mathcal{C}^1$-continuous shape functions is not straightforward using conventional finite elements. Only a limited class of elements exist which can satisfy a requirement of $\mathcal{C}^1$-continuity, e.g. Hermitian finite elements and mixed finite elements [36, 52, 92, 96]. Unfortunately, these formulations are often not so robust, and can be limited to uniform and regular meshes. However, the requirement of higher-order continuity poses no issues when considering discretisation methods that can exploit rational basis functions, such as meshless methods [105], or isogeometric analysis.

Isogeometric analysis [63] can be conceived as a finite element framework where B-splines (or NURBS) are being used as the basis functions rather than the traditional Langrange polynomials. B-splines, or nowadays rather their generalisation – Non-Uniform Rational B-Splines (NURBS) – have been widely used in Computer-Aided Geometric Design. Isogeometric analysis seeks to integrate the design and analysis processes by using the NURBS shape functions directly in analysis. For simple (one-patch) geometries, $\mathcal{C}^{p-1}$ continuity is achieved for NURBS of order p. The straightfor-

ward manner to achieve higher-order continuity with spline-based shape functions, has propelled their application in areas where higher-order continuity is necessary, such as gradient elasticity [50, 79, 86, 101, 123], gradient damage models [139], fluid flow in cracks of porous media [140], Kirchoff-Love shell theory [71, 89] and the Cahn-Hilliard equation [56, 69, 84].

Herein, we show how a plasticity theory with a gradient-dependent yield function is formulated and implemented exploiting isogeometric analysis. We employ Bézier extraction [24], which furnishes a convenient finite element data structure for analysis. The chapter is organised as follows. Section 3.2 presents the incremental formulation of the governing equations for gradient plasticity, their weak forms, and succinctly discusses issues like the stress update algorithm and consistent tangent operator. In section 3.3, the governing equations are discretised in an isogeometric analysis framework, including the formulation of Bézier elements for NURBS and the unequal order interpolation for displacements and the plastic multiplier. Representative numerical examples are given in one and two dimensions, and some concluding remarks are drawn.

3.2 Gradient-dependent plasticity

3.2.1 Incremental boundary value problem

Under static loading conditions and ignoring the effect of body forces, the equilibrium equation (in Voigt matrix notation) becomes:

$$\mathbf{L}^T \boldsymbol{\sigma} = \mathbf{0} \tag{3.1}$$

where $\boldsymbol{\sigma} = (\sigma_{xx}, \sigma_{yy}, \sigma_{zz}, \sigma_{xy}, \sigma_{yz}, \sigma_{zx})^T$ is the stress tensor in vector form, and $\mathbf{L}$ is the differential operator:

$$\mathbf{L} = \begin{bmatrix} \frac{\partial}{\partial x} & 0 & 0 & \frac{\partial}{\partial y} & \frac{\partial}{\partial z} & 0 \\ 0 & \frac{\partial}{\partial y} & 0 & \frac{\partial}{\partial x} & 0 & \frac{\partial}{\partial z} \\ 0 & 0 & \frac{\partial}{\partial z} & 0 & \frac{\partial}{\partial x} & \frac{\partial}{\partial y} \end{bmatrix}^T . \tag{3.2}$$

Under the assumption of small displacement gradients, the following kinematic relation holds:

$$\boldsymbol{\varepsilon} = \mathbf{L}\mathbf{u} \tag{3.3}$$

with the strain vector $\boldsymbol{\varepsilon} = (\varepsilon_{xx}, \varepsilon_{yy}, \varepsilon_{zz}, \tau_{xy}, \tau_{yz}, \tau_{zx})^T$ and the displacement vector $\mathbf{u} = (u_x, u_y, u_z)^T$. The incremental constitutive relation between the stress and strain increments is expressed as:

$$\mathrm{d}\boldsymbol{\sigma} = \mathbf{D}^e(\, \mathrm{d}\boldsymbol{\varepsilon} - \mathrm{d}\boldsymbol{\varepsilon}^p) \tag{3.4}$$

where $\mathbf{D}^e$ is the elastic stiffness matrix and $\mathrm{d}\boldsymbol{\varepsilon}^p$ is the plastic strain increment vector. We adopt an associated plasticity flow rule,

$$\mathrm{d}\boldsymbol{\varepsilon}^p = \mathrm{d}\lambda \mathbf{m}, \quad \mathbf{m} = \frac{\partial F}{\partial \boldsymbol{\sigma}} \tag{3.5}$$

in which $\mathrm{d}\lambda$ is a non-negative plastic multiplier and $\mathbf{m}$ is a vector that defines the direction of plastic flow relative to the yield function F.

In the form of gradient plasticity which we consider, the yield function is made dependent not only on the invariant plastic strain measure (effective plastic strain), κ, but also on its Laplacian, $\nabla^2\kappa$:

$$F = F(\boldsymbol{\sigma}, \kappa, \nabla^2\kappa) \tag{3.6}$$

For isotropic hardening or softening, the gradient dependent yield function reduces to:

$$F = \Phi(\boldsymbol{\sigma}) - \bar{\boldsymbol{\sigma}}(\kappa, \nabla^2\kappa) \tag{3.7}$$

To relate the hardening parameter, κ, to the plastic multiplier, λ, the strain-hardening hypothesis is adopted in the remainder:

$$\mathrm{d}\kappa = \sqrt{\frac{2}{3}(\mathrm{d}\boldsymbol{\varepsilon}^p)^T \mathbf{Q} \mathrm{d}\boldsymbol{\varepsilon}^p} \tag{3.8}$$

in which $\mathbf{Q} = \mathrm{diag}[1, 1, 1, \frac{1}{2}, \frac{1}{2}, \frac{1}{2}]$.

Equations (3.1), (3.3) and (3.4) are complemented by the Karush-Kuhn-Tucker loading-unloading conditions:

$$\mathrm{d}\lambda \geq 0, \quad F \leq 0, \quad F\mathrm{d}\lambda = 0 \tag{3.9}$$

Finally, standard static and kinematic boundary conditions must be specified on complementary parts of the body surface S:

$$\boldsymbol{\Upsilon}\mathbf{n}_s = \mathbf{t}, \quad \mathbf{u} = \mathbf{u}_s \tag{3.10}$$

where $\boldsymbol{\Upsilon}$ denotes the stress tensor in matrix form, $\mathbf{n}_s$ is the outward normal to the surface S, and $\mathbf{t}$ is the boundary traction vector.

3.2.2 Weak formulation

Due to the gradient dependence of the yield function, second-order spatial derivatives of the hardening parameter, κ, need to be computed. For this purpose, the yield function, will be satisfied in a weak sense, at the end of every loading step. Consequently, the plastic strain field has to be discretised in addition to the discretisation of the displacements. This leads to the following coupled equations at iteration $j+1$ of the current loading step:

$$\mathbf{L}^T \boldsymbol{\sigma}_{j+1} = \mathbf{0} \tag{3.11}$$

$$F(\boldsymbol{\sigma}_{j+1}, \kappa_{j+1}, \nabla^2 \kappa_{j+1}) = 0 \tag{3.12}$$

The weak form of these equations is obtained by setting:

$$\int_V \delta \mathbf{u}^T (\mathbf{L}^T \boldsymbol{\sigma}_{j+1}) \mathrm{d}V = \mathbf{0} \tag{3.13}$$

and

$$\int_V \delta\lambda F(\boldsymbol{\sigma}_{j+1}, \kappa_{j+1}, \nabla^2 \kappa_{j+1}) \mathrm{d}V = 0 \tag{3.14}$$

where δ denotes the variation of a quantity. When Equation (3.13) is integrated by parts and the divergence theorem is invoked, the following equation ensues:

$$\int_V \delta\boldsymbol{\varepsilon}^T \boldsymbol{\sigma}_{j+1} \mathrm{d}V - \int_S \delta \mathbf{u}^T \mathbf{t}_{j+1} \mathrm{d}S = \mathbf{0} \tag{3.15}$$

We next decompose the stress at iteration $j+1$ as sum of the stress at the previous iteration and an increment: $\boldsymbol{\sigma}_{j+1} = \boldsymbol{\sigma}_j + \mathrm{d}\boldsymbol{\sigma}$. With Equations (3.4) and $(3.5)_1$, we obtain:

$$\int_V \delta\boldsymbol{\varepsilon}^T \mathbf{D}^e (\, \mathrm{d}\boldsymbol{\varepsilon} - \mathrm{d}\lambda \mathbf{m}) dV = \int_S \delta \mathbf{u}^T \mathbf{t}_{j+1} \mathrm{d}S - \int_V \delta\boldsymbol{\varepsilon}^T \boldsymbol{\sigma}_j \mathrm{d}V \tag{3.16}$$

Through a Taylor's series expansion around $(\boldsymbol{\sigma}_j, \kappa_j, \nabla^2\kappa_j)$ and truncating after the linear terms, the yield function F can be developed as follows:

$$\begin{aligned} F(\boldsymbol{\sigma}_{j+1}, \kappa_{j+1}, \nabla^2\kappa_{j+1}) = F(\boldsymbol{\sigma}_j, \kappa_j, \nabla^2\kappa_j) + \left(\frac{\partial F}{\partial \boldsymbol{\sigma}}\right)^T \Bigg|_j \mathrm{d}\boldsymbol{\sigma} \\ + \frac{\partial F}{\partial \kappa}\Bigg|_j \mathrm{d}\kappa + \frac{\partial F}{\partial \nabla^2 \kappa}\Bigg|_j \nabla^2(\mathrm{d}\kappa) \end{aligned} \tag{3.17}$$

where $\mathrm{d}\kappa = \kappa_{j+1} - \kappa_j$. Next, we define the hardening modulus, H:

$$H(\kappa, \nabla^2\kappa) = -\frac{\mathrm{d}\kappa}{\mathrm{d}\lambda} \frac{\partial F}{\partial \kappa} \tag{3.18}$$

and the gradient influence variable g:

$$g(\kappa) = \frac{\mathrm{d}\kappa}{\mathrm{d}\lambda}\frac{\partial F}{\partial \nabla^2 \kappa} \tag{3.19}$$

and substitute them along with Equation $(3.5)_2$ into Equation (3.17) to obtain:

$$F(\boldsymbol{\sigma}_{j+1}, \kappa_{j+1}, \nabla^2\kappa_{j+1}) = F(\boldsymbol{\sigma}_j, \kappa_j, \nabla^2\kappa_j) + \mathbf{m}^T \mathrm{d}\boldsymbol{\sigma} - H\mathrm{d}\lambda + g\nabla^2(\mathrm{d}\lambda) \tag{3.20}$$

Using Equations (3.4), (3.5) and (3.20), Equation (3.14) is now expressed as:

$$\begin{aligned}\int_{V_\lambda} \delta\lambda\big[\mathbf{m}^T\mathbf{D}^e\mathrm{d}\boldsymbol{\varepsilon} - (H + \mathbf{m}^T\mathbf{D}^e\mathbf{m})\mathrm{d}\lambda + g\nabla^2(\mathrm{d}\lambda)\big]dV = \\ - \int_{V_\lambda} \delta\lambda F(\boldsymbol{\sigma}_j, \kappa_j, \nabla^2\kappa_j)\mathrm{d}V\end{aligned} \tag{3.21}$$

where V_λ is the volume of the plastic region of the body. The values of $\mathbf{m}$, H and g are determined for the state defined by $(\boldsymbol{\sigma}_j, \kappa_j, \nabla^2\kappa_j)$. Integrating the Laplacian term in Equation (3.21) by parts, we obtain:

$$\begin{aligned}\int_{V_\lambda} \delta\lambda\big[\mathbf{m}^T\mathbf{D}^e\mathrm{d}\boldsymbol{\varepsilon} - (H + \mathbf{m}^T\mathbf{D}^e\mathbf{m})\mathrm{d}\lambda\big]dV - \int_{V_\lambda} g(\nabla\delta\lambda)^T(\nabla\mathrm{d}\lambda)\mathrm{d}V = \\ - \int_{V_\lambda} \delta\lambda F(\boldsymbol{\sigma}_j, \kappa_j, \nabla^2\kappa_j)\mathrm{d}V\end{aligned} \tag{3.22}$$

and the following (non-standard) boundary conditions need to be fulfilled on S_λ, the boundary of the plastified part of the domain:

$$\delta\lambda = 0 \quad \text{or} \quad (\nabla\mathrm{d}\lambda)^T\mathbf{n}_\lambda = 0 \tag{3.23}$$

in which $\mathbf{n}_\lambda$ is the outward normal to the plastic region of the surface.

For finite increments, the elastic-plastic boundary moves stepwise as the plastic zone evolves. When this occurs, the first boundary condition Equation $(3.23)_1$ may not be satisfied and Equation $(3.23)_2$ must hold. This can be achieved either by enforcing Equation $(3.23)_2$ explicitly at S_λ, or by using $\mathcal{C}^1$-continuous basis functions for λ, so that the fact that $\lambda = 0$ on the entire elastic part of the domain directly leads to Equation $(3.23)_2$ to be satisfied at S_λ. It is noted that, different from Hermitian or mixed finite elements, where the derivatives of λ are required as independent degrees of freedom, the isogeometric formulation only requires the interpolation of λ, and no additional boundary conditions are necessary other than Equations (3.23).

3.2.3 Stress-strain relation and algorithmic tangent operator

The stress update in gradient plasticity follows the procedure from standard elasto-plasticity. It is computed as an integral along a given path from the initial state $(\boldsymbol{\sigma}_0, \boldsymbol{\varepsilon}_0)$ to the final state $(\boldsymbol{\sigma}_j, \boldsymbol{\varepsilon}_j)$:

$$\boldsymbol{\sigma} = \boldsymbol{\sigma}_0 + \int_{\boldsymbol{\varepsilon}_0}^{\boldsymbol{\varepsilon}_j} \mathbf{D}^e \mathrm{d}\boldsymbol{\varepsilon} \tag{3.24}$$

The algorithmic stress update in iteration j follows the format [36]:

$$\boldsymbol{\sigma}_j = \boldsymbol{\sigma}_0 + \mathbf{S}(\boldsymbol{\varepsilon}_0, \boldsymbol{\Delta\varepsilon}_j) \tag{3.25}$$

where $\mathbf{S}$ is a non-linear mapping operator and $\boldsymbol{\Delta}$ is a total increment, i.e. sum of increments in all iterations for the current load step:

$$\boldsymbol{\Delta\varepsilon}_j = \sum_{i=1}^{j} \mathrm{d}\boldsymbol{\varepsilon}_i \tag{3.26}$$

The stress update in gradient plasticity uses an Euler backward algorithm [36]:

$$\boldsymbol{\sigma}_j = \boldsymbol{\sigma}_0 + \mathbf{D}^e \boldsymbol{\Delta\varepsilon}_j - \Delta\lambda_j \mathbf{D}^e \mathbf{m}_j. \tag{3.27}$$

The algorithmic or consistent tangent operator is defined as [36]:

$$\mathbf{D}^{alg} = \left.\frac{\partial \boldsymbol{\sigma}_j}{\partial \boldsymbol{\Delta\varepsilon}}\right|_{\boldsymbol{\varepsilon}_0, \boldsymbol{\Delta\varepsilon}_j} = \left.\frac{\partial \mathbf{S}}{\partial \boldsymbol{\Delta\varepsilon}}\right|_{\boldsymbol{\varepsilon}_0, \boldsymbol{\Delta\varepsilon}_j} \tag{3.28}$$

and is generally non-symmetric [103]. The full algorithm is summarised in Box 3.1.

1. Compute the matrices $\mathbf{K}_{aa}$, $\mathbf{K}_{a\lambda}$, $\mathbf{K}_{\lambda a}$ and $\mathbf{K}_{\lambda\lambda}$, and forces f_e, f_a and f_λ, according to Equations (3.49) – (3.54) while replacing $\mathbf{D}^e$ with $\mathbf{D}^{alg}$

2. Solve for $\mathrm{d}\mathbf{a}$ and $\mathrm{d}\boldsymbol{\Lambda}$ using Equation (3.48)

3. Update the total increments $\Delta\mathbf{a}_{j+1} = \Delta\mathbf{a}_j + \mathrm{d}\mathbf{a}$, and $\Delta\boldsymbol{\Lambda}_{j+1} = \Delta\boldsymbol{\Lambda}_j + \mathrm{d}\boldsymbol{\Lambda}$.

4. Compute the following at each integration point:

   $\Delta\boldsymbol{\varepsilon}_{j+1} = \mathbf{B}\Delta\mathbf{a}_{j+1}$,

   $\Delta\lambda_{j+1} = \mathbf{h}^T\Delta\boldsymbol{\Lambda}_{j+1}$,

   $\nabla^2(\Delta\lambda_{j+1}) = \mathbf{p}^T\Delta\boldsymbol{\Lambda}_{j+1}$,

   $\kappa_{j+1} = \kappa_0 + \eta\Delta\lambda_{j+1}$,

   $\nabla^2\kappa_{j+1} = \nabla^2\kappa_0 + \eta\nabla^2(\Delta\lambda_{j+1})$,

   trial stress $\boldsymbol{\sigma}_t = \boldsymbol{\sigma}_0 + \mathbf{D}^e\Delta\boldsymbol{\varepsilon}_{j+1}$.

   If $F(\boldsymbol{\sigma}_{j+1}, \kappa_{j+1}, \nabla^2\kappa_{j+1}) > 1 \times 10^{-6}$,

   then plastic state:

   compute $\mathbf{m}_t$ using the trial stress update: $\boldsymbol{\sigma}_{j+1} = \boldsymbol{\sigma}_t - \Delta\lambda_{j+1}\mathbf{D}^e\mathbf{m}_t$

   compute the algorithmic stiffness operator

   compute H for the next iteration,

   else

   elastic state:

   $\mathbf{m}_t = \mathbf{0}$

   $\boldsymbol{\sigma}_{j+1} = \boldsymbol{\sigma}_t$

   $\mathbf{D}^{alg} = \mathbf{D}^e$

   $H = E$

5. Check the global convergence criterion. If not converged, go to 1.

$(\bullet)_0$ denotes value at previous converged load step and $(\bullet)_j$ indicates value at previous iteration.

Box 3.1. Algorithm: $\mathcal{C}^1$ formulation for explicit gradient plasticity (iteration $j+1$)

3.3 Isogeometric discretisation: $\mathcal{C}^1$-continuous formulation

Herein, we use NURBS as shape functions and through Bézier extraction, cast them in an element data structure as in standard finite element analysis.

3.3.1 NURBS shape functions

The basis functions of a univariate NURBS are given by:

$$R_{a,p}(\xi) = \frac{w_a B_{a,p}(\xi)}{\mathbf{W}(\xi)} \tag{3.29}$$

where $B_{a,p}$ is the basis function of the underlying B-spline, w_a is the corresponding NURBS weight and $\mathbf{W}$ is the weight function:

$$\mathbf{W}(\xi) = \sum_{b=1}^{n} w_b B_{b,p}(\xi) \tag{3.30}$$

The B-spline basis is defined for a polynomial of degree $p = 0$, as:

$$B_{a,0}(\xi) = \begin{cases} 1, & \xi_a \leq \xi \leq \xi_{a+1} \\ 0, & \text{otherwise} \end{cases} \tag{3.31}$$

and by the Cox-de Boor recursion formula for $p > 0$:

$$B_{a,p}(\xi) = \frac{\xi - \xi_a}{\xi_{a+p} - \xi_a} B_{a,p-1}(\xi) + \frac{\xi_{a+p+1} - \xi}{\xi_{a+p+1} - \xi_{a+1}} B_{a+1,p-1}(\xi) \tag{3.32}$$

where ξ is the parametric coordinate (knot) of a knot vector with increasing knot values:

$$\boldsymbol{\Xi} = \{\xi_1, \xi_2, \ldots, \xi_{n+p+1}\} \tag{3.33}$$

in which p is the polynomial degree and n is the number of basis functions. Projective transformations of B-splines in $\mathbb{R}^{d+1}$ produce NURBS in $\mathbb{R}^d$. Through a tensor product of the univariate NURBS bases, we obtain the two-dimensional NURBS shape functions:

$$N_{a,b}^{p,q}(\xi, \eta) = \frac{B_{a,p}(\xi) A_{b,q}(\eta) w_{a,b}}{\sum_{c=1}^{nB} \sum_{d=1}^{nA} B_{c,p}(\xi) A_{d,q}(\eta) w_{c,d}} \tag{3.34}$$

where η, $A_{b,q}$, q and nA are the knot vector, the B-spline basis, the polynomial degree and the number of basis functions in the second spatial dimension respectively.

NURBS shape functions of order p are $\mathcal{C}^{p-1}$-continuous provided there are no repeated knots [63].

3.3.2 Bézier element

Different from Lagrange polynomials, NURBS basis functions are not local to an element. To facilitate isogeometric analysis in a classical finite element structure, the concept of Bézier extraction has been proposed [24]. In this approach, a NURBS mesh can be decomposed into $\mathcal{C}^0$-continuous Bézier elements through a Bézier extraction operator $\mathbf{C}$. While this gives a convenient element structure, it does not restrict the continuity of NURBS. For a two-dimensional element e, the NURBS shape functions become:

$$\mathbf{N}^e(\xi,\eta) = \mathbf{W}^e\mathbf{C}^e\frac{\mathbf{B}^e(\xi,\eta)}{W^e(\xi,\eta)} \tag{3.35}$$

with

$$W^e(\xi,\eta) = (\mathbf{w}^e)^T\mathbf{C}^e\mathbf{B}^e(\xi,\eta) \tag{3.36}$$

where $\mathbf{N}$ contains the NURBS basis functions, $\mathbf{w}$ is a vector of the NURBS weights, and $\mathbf{B}$ contains the Bézier basis functions (Bernstein polynomials). The procedure for computing the Bézier extraction operator of a NURBS has been presented in [24].

3.3.3 Orders of interpolation

The displacement field, $\mathbf{u}$, and the plastic multiplier, λ, are discretised as follows:

$$\mathbf{u} = \mathbf{N}\mathbf{a} \tag{3.37}$$

$$\lambda = \mathbf{h}^T\boldsymbol{\Lambda} \tag{3.38}$$

where $\mathbf{a}$ is a vector of discrete displacements at the control points, $\boldsymbol{\Lambda}$ is a vector of the plastic multiplier degrees of freedom at the control point, $\mathbf{N}$ is a matrix, and $\mathbf{h}$, a vector, both containing NURBS shape functions. According to the linear kinematic relation in Equation (3.3), the strain vector can be expressed as:

$$\boldsymbol{\varepsilon} = \mathbf{B}\mathbf{a} \tag{3.39}$$

where $\mathbf{B} = \mathbf{LN}$. In a similar way, we discretise the gradient of the plastic multiplier $\nabla\lambda$ and its Laplacian as:

$$\nabla\lambda = \mathbf{q}^T\mathbf{\Lambda} \tag{3.40}$$

$$\nabla^2\lambda = \mathbf{p}^T\mathbf{\Lambda} \tag{3.41}$$

where

$$\mathbf{q} = [\nabla h_1, \nabla h_2, \ldots, \nabla h_{ns}]^T \tag{3.42}$$

$$\mathbf{p} = [\nabla^2 h_1, \nabla^2 h_2, \ldots, \nabla^2 h_{ns}]^T \tag{3.43}$$

and ns is the number of shape functions at each control point.

The strain vector is one order lower than the displacement, cf. Equation (3.3). Since the plastic multiplier is of the same order as the (plastic) strain, the interpolation functions of the displacements, contained in $\mathbf{N}$, should be taken to be one order higher than those used for the plastic multiplier ($\mathbf{h}$). To satisfy the $\mathcal{C}^1$-continuity requirement, the NURBS shape functions in $\mathbf{h}$, must be, at least, of order two. Therefore, the shape functions in $\mathbf{N}$ are taken to be of the order three.

In isogeometric analysis, Bézier projection is generally required to construct conforming meshes of different orders and matching element boundaries. The procedure for achieving this has been presented in [140]. Starting with p-refinement, which elevates a NURBS from order p to order p', the control points for the p' curve/surface are computed for each element e as follows:

$$\mathbf{P}^{e,p'} = (\mathbf{R}^{e,p'})^T(\mathbf{E}^{p,p'})^T(\mathbf{C}^{e,p})^T(\mathbf{P}^{e,p}) \tag{3.44}$$

where $\mathbf{P}^{e,p}$ contains the control points of the initial curve/surface of order p, $\mathbf{P}^{e,p'}$ contains the control points of the target curve/surface of order p', $\mathbf{C}^{e,p}$ contains the initial Bézier extraction operator, $\mathbf{R}^{e,p'}$ is the inverse of the target Bézier extraction operator, i.e. $\mathbf{R}^{e,p'} = (\mathbf{C}^{e,p'})^{-1}$, and $\mathbf{E}^{p,p'}$ is the elevation matrix from degree p to p'. For a univariate elevation from quadratic to cubic NURBS, the elevation matrix is given by [140]:

$$\mathbf{E}^{2,3}_{uni} = \begin{bmatrix} 1 & \frac{1}{3} & 0 & 0 \\ 0 & \frac{2}{3} & \frac{2}{3} & 0 \\ 0 & 0 & \frac{1}{3} & 1 \end{bmatrix}. \tag{3.45}$$

The corresponding bivariate elevation matrix is obtained as a tensor product of the univariate matrices [24, 140]:

$$\mathbf{E}_{bi}^{2,3} = \mathbf{E}_{uni}^{2,3} \otimes \mathbf{E}_{uni}^{2,3} \tag{3.46}$$

When considering a one-dimensional 100 mm bar with one element, the initial quadratic knot vector is $\mathbf{\Xi}_2 = \{0,0,0,1,1,1\}$ with control points $\mathbf{P}^{1,2} = [0 \quad 0;\ 50 \quad 0;\ 100 \quad 0]$ and the target cubic knot vector is $\mathbf{\Xi}_3 = \{0,0,0,0,1,1,1,1\}$. Equation (3.44) then specialises as:

$$\left(\begin{bmatrix} 1 & 0 & 0 & 0 \\ 0 & 1 & 0 & 0 \\ 0 & 0 & 1 & 0 \\ 0 & 0 & 0 & 1 \end{bmatrix}^{-1} \right)^T \begin{bmatrix} 1 & \frac{1}{3} & 0 & 0 \\ 0 & \frac{2}{3} & \frac{2}{3} & 0 \\ 0 & 0 & \frac{1}{3} & 1 \end{bmatrix}^T \begin{bmatrix} 1 & 0 & 0 \\ 0 & 1 & 0 \\ 0 & 0 & 1 \end{bmatrix}^T \begin{bmatrix} 0 & 0 \\ 50 & 0 \\ 100 & 0 \end{bmatrix} = \begin{bmatrix} 0 & 0 \\ 33.3333 & 0 \\ 66.6667 & 0 \\ 100.000 & 0 \end{bmatrix} \tag{3.47}$$

3.3.4 Spatial discretisation

The weak forms, Equations (3.16) and (3.21), are discretised using the interpolations of Equations (3.37) – (3.41). Requiring that the result holds for all admissible $\delta\mathbf{a}$ and $\delta\mathbf{\Lambda}$, we obtain the following set of non-linear algebraic equations [36]:

$$\begin{bmatrix} \mathbf{K}_{aa} & \mathbf{K}_{a\lambda} \\ \mathbf{K}_{\lambda a} & \mathbf{K}_{\lambda\lambda} \end{bmatrix} \begin{bmatrix} \mathrm{d}\mathbf{a} \\ \mathrm{d}\mathbf{\Lambda} \end{bmatrix} = \begin{bmatrix} \mathbf{f}_e + \mathbf{f}_a \\ \mathbf{f}_\lambda \end{bmatrix} \tag{3.48}$$

with the elastic stiffness matrix

$$\mathbf{K}_{aa} = \int_V \mathbf{B}^T \mathbf{D}^e \mathbf{B} \mathrm{d}V, \tag{3.49}$$

the off-diagonal matrices

$$\mathbf{K}_{a\lambda} = -\int_V \mathbf{B}^T \mathbf{D}^e \mathbf{m} \mathbf{h}^T \mathrm{d}V, \quad \mathbf{K}_{\lambda a} = \mathbf{K}_{a\lambda}^T, \tag{3.50}$$

the non-symmetric gradient-dependent matrix

$$\mathbf{K}_{\lambda\lambda} = \int_V [(H + \mathbf{m}^T \mathbf{D}^e \mathbf{m}) \mathbf{h}\mathbf{h}^T - g \mathbf{h}\mathbf{p}^T] \mathrm{d}V, \tag{3.51}$$

the external force vector

$$\mathbf{f}_e = \int_S \mathbf{N}^T \mathbf{t}_{j+1} \mathrm{d}S, \tag{3.52}$$

the vector of control point forces (equivalent to internal stresses)

$$\mathbf{f}_a = -\int_V \mathbf{B}^T \boldsymbol{\sigma}_j \mathrm{d}V, \tag{3.53}$$

and the vector of residual forces due to inexact fulfilment of the yield function

$$\mathbf{f}_\lambda = \int_V F(\boldsymbol{\sigma}_j, \lambda_j, \nabla^2 \lambda_j)\mathbf{h}\, \mathrm{d}V. \tag{3.54}$$

For associated flow, the gradient-dependent matrix can be made symmetric when Equation (3.22) is discretised instead of Equation (3.21):

$$\mathbf{K}_{\lambda\lambda} = \int_V [(H + \mathbf{m}^T \mathbf{D}^e \mathbf{m})\mathbf{h}\mathbf{h}^T + g\mathbf{q}\mathbf{q}^T]\mathrm{d}V \tag{3.55}$$

It has been proposed to initially set the hardening modulus H equal to the Young's modulus E for elastic elements [36] in order to avoid singularity of the tangent operator for these elements. Also, when all elements are elastic, the gradient vector $\mathbf{m}$ is set to zero, and subsequently, $\mathbf{K}_{a\lambda} = \mathbf{K}_{a\lambda}^T = \mathbf{0}$.

3.4 Numerical examples

We demonstrate the suitability of isogeometric finite element analysis for gradient plasticity. In all examples considered, NURBS shape functions of order $p = 3$ have been used to discretise the displacements and for the plastic multiplier NURBS basis functions of order $p = 2$ have been employed. The non-symmetric formulation has been used.

3.4.1 Gradient-dependent yield function

The Maxwell-Huber-Hencky-von Mises yield criterion is adopted for all numerical simulations:

$$F = \sqrt{\left(\frac{3}{2}\boldsymbol{\sigma}^T \mathbf{P} \boldsymbol{\sigma}\right)} - \bar{\boldsymbol{\sigma}}(\kappa, \nabla^2 \kappa) \tag{3.56}$$

where $\bar{\boldsymbol{\sigma}}_g$ is the gradient dependent yield strength and $\mathbf{P}$ is the symmetric projection matrix:

$$\mathbf{P} = \begin{bmatrix} \frac{2}{3} & -\frac{1}{3} & -\frac{1}{3} & 0 & 0 & 0 \\ -\frac{1}{3} & \frac{2}{3} & -\frac{1}{3} & 0 & 0 & 0 \\ -\frac{1}{3} & -\frac{1}{3} & \frac{2}{3} & 0 & 0 & 0 \\ 0 & 0 & 0 & 2 & 0 & 0 \\ 0 & 0 & 0 & 0 & 2 & 0 \\ 0 & 0 & 0 & 0 & 0 & 2 \end{bmatrix}. \tag{3.57}$$

The simple case of linear softening and a constant gradient influence variable (g) is considered. This renders the following form for the gradient-dependent yield strength:

$$\bar{\boldsymbol{\sigma}}(\kappa, \nabla^2\kappa) = \sigma_y + H\kappa - g\nabla^2\kappa, \quad g = -\ell^2 H \tag{3.58}$$

where σ_y is the initial yield strength and ℓ is an internal length scale.

3.4.2 One-dimensional tensile bar with and without imperfection

A one-dimensional bar with specifications as listed in Table 3.1 and shown in Figure 3.1 is investigated using classical plasticity ($g = 0$) and gradient plasticity ($g = 50000$ N), cf. [36]. First, an ideally plastic homogeneous bar is considered, and then, in order to trigger localisation, a small imperfection is introduced in the central part of the bar. The stress and displacement at the right end are σ_r and $\bar{u}$ respectively. We consider two refined meshes with 2^6 and 2^7 elements respectively. For each mesh, four Gauss integration points are employed.

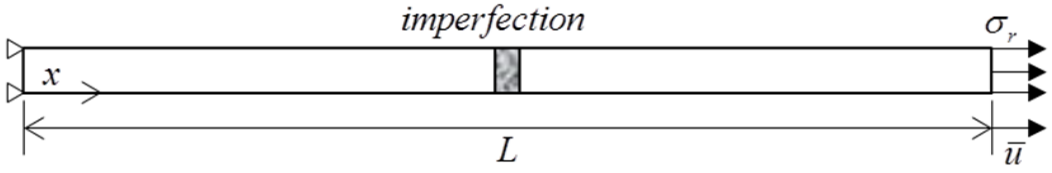

Figure 3.1: Tensile bar with imperfection

Figure 3.2 shows the load-displacement diagram for a homogeneous bar assuming ideal plasticity ($H = 0$). A mesh of 64 elements is used. It is noted that g is zero since

Specification	**Notation**	**Value**
Length	L	100 mm
Young's modulus	E	20000 N/mm^2
Tensile strength	σ_y	2 N/mm^2
Reduced tensile strength	σ_{yr}	1.8 N/mm^2
Softening modulus	H	-2000 N/mm^2
Gradient constant	g	50000 N
Thickness	t	1 mm

Table 3.1: Specifications for one-dimensional tensile bar

H is zero. A nonzero H as well as an imperfection are needed to trigger localisation. The latter is implemented by introducing an imperfect zone at the middle of the bar with H and g as given in Table 3.1. This is done by reducing the yield strength in the affected zone by 10%. The imperfection zone length is not very crucial [105], thus we use a length of 3.125 mm (two mid-elements).

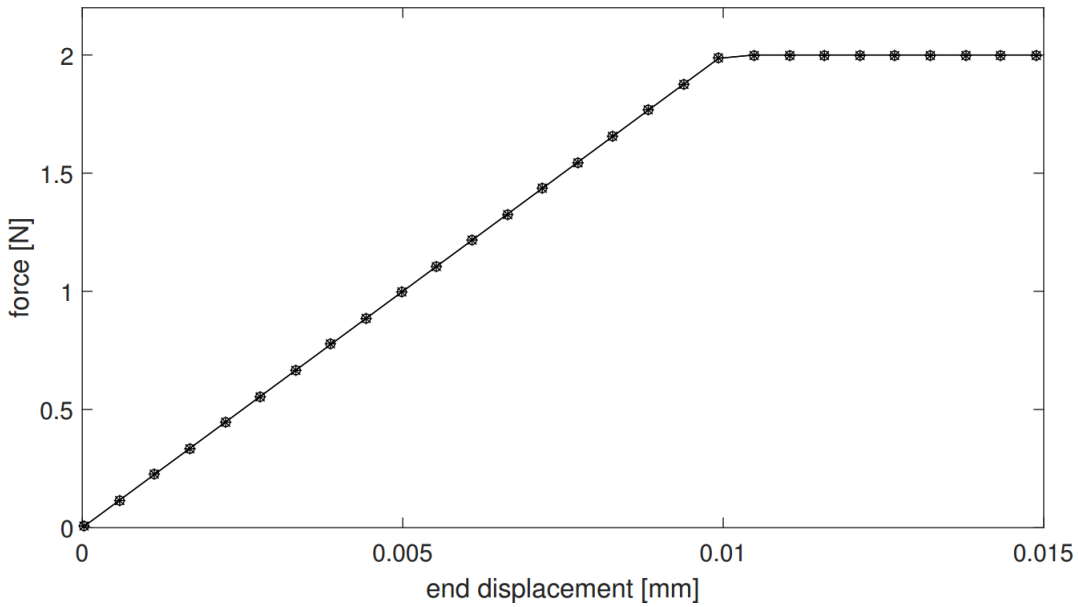

Figure 3.2: Perfectly plastic homogeneous bar without imperfection.

Results for the imperfect bar are shown in Figures 3.3 and 3.4. It is evident from

the load-displacement diagram that there is no mesh dependence. In fact, the slope of the softening regime matches the analytical solution perfectly, cf. [35]. The cosine distribution of the effective plastic strain that comes from the analytical solution is also reproduced. A localisation zone width of $10\pi \approx 31.4$ mm was calculated analytically. This matches very closely with the localisation zone widths for both discretisations, see Figure 3.4. It is noted that for $\ell = 5$ mm, the load-displacement curve shows a sharp cusp beyond an end displacement of 0.02 mm [35]. This leads to non-symmetric evolution of the plastic strain distribution. Thus, to conveniently compare the results with the analytical solution, the maximum end displacement has been chosen before the cusp develops.

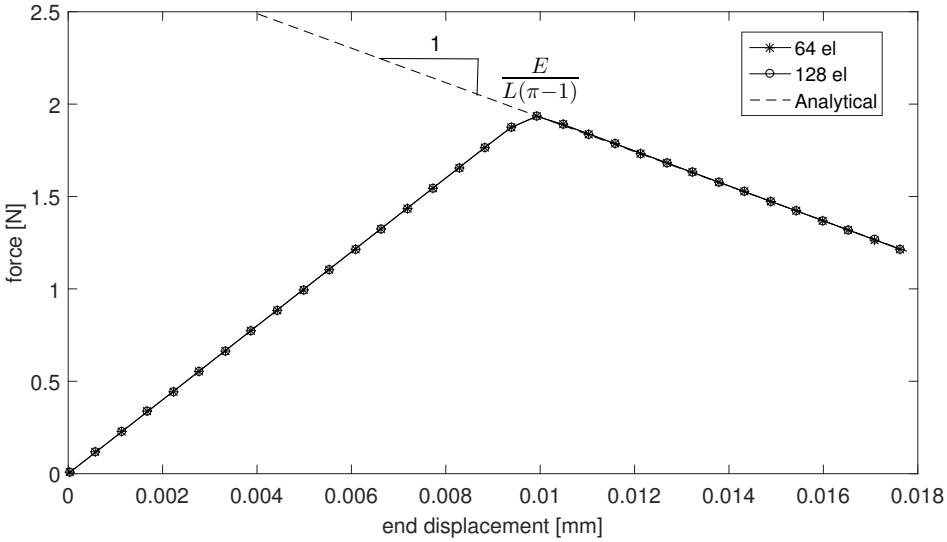

Figure 3.3: Imperfect bar: Load-displacement diagrams for discretisations with 64 and 128 elements (el).

Figure 3.5 exhibits stress oscillations which do not disappear even upon mesh refinement. This was also observed using the element-free Galerkin method [105] and is due to the satisfaction of the yield function only in a weak sense rather than in a point-wise fashion. This manifests in the additional partial differential equation that arises from a Taylor expansion of the yield function which makes the plastic multiplier an independent discretised variable. The norm of non-standard residuals does not fully converge to zero, and neither does the norm of out-of-balance forces.

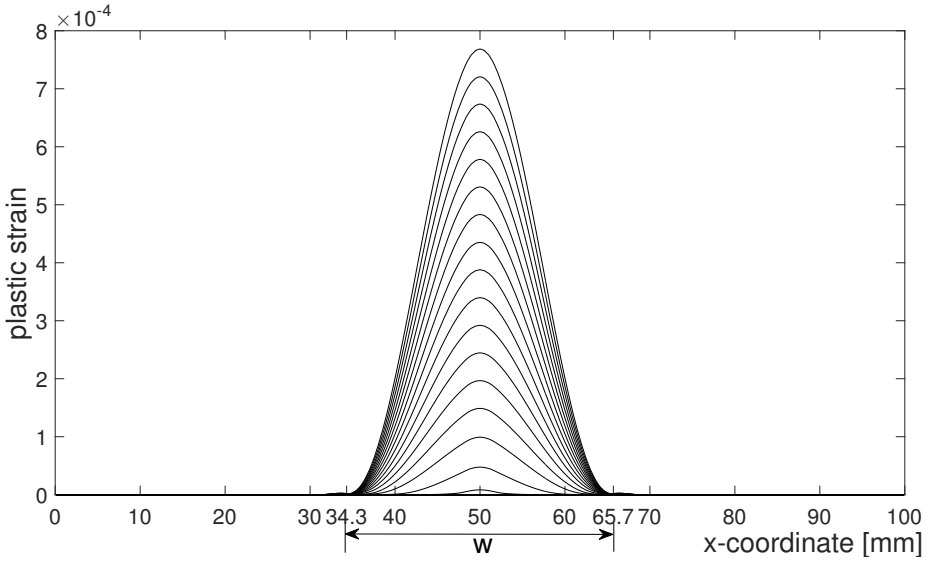

(a)

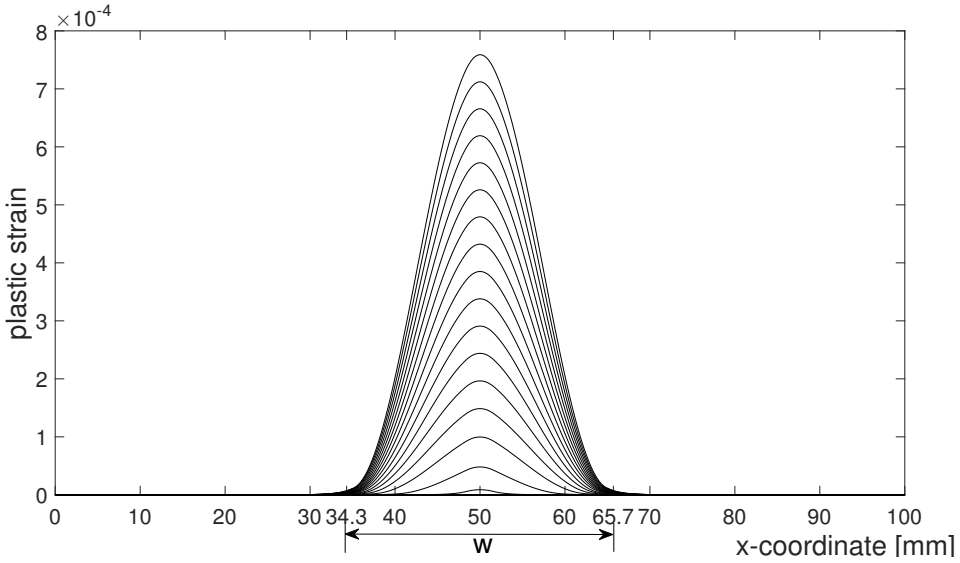

(b)

Figure 3.4: Evolution of effective plastic strain for the bar with imperfection discretised with (a) 64 elements and (b) 128 elements. w is the analytical solution: $10\pi \approx 31.4$ mm.

3.4.3 Two-dimensional panel under uniaxial tension

Next, we consider a square panel subjected to uniaxial tension as shown in Figure 3.6 with material properties summarised in Table 3.2, cf. [83, 145]. The left edge is restricted in the x-direction with its midpoint fixed in both directions, while the right

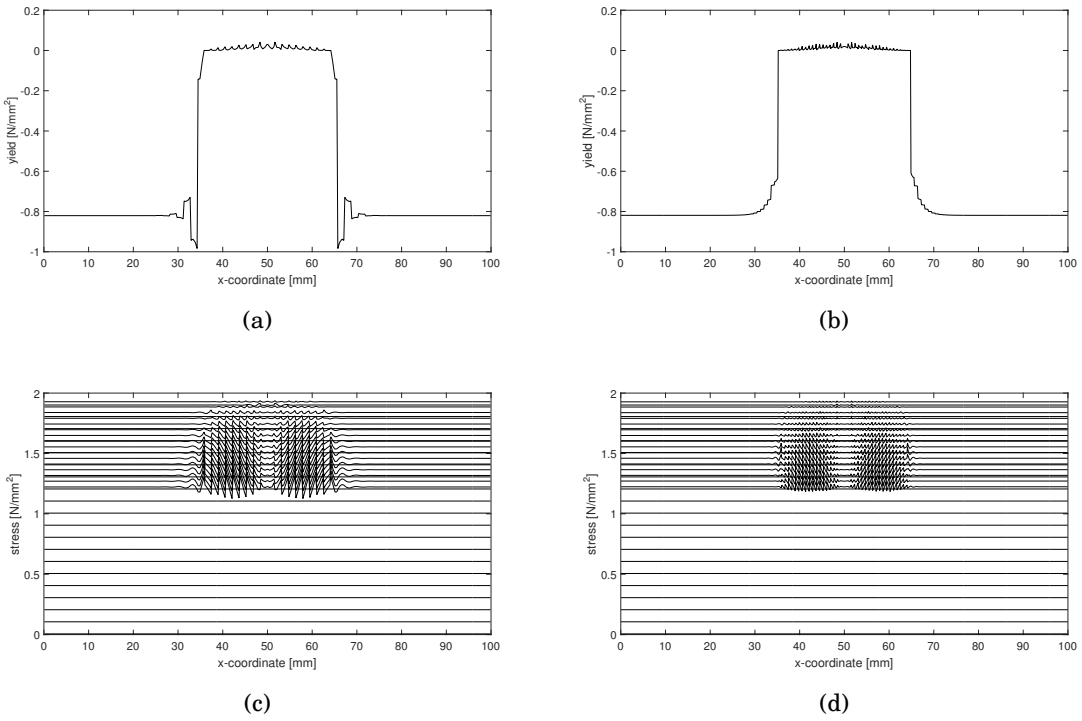

Figure 3.5: Non-zero values of the yield function in the final step – (a),(b), and evolution of stress oscillations – (c),(d) for the imperfect bar discretised with 64 elements (left) and 128 elements (right).

edge is pulled in the x-direction. In order to avoid a homogeneous deformation with no gradient effect, some elements at the bottom-left corner have been weakened. We consider two meshes with $2^4 \times 2^4$ and $2^5 \times 2^5$ elements, respectively.

The two meshes and the corresponding weak elements with a 10% reduction in yield strength are shown in Figure 3.7. Starting from the region of weak-strong elements interface, a localisation band develops. This is depicted in Figure 3.8. For classical plasticity (Figure 3.8(a) and (b)), the localisation width is strongly mesh dependent. This also becomes clear from the load-displacement diagram of Figure 3.9(a), where the curve using 256 elements deviates from the discretisation with 1024 elements. It is noted that the difference is moderate due to the fact that in this example only a very moderate rate of softening has been used ($H/E = -0.02$). A rather moderate rate of softening was chosen because otherwise convergence problems were encountered for this 2–dimensional problem.

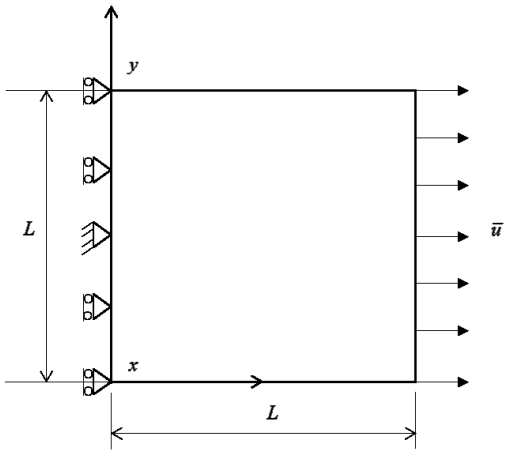

Figure 3.6: Geometry and boundary conditions of square panel under uniaxial tension.

Specification	**Notation**	**Value**
Length	L	10 mm
Young's modulus	E	20000 N/mm^2
Poisson ratio	ν	0.25
Tensile strength	σ_y	2 N/mm^2
Reduced tensile strength	σ_{yr}	1.8 N/mm^2
Softening modulus	H	-400 N/mm^2
Gradient constant	g	100 N ($\ell = 0.5$ mm)
		400 N ($\ell = 1.0$ mm)

Table 3.2: Specifications for square panel under tension.

When an internal length scale is introduced, unsurprisingly, results are obtained that are fully mesh-objective. This is very clear from the contour plots for the effective plastic strain, Figures 3.8(c)-(d) for an internal length scale $\ell = 0.5$ mm, and Figures 3.8(e)-(f) for an internal length scale $\ell = 1.0$ mm. It is noted that for convenience, the scales of plots comparing classical and gradient plasticity have been synchronised. Comparing the contour plots for $\ell = 0.5$ mm on one hand, and those for $\ell = 1.0$ mm, on the other hand, we clearly observe that the width of the localisation zone is proportional to the internal length scale. Figures 3.9 also show full mesh-objectivity when a

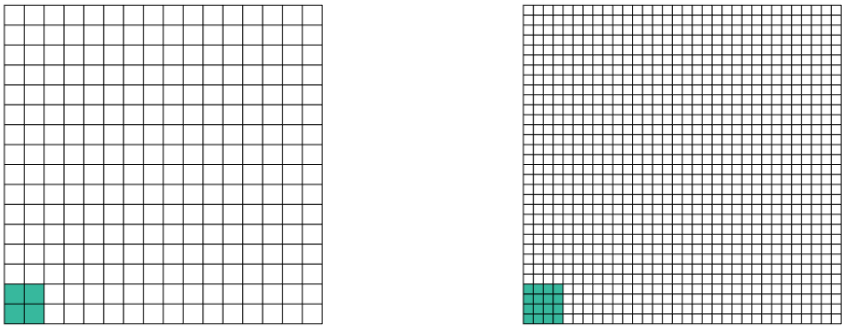

(a) (b)

Figure 3.7: Meshes of square panel showing weakened elements: (a) 256 elements; (b) 1024 elements.

gradient dependence is introduced in the yield function, and confirm that for higher values of ℓ a more ductile behaviour is obtained, which is concomitant with an increased width of the localisation zone. The localisation pattern is a point of further study. The orientation of the shearband is affected by the assumptions related to the constitutive model, the Poisson's ratio and plane stress or plane strain configuration [130]. Different shearband orientations have been shown for plane stress and plane strain configurations of a biaxial compression test [132]. One method that can be looked into is the B-bar method related to volumetric locking as suggested by [23]. On another note, when the elements along the diagonal are weakened, this maintains the band along the diagonal of the specimen [83].

The finite element size needs to be smaller than the internal length scale for sufficient accuracy to be achieved [62]. The mesh size needs to be at least three times smaller than $2\pi\ell$ [35]. For a length scale of 0.5 mm for example, the mesh size needs to be 1.05 mm or lower; we have 0.625mm (16 $\times$ 16 elements) which is sufficient. For a coarser mesh (8 $\times$ 8 elements with a finite element size of 1.25 mm), the load-displacement curve failed to converge for $\ell = 0.5$ mm. In transient finite element analysis which tries to accurately capture the propagation of plastic strain, the observation implies that the size of the finite elements should be small relative to the size of the structure. Adaptive remeshing may therefore be required particularly in the localisa-

tion area [39, 62].

As emphasised in [43], contour plots are important in assessing higher-order NURBS elements in plasticity as load-displacement diagrams may not be sufficient. The least squares approach [43, 95] has been used for plotting the effective plastic strain contours employing the relevant (quadratic) shape functions. A brief description of how to extrapolate the effective plastic strain values from Gauss points to control points is explained next.

History variables are normally computed at integration points. However, these variables must be extrapolated to the control points for post-processing purposes. Herein, we have adopted a global least-squares fit to extrapolate the effective plastic strain from the Gauss points to the control points. The control variables contained in the vector $\boldsymbol{\kappa}^c$ are obtained from the Gauss point values contained in the vector $\boldsymbol{\kappa}^g$ by solving [95]:

$$\mathbf{M}\boldsymbol{\kappa}^c = \int_V \mathbf{h}^T \boldsymbol{\kappa}^g \mathrm{d}V \tag{3.59}$$

where M is the least-squares fit matrix or Gramm matrix given by:

$$\mathbf{M} = \int_V \mathbf{h}\mathbf{h}^T \mathrm{d}V \tag{3.60}$$

and h a vector that contains the NURBS shape functions used for discretising the plastic multiplier as in Equation (3.38). The same approach can be used for other history variables.

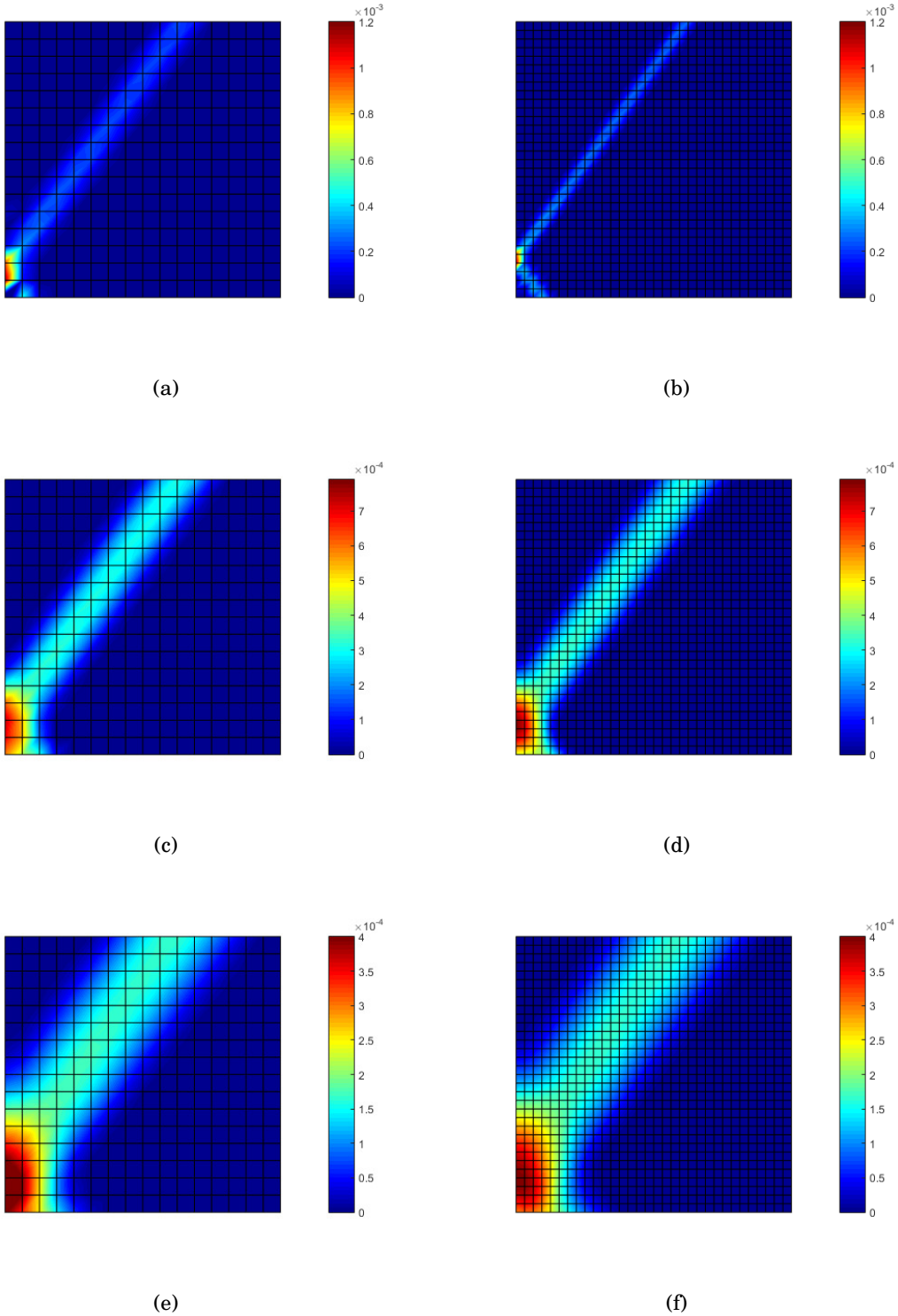

Figure 3.8: Square panel: Distribution of effective plastic strain measure (κ) for the case of classical plasticity – (a) and (b), and gradient plasticity for $\ell = 0.5$ mm – (c) and (d), as well as $\ell = 1.0$ mm – (e) and (f).

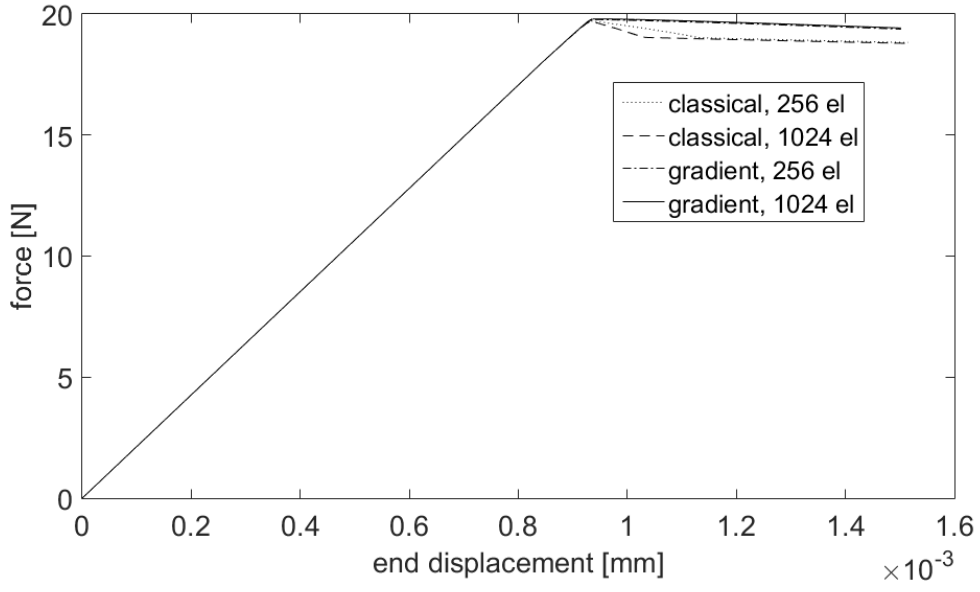

(a)

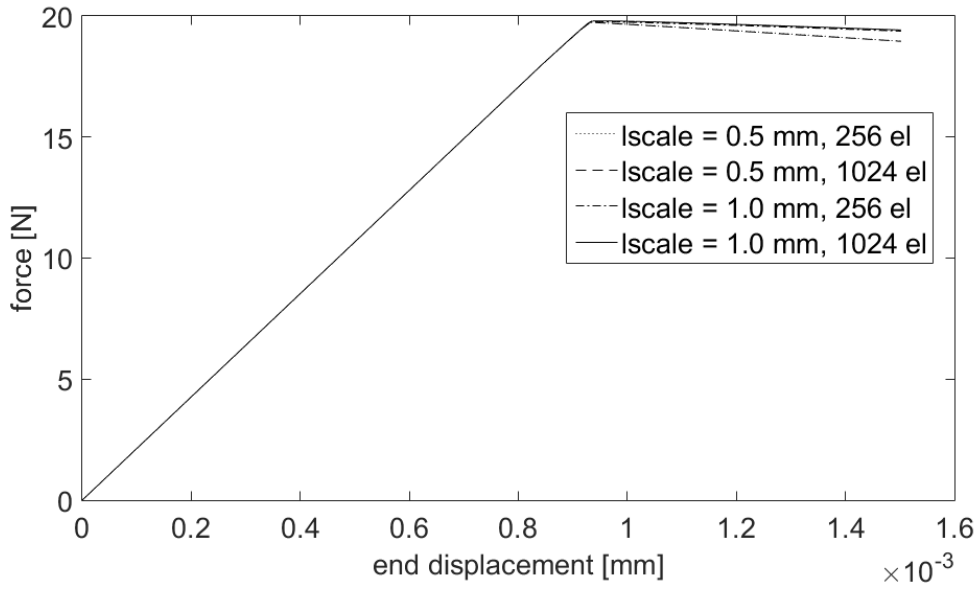

(b)

Figure 3.9: Load-displacement diagrams for square panel (a) using classical plasticity ($\ell = 0$ mm) and gradient plasticity with $\ell = 0.5$ mm and (b) using gradient plasticity with $\ell = 0.5$ mm and $\ell = 1.0$ mm.

3.5 Concluding remarks

An isogeometric approach to gradient-dependent plasticity has been presented in this chapter. Compared to finite element or meshless approaches, isogeometric analysis has the advantage that the displacements and the plastic multiplier can be interpolated with different orders in a straightforward manner, which enables a consistent, equal-order approximation of the strains and the plastic strains. Herein, we have employed NURBS with a cubic interpolation for the displacements and a quadratic interpolation for the plastic multiplier. Through Bézier projection, meshes with matching element boundaries have been obtained.

Compared to finite element approaches that use Hermitian shape functions for the plastic multiplier or mixed finite element approaches, isogeometric analysis has the distinct advantage that no interpolation of derivatives is required. This advantage shows up especially in the boundary conditions, where no non-physical constraints have to be imposed.

The ability of gradient plasticity to maintain the well-posedness of the governing equations for softening problems with the ensuing band width that is mesh-independent, has been demonstrated in an isogeometric analysis framework for one-dimensional and two-dimensional boundary value problems.

While regularisation has been shown for a 2-dimensional problem, steeper ratios of hardening modulus to elastic modulus did not converge. An implicit gradient formulation is thus pursued in the next chapter.

Chapter 4

DISPERSION AND ISOGEOMETRIC ANALYSES OF SECOND-ORDER AND FOURTH-ORDER IMPLICIT GRADIENT-ENHANCED PLASTICITY MODELS[1]

4.1 Introduction

Softening caused by inherent microstructural defects can lead to the formation of localisation bands. Constitutive modelling of this process in the framework of standard continuum plasticity leads to ill-posed problems, which feature unphysical solutions with a vanishing energy dissipation upon refinement of the discretisation. This can be considered as a consequence of the absence of an internal length scale, which causes the localisation band to have a zero width.

This mesh sensitivity is removed when incorporating a length scale in the material description. Often, standard continuum plasticity is enhanced by replacing quantities like the inelastic strain by weighted averages (nonlocal theories) or by adding higher-order gradients of an internal variable such as the accumulated plastic strain (gradient theories). Doing so, a continuum description can ensue which allows for localised solutions, while preserving well-posedness of the boundary value problem [17, 18, 35, 39, 98].

In nonlocal models, volume integrals have to be computed at every material point. This can make such models numerically inefficient, which provides a rationale for developing gradient approximations [14, 45, 110, 139]. Indeed, gradient regularisation

[1]Based on: I. Kolo and R. de Borst. Dispersion and isogeometric analyses of second-order and fourth-order implicit gradient-enhanced plasticity models. *International Journal for Numerical Methods in Engineering*, 114(4):431–453, 2018

can also be considered as an approximation of a fully nonlocal, integral-type model. When a truncated Taylor series of the averaged quantity is substituted in a nonlocal model, a gradient formulation can be derived [100, 113, 139]. It is important to note that the approximation of the nonlocal variable can be based on either the higher-order derivatives of the local variable (explicit formulation), or on the nonlocal variable (implicit formulation). A Taylor series expansion of the nonlocal variable results in an expression which is an explicit formulation with higher-order derivatives on the local variable. When higher-order derivatives of this expression are taken, higher-order derivatives of the nonlocal variable emerge leading to the implicit formulation.

Early studies in plasticity focused on an explicit gradient enhancement, which usually requires C^1-continuity of the shape functions [35]. It has been attempted to satisfy this requirement using Hermitian finite elements [36], using meshless methods [105], and recently, isogeometric analysis [75] as demonstrated in chapter 3. The ability of this explicit gradient plasticity model, in which the yield stress is made a function of the Laplacian of the accumulated plastic strain in addition to the plastic strain itself, to fully regularise the boundary value problem has been demonstrated through one-dimensional dispersion analysis [37], spectral analyses [41, 85, 117], and shear band simulations [36, 105].

The implicit gradient plasticity formulation was proposed to overcome some of the limitations of the explicit gradient plasticity formulation such as (i) difficulty in modelling complete failure, (ii) numerical problems when the total enhanced yield strength approaches zero, and (iii) the additional partial differential equation related to the gradient-enhanced consistency condition is only valid in the plastic region [45]. However, implicit gradient plasticity models with second-order gradients do not fully regularise the boundary-value problem, as has been demonstrated through spectral analysis [41, 66, 117] and three-dimensional simulations [117]. Two approaches have been identified to improve this situation, namely the use of a multiplicative yield function with a damage term, and over-nonlocal implicit gradient plasticity [41, 66, 67]. The localisation properties of both methods have been analysed using one-dimensional spectral analysis and the latter approach has been scrutinised whether it can produce shear-band which are mesh-objective [117]. It is noted that the multiplicative yield

function proposed in [45] can be conceived as a special case of the over-nonlocal formulation which is a linear combination of the local and non-local history variable. In this context, the ratio of the local and non-local moduli determines whether regularisation is achieved or not [44, 67].

The practical use of implicit gradient plasticity models derived from nonlocal averaging seems to be limited to a Taylor series truncated after the second-order gradient [44, 45]. This can be partly attributed to the fact that the ensuing formulation represents a special case of the nonlocal model when an appropriate (Green's) weighting function is adopted [45, 113]. Perhaps more importantly, the formulation requires only $\mathcal{C}^0$-continuity of the shape functions, which is compatible with standard finite elements. However, the inclusion of fourth-order gradients requires $\mathcal{C}^1$-continuity of shape functions, which results in the same continuity requirements as an explicit second-order enrichment, with the computational inconveniences that come with it. Herein, we consider inclusion of second-order gradients as well as fourth-order gradients. Higher-order continuity is achieved using higher-order NURBS shape functions within the context of isogeometric analysis [63].

This chapter expounds the formulation and implementation of implicit gradient-enhanced plasticity models, exploiting isogeometric analysis. The implicit gradient plasticity formulations are presented first. Next, a one-dimensional dispersion analysis is carried out to study the localisation properties of different formulations. The isogeometric finite element discretisation of the field equations is outlined and the interpolation requirements for the discretised variables are highlighted. Bézier extraction [24] is employed to arrive at a standard finite element data structure. One-dimensional simulations and two-dimensional shear band simulations further illustrate the responses of both formulations.

4.2 Implicit gradient-enhanced plasticity

4.2.1 Incremental boundary value problem

We consider the equilibrium equation:

$$\mathbf{L}^{\mathrm{T}}\boldsymbol{\sigma} = \mathbf{0} \tag{4.1}$$

where $\boldsymbol{\sigma} = [\sigma_{xx}, \sigma_{yy}, \sigma_{zz}, \sigma_{xy}, \sigma_{yz}, \sigma_{zx}]^{\mathrm{T}}$ is the stress vector, and $\mathbf{L}$ is the differential operator:

$$\mathbf{L} = \begin{bmatrix} \frac{\partial}{\partial x} & 0 & 0 & \frac{\partial}{\partial y} & \frac{\partial}{\partial z} & 0 \\ 0 & \frac{\partial}{\partial y} & 0 & \frac{\partial}{\partial x} & 0 & \frac{\partial}{\partial z} \\ 0 & 0 & \frac{\partial}{\partial z} & 0 & \frac{\partial}{\partial x} & \frac{\partial}{\partial y} \end{bmatrix}^{\mathrm{T}} . \tag{4.2}$$

Under the assumption of small displacement gradients, the following kinematic relation holds:

$$\boldsymbol{\varepsilon} = \mathbf{L}\mathbf{u} \tag{4.3}$$

with the strain vector $\boldsymbol{\varepsilon} = [\varepsilon_{xx}, \varepsilon_{yy}, \varepsilon_{zz}, \tau_{xy}, \tau_{yz}, \tau_{zx}]^{\mathrm{T}}$ and the displacement vector $\mathbf{u} = [u_x, u_y, u_z]^{\mathrm{T}}$. The incremental constitutive relation between the stress and strain increments is given by:

$$\mathrm{d}\boldsymbol{\sigma} = \mathbf{D}^e(\, \mathrm{d}\boldsymbol{\varepsilon} - \mathrm{d}\boldsymbol{\varepsilon}^p) \tag{4.4}$$

where $\mathbf{D}^e$ is the material elastic stiffness matrix and $\mathrm{d}\boldsymbol{\varepsilon}^p$ is the plastic strain increment vector. An associated plasticity flow rule is adopted:

$$\mathrm{d}\boldsymbol{\varepsilon}^p = \mathrm{d}\lambda \mathbf{m}, \quad \mathbf{m} = \frac{\partial F}{\partial \boldsymbol{\sigma}} \tag{4.5}$$

in which $\mathrm{d}\lambda$ is a non-negative plastic multiplier and $\mathbf{m}$ is a vector that defines the direction of plastic flow relative to the yield function F.

The following yield function is considered [45]:

$$F(\boldsymbol{\sigma}, \kappa, \bar{\kappa}) = \sigma_e(\boldsymbol{\sigma}) - (1 - \omega(\bar{\kappa}))\, \sigma_y(\kappa) \tag{4.6}$$

where $\sigma_e(\boldsymbol{\sigma})$ is the Von Mises equivalent stress, κ is the local effective plastic strain measure, $\bar{\kappa}$ is the nonlocal effective plastic strain measure, $\omega \in [0, 1]$ can be interpreted as a nonlocal damage variable, and σ_y is the yield or flow stress. The yield stress can be written as:

$$\sigma_y = \sigma_{y,0} + H\kappa \tag{4.7}$$

where $\sigma_{y,0}$ is the initial yield strength, and $H > 0$ a hardening modulus. The yield stress is progressively reduced by the factor $(1 - \omega)$ as the damage variable increases from $\omega = 0$ until complete loss of strength, $\omega = 1$. The damage evolution can be de-

scribed by an exponential relation, a power law, or a linear relation, e.g.,

$$\omega(\bar{\kappa}) = \begin{cases} \frac{\bar{\kappa}-\bar{\kappa}_i}{\bar{\kappa}_u-\bar{\kappa}_i} & \text{if } \bar{\kappa} \leq \bar{\kappa}_u \\ 1 & \text{if } \bar{\kappa} > \bar{\kappa}_u \end{cases} \tag{4.8}$$

in which $\bar{\kappa}_i$ is the nonlocal effective plastic strain measure at which damage is initiated and $\bar{\kappa}_u$ is the ultimate nonlocal effective plastic strain measure at complete loss of integrity. The implicit gradient plasticity formulation was proposed to overcome some of the limitations of the explicit gradient plasticity formulation such as (i) difficulty in modelling complete failure, (ii) numerical problems when the total enhanced yield strength approaches zero, and (iii) the additional partial differential equation related to the gradient-enhanced consistency condition is only valid in the plastic region [45]. However, the implicit formulation with a standard yield function leads to only partial regularisation [66, 117]. To achieve full regularisation, the yield function is modified using a damage variable [45]. The motivation for using damage is, on one hand to ensure proper regularisation, and on the other hand to properly capture the material softening. Different from the yield function used in chapter 3 where a softening modulus is directly used, this yield function only allows a (positive) hardening modulus. Degradation in material integrity is incorporated through damage.

The hardening parameter κ is related to the plastic multiplier λ according to the strain-hardening hypothesis:

$$\mathrm{d}\kappa = \sqrt{\frac{2}{3}(\mathrm{d}\boldsymbol{\varepsilon}^p)^{\mathrm{T}}\mathbf{P}\mathrm{d}\boldsymbol{\varepsilon}^p} \tag{4.9}$$

where, cf. [34],

$$\mathbf{P} = \begin{bmatrix} \frac{2}{3} & -\frac{1}{3} & -\frac{1}{3} & 0 & 0 & 0 \\ -\frac{1}{3} & \frac{2}{3} & -\frac{1}{3} & 0 & 0 & 0 \\ -\frac{1}{3} & -\frac{1}{3} & \frac{2}{3} & 0 & 0 & 0 \\ 0 & 0 & 0 & \frac{1}{2} & 0 & 0 \\ 0 & 0 & 0 & 0 & \frac{1}{2} & 0 \\ 0 & 0 & 0 & 0 & 0 & \frac{1}{2} \end{bmatrix}. \tag{4.10}$$

Substitution of the flow rule, Equation (4.5) into the strain-hardening hypothesis, Equation (4.9), then yields $\mathrm{d}\kappa = \mathrm{d}\lambda$. The yield function F and the plastic multiplier

$\mathrm{d}\lambda$ obey the the Karush-Kuhn-Tucker loading-unloading conditions, similar to standard plasticity:

$$\mathrm{d}\lambda \geq 0, \quad F \leq 0, \quad F\mathrm{d}\lambda = 0 \tag{4.11}$$

The nonlocal effective plastic strain measure, $\bar{\kappa}(\mathbf{x})$, can be defined as the volume average of the local effective plastic strain measure, $\kappa = \kappa(\boldsymbol{\varepsilon}^p)$, as follows:

$$\bar{\kappa}(\mathbf{x}) = \frac{\int_\Omega \phi(\mathbf{x},\mathbf{y})\kappa(\mathbf{y})\mathrm{d}\Omega}{\int_\Omega \phi(\mathbf{x},\mathbf{y})\mathrm{d}\Omega} \tag{4.12}$$

where $\mathbf{y}$ is the position vector of the infinitesimal volume $\mathrm{d}\Omega$ and ϕ is a weight function. A Gaussian weight function is often assumed:

$$\phi(\mathbf{x},\mathbf{y}) = \frac{1}{(2\pi)^{3/2}\ell^3}\exp\left[-\frac{\|\mathbf{x}-\mathbf{y}\|^2}{2\ell^2}\right] \tag{4.13}$$

where ℓ is a length scale that sets the averaging volume. The nonlocal formulation in Equation (4.12) requires the computation of a volume integral at each material point, which is cumbersome and leads to inefficiency. This is usually obviated by using a gradient approximation of the nonlocal model, e.g., [113, 139].

The nonlocal hardening parameter $\bar{\kappa}$ can be approximated when $\kappa(\mathbf{y})$ is expanded in a Taylor series around $\mathbf{x}$,

$$\kappa(\mathbf{y}) = \kappa|_{\mathbf{y}=\mathbf{x}} + \left.\frac{\partial\kappa}{\partial y_i}\right|_{\mathbf{y}=\mathbf{x}}(y_i - x_i) + \frac{1}{2!}\left.\frac{\partial\kappa}{\partial y_i}\right|_{\mathbf{y}=\mathbf{x}}(y_i - x_i)(y_j - x_j) + \mathcal{O}((x_i - y_i)^3) \tag{4.14}$$

Substitution into Equation (4.12) and integration in $\mathbb{R}^3$ leads to:

$$\bar{\kappa}(\mathbf{x}) = \kappa(\mathbf{x}) + c_1\nabla^2\kappa(\mathbf{x}) + c_2\nabla^4\kappa(\mathbf{x}) + c_3\nabla^6\kappa(\mathbf{x}) + \cdots \tag{4.15}$$

in which $\nabla^{2n} = (\nabla^2)^n$ and $\nabla^2 = \sum_i \frac{\partial^2}{\partial x_i^2}$. The coefficients $c_i(\ell)$ depend on the nonlocal averaging function ϕ, and odd derivatives vanish in the integration process due to the isotropic character of ϕ [14, 139]. The nonlocal effective plastic strain measure, $\bar{\kappa}$, can be approximated by truncating the series in Equation (4.15) after the second-order term. This gradient approximation is known as the *explicit gradient formulation* and it requires $\mathcal{C}^1$-continuous shape functions for the interpolation of κ.

We next take the second-order derivative of Equation (4.15), multiply by c_1 and substitute the result back into Equation (4.15). This gives [14]:

$$\bar{\kappa}(\mathbf{x}) - c_1\nabla^2\bar{\kappa}(\mathbf{x}) = \kappa(\mathbf{x}) + (c_2 - c_1^2)\nabla^4\kappa(\mathbf{x}) + (c_3 - c_1c_2)\nabla^6\kappa(\mathbf{x}) + \cdots \tag{4.16}$$

A formulation requiring only $\mathcal{C}^0$-continuous shape functions is obtained when fourth-order and higher-order terms are omitted in Equation (4.16) [14, 110]. This implies that coefficients of higher-order terms are set equal to zero, starting with $c_2 - c_1^2 = 0$. It is noted that when Green's weighting function

$$\phi(\mathbf{x}, \mathbf{y}) = \frac{1}{4\pi\|\mathbf{x}-\mathbf{y}\|\ell^2}\exp\left[-\frac{\|\mathbf{x}-\mathbf{y}\|}{\ell}\right] \tag{4.17}$$

$\|\mathbf{x}-\mathbf{y}\|$ being the distance between two points, is substituted for ϕ, no higher-order terms are neglected [45, 113]. The coefficient c_1 then reads:

$$c_1(\ell) = \ell^2. \tag{4.18}$$

Accordingly, the *second-order implicit gradient formulation* is given by:

$$\bar{\kappa}(\mathbf{x}) - \ell^2\nabla^2\bar{\kappa}(\mathbf{x}) = \kappa(\mathbf{x}) \tag{4.19}$$

When we include the fourth-order derivatives of Equation (4.15), multiply by the terms c_i and substitute the result back into Equation (4.15), the following expression ensues:

$$\bar{\kappa}(\mathbf{x}) - c_1\nabla^2\bar{\kappa}(\mathbf{x}) - (c_2 - c_1^2)\nabla^4\bar{\kappa}(\mathbf{x}) = \kappa(\mathbf{x}) + (c_3 - 2c_1c_2 - c_1^3)\nabla^6\kappa(\mathbf{x}) + \cdots \tag{4.20}$$

For the Gaussian weight function, $c_1 = \frac{1}{2}\ell^2$, $c_2 = \frac{1}{8}\ell^4$, etc. [112]. When these coefficients are substituted into Equation (4.20) and sixth-order and higher-order terms are neglected, we obtain the *fourth-order implicit gradient formulation*:

$$\bar{\kappa}(\mathbf{x}) - \frac{1}{2}\ell^2\nabla^2\bar{\kappa}(\mathbf{x}) + \frac{1}{8}\ell^4\nabla^4\bar{\kappa}(\mathbf{x}) = \kappa(\mathbf{x}). \tag{4.21}$$

For the implicit gradient formulations, the strain-hardening hypothesis is assumed to hold for $\bar{\kappa}$. A state variable $\bar{\lambda}$ is defined as

$$\bar{\lambda}(t) = \max\{\bar{\kappa}(\tau)|0 \leq \tau \leq t\} \tag{4.22}$$

such that:

$$\mathrm{d}\bar{\lambda} \geq 0, \quad \bar{\kappa} - \bar{\lambda} \leq 0, \quad \mathrm{d}\bar{\lambda}\left[\bar{\kappa} - \bar{\lambda}\right] = 0 \tag{4.23}$$

Standard static and kinematic boundary conditions are specified on complementary parts of the body surface S:

$$\boldsymbol{\Upsilon}\mathbf{n}_s = \mathbf{t}, \quad \mathbf{u} = \mathbf{u}_s \tag{4.24}$$

where $\boldsymbol{\Upsilon}$ denotes the stress tensor in matrix form, $\mathbf{n}_s$ is the outward normal to the surface S, and $\mathbf{t}$ is the boundary traction vector. Natural boundary conditions apply on the odd derivatives of $\bar{\kappa}$ [14]:

$$(\mathbf{n}_s^{\mathrm{T}}\nabla)\nabla^n\bar{\kappa} = 0, \quad n = 0, 2 \tag{4.25}$$

4.2.2 Weak formulation

The weak form of the governing equations is obtained by setting:

$$\int_V \delta\mathbf{u}^{\mathrm{T}}(\mathbf{L}^{\mathrm{T}}\boldsymbol{\sigma}_{j+1})\mathrm{d}V = \mathbf{0} \tag{4.26}$$

and

$$\int_V \delta\bar{\lambda}\Big(\bar{\kappa}_{j+1} - c_a\nabla^2\bar{\kappa}_{j+1} + c_b\nabla^4\bar{\kappa}_{j+1} - \kappa_{j+1}\Big)\mathrm{d}V = 0 \tag{4.27}$$

where δ denotes the variation of a quantity. We obtain the second-order implicit gradient formulation when $c_a = \ell^2$ and $c_b = 0$, while the fourth-order formulation is obtained when $c_a = \frac{1}{2}\ell^2$ and $c_b = \frac{1}{8}\ell^4$. Integrating by parts and applying the divergence theorem yields:

$$\int_V \delta\boldsymbol{\varepsilon}^{\mathrm{T}}\boldsymbol{\sigma}_{j+1}\mathrm{d}V - \int_S \delta\mathbf{u}^{\mathrm{T}}\mathbf{t}_{j+1}\mathrm{d}S = \mathbf{0} \tag{4.28}$$

and

$$\int_V \Big(\delta\bar{\lambda}\bar{\kappa}_{j+1} - c_a(\nabla\delta\bar{\lambda})^{\mathrm{T}}(\nabla\bar{\kappa}_{j+1}) + c_b\nabla^2\delta\bar{\lambda}\nabla^2\bar{\kappa}_{j+1} - \delta\bar{\lambda}\kappa_{j+1}\Big)\mathrm{d}V = 0 \tag{4.29}$$

where the boundary condition (4.25) has been substituted in Equation (4.29), and the boundary condition for $\mathbf{t}$, Equation $(4.24)_1$, is applied along the entire external boundary S of the body V.

The following linearisations are carried out at iteration $j+1$ for use in a Newton-Raphson iterative solution procedure:

$$\boldsymbol{\sigma}_{j+1} = \boldsymbol{\sigma}_j + \mathrm{d}\boldsymbol{\sigma}, \quad \kappa_{j+1} = \kappa_j + \mathrm{d}\kappa, \quad \bar{\kappa}_{j+1} = \bar{\kappa}_j + \mathrm{d}\bar{\kappa} \tag{4.30}$$

where d represents an iterative contribution. Substituting Equation $(4.30)_1$ into Equations (4.28) and using (4.4) gives the weak form:

$$\int_V \delta\boldsymbol{\varepsilon}^{\mathrm{T}}\mathbf{D}^e(\,\mathrm{d}\boldsymbol{\varepsilon} - \mathrm{d}\lambda\mathbf{m})dV = \int_S \delta\mathbf{u}^{\mathrm{T}}\mathbf{t}_{j+1}\mathrm{d}S - \int_V \delta\boldsymbol{\varepsilon}^{\mathrm{T}}\boldsymbol{\sigma}_j\mathrm{d}V \tag{4.31}$$

Similarly, Equations $(4.30)_{2,3}$ are substituted into Equation (4.29) to give

$$\begin{aligned}\int_V \Big(\delta\bar{\lambda}\mathrm{d}\bar{\kappa} - c_a(\nabla\delta\bar{\lambda})^{\mathrm{T}}(\nabla\mathrm{d}\bar{\kappa}) + c_b\nabla^2\delta\bar{\lambda}\nabla^2\mathrm{d}\bar{\kappa} - \delta\bar{\lambda}\mathrm{d}\kappa\Big)\mathrm{d}V = \\ -\int_V \Big(\delta\bar{\lambda}\bar{\kappa}_j - c_a(\nabla\delta\bar{\lambda})^{\mathrm{T}}(\nabla\bar{\kappa}_j) + c_b\nabla^2\delta\bar{\lambda}\nabla^2\bar{\kappa}_j - \delta\bar{\lambda}\kappa_j\Big)\mathrm{d}V\end{aligned} \tag{4.32}$$

4.2.3 Stress update

Similar to standard elastoplasticity, the stress update is computed as an integral along a given path from the initial state $(\boldsymbol{\sigma}_0, \boldsymbol{\varepsilon}_0)$ to the final state $(\boldsymbol{\sigma}_{j+1}, \boldsymbol{\varepsilon}_{j+1})$:

$$\boldsymbol{\sigma} = \boldsymbol{\sigma}_0 + \int_{\boldsymbol{\varepsilon}_0}^{\boldsymbol{\varepsilon}_{j+1}} \mathbf{D}^e \mathrm{d}\boldsymbol{\varepsilon} \tag{4.33}$$

The algorithmic stress update in iteration $j+1$ follows the format [36]:

$$\boldsymbol{\sigma}_{j+1} = \boldsymbol{\sigma}_0 + \mathbf{S}(\boldsymbol{\varepsilon}_0, \boldsymbol{\Delta\varepsilon}_{j+1}) \tag{4.34}$$

where $\mathbf{S}$ is a non-linear mapping operator and $\boldsymbol{\Delta}$ is the sum of increments in all iterations for the current load step:

$$\boldsymbol{\Delta\varepsilon}_{j+1} = \sum_{i=1}^{j+1} \mathrm{d}\boldsymbol{\varepsilon}_i \tag{4.35}$$

The yield function is evaluated at every iteration $j+1$ as [45]:

$$F_t = F(\boldsymbol{\sigma}_t, \kappa_0, \bar{\kappa}_{j+1}) = \sigma_{e,t} - \sigma_{y,0}\big(1 - \omega_{j+1}\big) \tag{4.36}$$

where $(\bullet)_{\bullet,t}$ indicates use of the trial stress which is given by:

$$\boldsymbol{\sigma}_t = \boldsymbol{\sigma}_0 + \mathbf{D}^e \Delta\boldsymbol{\varepsilon}_{j+1}. \tag{4.37}$$

and $(\bullet)_0$ denotes value at previous converged load step. If $F_t \leq 0$, we have an elastic state and the stress is updated as $\boldsymbol{\sigma}_{j+1} = \boldsymbol{\sigma}_t$. When $F_t > 0$, we have a plastic state which is updated by [35, 117]:

$$\boldsymbol{\sigma}_{j+1} = \boldsymbol{\sigma}_t - \Delta\gamma_{j+1}\mathbf{D}^e\mathbf{m}_t \tag{4.38}$$

where $\mathbf{m}_t$ is given by Equation $(4.5)_2$, and $\Delta\gamma_{j+1}$ is the amount of plastic strain for the current iteration, expressed as [45],

$$\Delta\gamma_{j+1} = \frac{F_t}{H\big[1-\omega_{j+1}\big]\big[\frac{\partial\kappa}{\partial\bar{\lambda}}\big] + \frac{3E}{2(1+\nu)}} \tag{4.39}$$

in which E is the Young's modulus and ν is the Poisson ratio. This ensures that the consistency condition is satisfied.

4.3 Dispersion analyses

We consider the one-dimensional equation of motion for a bar under uniform tensile loading in rate form:

$$\frac{\partial \dot{\sigma}}{\partial x} = \rho \frac{\partial^2 \dot{u}}{\partial t^2} \tag{4.40}$$

where σ is the stress, ρ is the mass density, u is the displacement, and $(\dot{\bullet})$ denotes the time derivative. The rate of deformation is expressed as

$$\dot{\varepsilon} = \frac{\partial \dot{u}}{\partial x}. \tag{4.41}$$

An additive decomposition of the strain holds, so that Hooke's law is given by:

$$\dot{\sigma} = E(\dot{\varepsilon} - \dot{\kappa}) \tag{4.42}$$

The current yield stress has a multiplicative format:

$$\sigma_y = (1 - \omega(\bar{\kappa}))\,(\sigma_{y,0} + H\kappa) \tag{4.43}$$

while the stress rate $\dot{\sigma}$ has to satisfy the consistency condition: $\dot{F} \equiv \dot{\sigma} - \dot{\sigma}_y = 0$. Differentiating Equation (4.43) with respect to time yields [67]:

$$\dot{\sigma}_y = \underbrace{(1-\omega)H}_{H_L}\,\dot{\kappa} + \underbrace{\omega'(-\sigma_{y,0} - H\kappa)}_{H_N}\,\dot{\bar{\kappa}} \tag{4.44}$$

in which $\omega' = \mathrm{d}\omega/\mathrm{d}\bar{\kappa}$, and H_L and H_N can be considered as the current local and nonlocal plastic moduli, respectively. The time derivative of Equation (4.21) reads:

$$\dot{\bar{\kappa}} - c_a \nabla^2 \dot{\bar{\kappa}} + c_b \nabla^4 \dot{\bar{\kappa}} = \dot{\kappa}. \tag{4.45}$$

For a dispersion analysis, we consider the following harmonic functions

$$\dot{u} = \hat{u}\mathrm{e}^{ik(x-ct)}, \quad \dot{\kappa} = \hat{\kappa}\mathrm{e}^{ik(x-ct)}, \quad \dot{\bar{\kappa}} = \hat{\bar{\kappa}}\mathrm{e}^{ik(x-ct)} \tag{4.46}$$

with k the wave number, c the phase velocity, and the amplitudes $\hat{u}$, $\hat{\kappa}$ and $\hat{\bar{\kappa}}$. The amplitudes $\hat{\kappa}$ and $\hat{\bar{\kappa}}$ can be related by substituting the respective harmonic fields into Equation (4.45). Using the result together with Equations (4.41) and (4.42), the amplitude of the plastic strain, $\hat{\kappa}$, can be related to $\hat{u}$, the amplitude of the displacement.

Subsequently, satisfaction of the consistency condition can be exploited to equal the right-hand sides of Equations (4.42) and (4.44). The resulting expression reads:

$$Ek^2\left[\frac{H_L(1+c_ak^2+c_bk^4)+H_N}{(H_L+E)(1+c_ak^2+c_bk^4)+H_N}\right]=\rho k^2c^2 \tag{4.47}$$

Using the bar velocity, $c_e=\sqrt{E/\rho}$, the phase velocity c can be expressed as:

$$\frac{c^2}{c_e^2}=\left[\frac{H_L(1+c_ak^2+c_bk^4)+H_N}{(H_L+E)(1+c_ak^2+c_bk^4)+H_N}\right]. \tag{4.48}$$

The normalised wave velocity c/c_e is plotted as a function of the normalised wave number $k\ell$ in Figure 4.1 for $H_L=1819\ \mathrm{N/mm^2}$, $H_N=-2148\ \mathrm{N/mm^2}$, $E=20000\ \mathrm{N/mm^2}$ and $\ell=1.0\ \mathrm{mm}$, being representative values for a low-strength concrete. For comparison, the dispersion relation for the explicit gradient plasticity model [37],

$$\frac{c^2}{c_e^2}=\left[\frac{H_E+gk^2}{E+H_E+gk^2}\right] \tag{4.49}$$

has been plotted in the same figure for a softening modulus $H_E=-329\ \mathrm{N/mm^2}$ and $g=-\ell^2H_E$. The frequency $\omega=kc$ is a function of wave number, $\omega=\omega(k)$. Since $\omega''(k)\neq 0$, wave propagation is dispersive [37, 144]. It is noted that emphasis is on the comparison of the regularisation properties of the models considered.

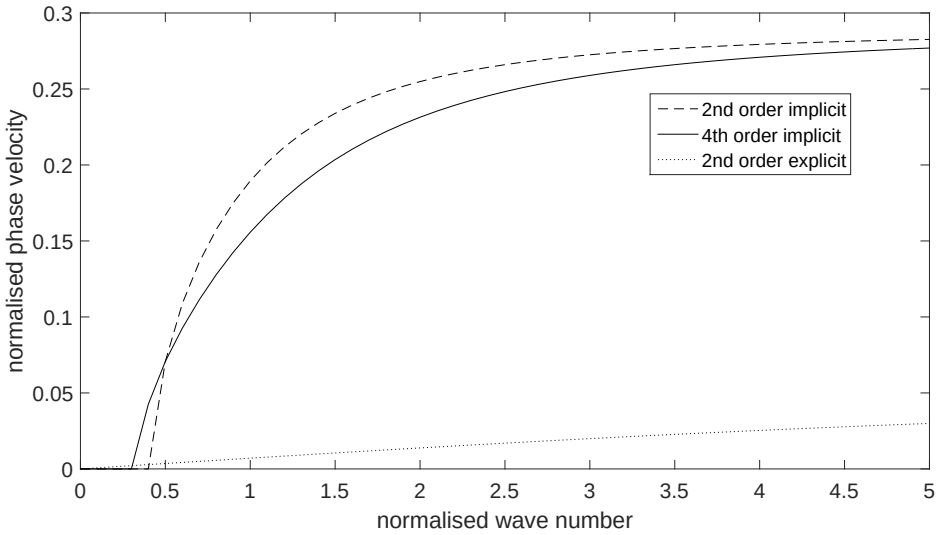

Figure 4.1: Normalised phase velocity c/c_e as a function of normalised wave number $k\ell$.

The critical wave number k_{crit} is the minimum wave number below which only imaginary values of phase velocity exist. It is obtained by setting the phase velocity $c = 0$. The critical wave length $\mu_{crit} = 2\pi/k_{crit}$ is the wave length above which no waves will propagate:

$$\begin{aligned}
&\text{second-order implicit formulation} \quad \mu_{crit} = 2\pi\ell\sqrt{-\frac{(H_N + H_L)}{H_L}} \\
&\text{fourth-order implicit formulation} \quad \mu_{crit} = 2\pi\ell\sqrt{-2 + 2\sqrt{\frac{-(H_L + 2H_N)}{H_L}}} \\
&\text{second-order explicit formulation} \quad \mu_{crit} = 2\pi\ell
\end{aligned} \tag{4.50}$$

We now proceed by using the linear damage relation of Equation (4.8) and use this to derive the expressions for the local and nonlocal hardening moduli for the implicit gradient plasticity formulation:

$$H_L = \begin{cases} H\left(1 - \frac{\bar{\kappa} - \bar{\kappa}_i}{\bar{\kappa}_u - \bar{\kappa}_i}\right) & \text{if } \bar{\kappa} \leq \bar{\kappa}_u \\ 0 & \text{if } \bar{\kappa} > \bar{\kappa}_u \end{cases} \tag{4.51}$$

and

$$H_N = \begin{cases} -(\sigma_{y,0} + H\kappa)\left(\frac{1}{\bar{\kappa}_u - \bar{\kappa}_i}\right) & \text{if } \bar{\kappa} \leq \bar{\kappa}_u \\ 0 & \text{if } \bar{\kappa} > \bar{\kappa}_u \end{cases} \tag{4.52}$$

The normalised critical wave length μ_{crit}/ℓ is plotted *vs* the strain level $\kappa = \bar{\kappa}$ in Figure 4.2 for $\bar{\kappa}_i = 0$, $\bar{\kappa}_u = 0.001$, $H = 2000$ N/mm^2 and $\sigma_{y,0} = 2$ N/mm^2. For the explicit gradient plasticity formulation, the critical wavelength is non-zero and independent of the accumulated damage, so that there is localisation into a non-zero band width. For the implicit gradient plasticity formulations, a non-zero band width results, except when the damage attains a maximum, when the localisation width becomes zero. It has been argued that this can be conceived as an an advantage of implicit gradient plasticity formulations, since they ultimately result in a sharp crack [45]. Conversely, it can be considered as a disadvantage, as in the limiting case of a sharp crack, the topology changes and boundary conditions have to be supplied locally in order to keep the boundary value problem well-posed.

Indeed, the critical wave length represents the width of the localisation band. It is clear from Figure 4.2 that, at the initial stages of the deformation, the second-order

implicit formulation has a localisation band that is wider than that which results from the fourth-order implicit formulation. However, at some point, before complete failure, the localisation band width of the fourth-order formulation becomes higher, and remains so.

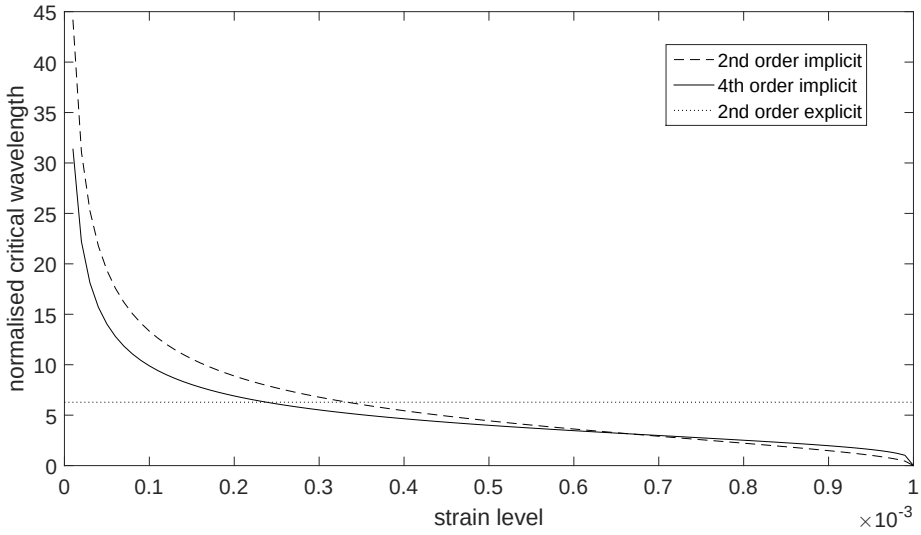

Figure 4.2: Normalised critical wavelength μ_{crit}/ℓ *vs* the strain level $\kappa = \bar{\kappa}$ for a piecewise linear damage law.

When using an exponential damage law [45], for instance

$$\omega = 1 - \mathrm{e}^{-\beta\bar{\kappa}} \tag{4.53}$$

the results become different, see Figure 4.3 for $\beta = 1000$. Now, neither the explicit formulation, nor either of the implicit gradient plasticity formulations result in a zero critical wave length at complete damage, and thus, convergence to a line crack does not take place in either of the cases which have been considered. As a minor detail we note that the band width of the second-order gradient plasticity model remains wider than that of the fourth-order model for all strain levels.

The relations for the critical wave length, Equations (4.50), indicate that the sum of the local and nonlocal hardening moduli, H_L and H_N determine whether or not regularisation is achieved for the implicit gradient formulations. For the second-order implicit gradient plasticity formulation, $H_L + H_N$ has to be negative. According to the adopted

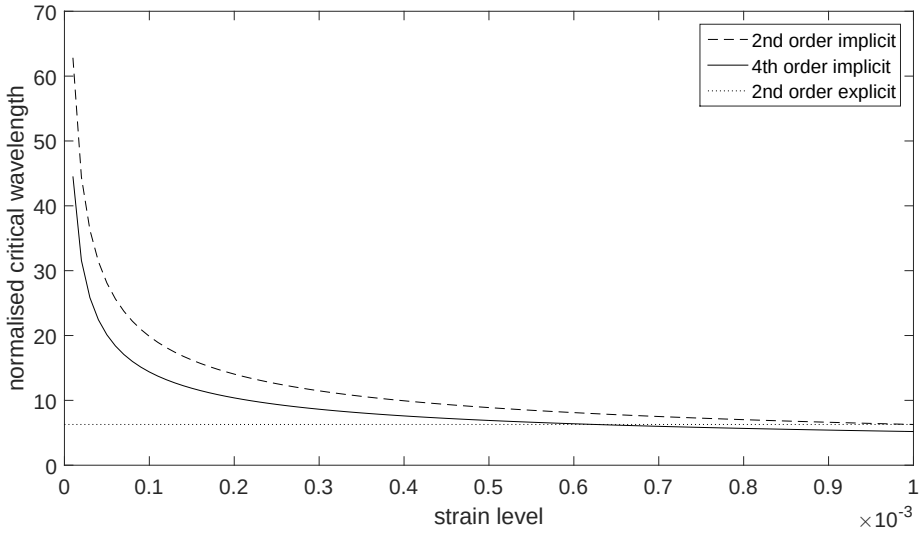

Figure 4.3: Normalised critical wavelength μ_{crit}/ℓ *vs* the strain level $\kappa = \bar{\kappa}$ for an exponential damage law.

yield function, Equation (4.43), H_L is always positive and H_N is always negative because $H > 0$. The sum of the two moduli is initially positive but at a certain loading stage, it becomes negative. The same holds for the fourth-order implicit gradient plasticity formulation, except that now the sum under consideration is $H_L + 2H_N$. For the second-order explicit formulation, $H_E < 0$, and regularisation is always achieved.

The behaviour of localised zones in softening systems depends on the dispersive properties of the material [133, 134]. At wave lengths below μ_{crit}, waves with real phase velocities exhibit dispersion. Hence, the localisation zone can extend, and the strain profile in the localisation zone can be transformed due to different modes travelling at different speeds. In the static case, phase velocity $c = 0$, the localisation zone acts as a stationary wave and the width of the localisation zone is equal to the lowest-order wave that the system can transmit [37, 134].

4.4 Isogeometric finite element discretisation

See section 2.3 and section 3.3 for a description of NURBS shape functions as well as their Bézier element representation.

4.4.1 Orders of interpolation

The displacement field, $\mathbf{u}$, and the nonlocal effective plastic strain measure (nonlocal plastic multiplier), $\bar{\lambda}$, are discretised as follows:

$$\mathbf{u} = \mathbf{N}\mathbf{a} \tag{4.54}$$

and

$$\bar{\lambda} = \mathbf{h}^{\mathrm{T}}\bar{\mathbf{\Lambda}} \tag{4.55}$$

where $\mathbf{a}$ is a vector of discrete displacements at the control points, $\bar{\mathbf{\Lambda}}$ is a vector of the nonlocal plastic multiplier degrees of freedom at the control point, $\mathbf{N}$ is a matrix, and $\mathbf{h}$, a vector, both containing NURBS shape functions. Based on the linear kinematic relation (4.3), the strain vector can be expressed as:

$$\boldsymbol{\varepsilon} = \mathbf{B}\mathbf{a} \tag{4.56}$$

where $\mathbf{B} = \mathbf{L}\mathbf{N}$. In a similar way, the gradient of the nonlocal plastic multiplier $\nabla\bar{\lambda}$ and its Laplacian can be discretised as:

$$\nabla\bar{\lambda} = \mathbf{Q}^{\mathrm{T}}\bar{\mathbf{\Lambda}} \tag{4.57}$$

$$\nabla^2\bar{\lambda} = \mathbf{p}^{\mathrm{T}}\bar{\mathbf{\Lambda}} \tag{4.58}$$

where

$$\mathbf{Q} = [\nabla h_1, \nabla h_2, \ldots, \nabla h_{ns}]^{\mathrm{T}} \tag{4.59}$$

$$\mathbf{p} = [\nabla^2 h_1, \nabla^2 h_2, \ldots, \nabla^2 h_{ns}]^{\mathrm{T}} \tag{4.60}$$

and ns the number of shape functions at each control point. The interpolation functions contained in $\mathbf{h}$ must be C^0-continuous and C^1-continuous for the second-order and fourth-order formulations, respectively. Quadratic NURBS are used for $\mathbf{h}$, and since the strain vector (which is of the same order as the nonlocal plastic multiplier) is one order lower than the displacement, cubic NURBS are used for $\mathbf{N}$. This is investigated further in Section 4.5.

To construct conforming meshes of different orders and matching element boundaries, we use Bézier projection [140]:

$$\mathbf{P}^{e,p'} = (\mathbf{R}^{e,p'})^{\mathrm{T}}(\mathbf{E}^{p,p'})^{\mathrm{T}}(\mathbf{C}^{e,p})^{\mathrm{T}}(\mathbf{P}^{e,p}) \tag{4.61}$$

where $\mathbf{P}^{e,p}$ contains the control points of the initial curve of order p, $\mathbf{P}^{e,p'}$ contains the control points of the target curve of order p', $\mathbf{C}^{e,p}$ contains the initial Bézier extraction operator, $\mathbf{R}^{e,p'}$ is the inverse of the target Bézier extraction operator, i.e. $\mathbf{R}^{e,p'} = (\mathbf{C}^{e,p'})^{-1}$, and $\mathbf{E}^{p,p'}$ is the elevation matrix from degree p to p'. It is noted that the Bézier extraction/projection procedure preserves the original continuity.

4.4.2 Spatial discretisation

The interpolation functions of Equations (4.54)–(4.55) are used to discretise the weak forms, Equations (4.31) and (4.32). Requiring that the result must hold for all admissible $\delta\mathbf{a}$ and $\delta\mathbf{\Lambda}$ leads to the following set of non-linear algebraic equations [45]:

$$\begin{bmatrix} \mathbf{K}_{aa} & \mathbf{K}_{a\lambda} \\ \mathbf{K}_{\lambda a} & \mathbf{K}_{\lambda\lambda} \end{bmatrix} \begin{bmatrix} \mathrm{d}\mathbf{a} \\ \mathrm{d}\bar{\mathbf{\Lambda}} \end{bmatrix} = \begin{bmatrix} \mathbf{f}_e - \mathbf{f}_a \\ -\mathbf{f}_\lambda \end{bmatrix} \tag{4.62}$$

with the elastic stiffness matrix

$$\mathbf{K}_{aa} = \int_V \mathbf{B}^{\mathrm{T}} \mathbf{A}_{aa} \mathbf{B} \mathrm{d}V, \tag{4.63}$$

the off-diagonal matrices

$$\mathbf{K}_{a\lambda} = -\int_V \mathbf{B}^{\mathrm{T}} \mathbf{A}_{a\lambda} \mathbf{h} \, \mathrm{d}V, \quad \mathbf{K}_{\lambda a} = -\int_V \mathbf{h}^{\mathrm{T}} \mathbf{A}_{\lambda a} \mathbf{B} \, \mathrm{d}V, \tag{4.64}$$

the gradient-dependent matrix

$$\mathbf{K}_{\lambda\lambda} = \int_V \mathbf{h}^{\mathrm{T}} \big(1 - A_{\lambda\lambda}\big) \mathbf{h} + c_a \mathbf{Q}^{\mathrm{T}} \mathbf{Q} + c_b \mathbf{p}^{\mathrm{T}} \mathbf{p} \, \mathrm{d}V, \tag{4.65}$$

the external force vector

$$\mathbf{f}_e = \int_S \mathbf{N}^{\mathrm{T}} \mathbf{t}_{j+1} \mathrm{d}S, \tag{4.66}$$

the vector of control point forces (equivalent to internal stresses)

$$\mathbf{f}_a = -\int_V \mathbf{B}^{\mathrm{T}} \boldsymbol{\sigma}_j \mathrm{d}V, \tag{4.67}$$

and the vector associated with the nonlocal averaging

$$\mathbf{f}_\lambda = \mathbf{K}_\lambda \bar{\lambda}_j - \int_V \mathbf{h}^{\mathrm{T}} \lambda_j \, \mathrm{d}V \tag{4.68}$$

where

$$\mathbf{K}_\lambda = \int_V \mathbf{h}^{\mathrm{T}} \mathbf{h} + c_a \mathbf{Q}^{\mathrm{T}} \mathbf{Q} + c_b \mathbf{p}^{\mathrm{T}} \mathbf{p} \, \mathrm{d}V. \tag{4.69}$$

The arrays $\mathbf{A}_{aa}$, $\mathbf{A}_{a\lambda}$ and $\mathbf{A}_{\lambda a}$, and the scalar $\mathbf{A}_{\lambda\lambda}$ are defined as [45, 117]:

$$\mathbf{A}_{aa} = \mathbf{A} - \frac{\mathbf{A}\mathbf{m}\mathbf{m}^{\mathrm{T}}\mathbf{A}}{H\big(1-\omega\big)\big(\frac{\partial\kappa}{\partial\lambda}\big) + \frac{3E}{2(1+\nu)}} \tag{4.70}$$

$$\mathbf{A}_{a\lambda} = \frac{\sigma_y\big(\frac{\partial\omega}{\partial\bar{\kappa}}\big)\big(\frac{\partial\bar{\kappa}}{\partial\lambda}\big)\mathbf{A}\mathbf{m}}{H\big(1-\omega\big)\big(\frac{\partial\kappa}{\partial\lambda}\big) + \frac{3E}{2(1+\nu)}} \tag{4.71}$$

$$\mathbf{A}_{\lambda a} = \frac{\mathbf{m}^{\mathrm{T}}\mathbf{A}}{H\big(1-\omega\big)\big(\frac{\partial\kappa}{\partial\lambda}\big) + \frac{3E}{2(1+\nu)}} \tag{4.72}$$

$$A_{\lambda\lambda} = \frac{\sigma_y\big(\frac{\partial\omega}{\partial\bar{\kappa}}\big)\big(\frac{\partial\bar{\kappa}}{\partial\lambda}\big)}{H\big(1-\omega\big)\big(\frac{\partial\kappa}{\partial\lambda}\big) + \frac{3E}{2(1+\nu)}} \tag{4.73}$$

respectively, where $\mathbf{A}$ is the algorithmic stiffness operator

$$\mathbf{A} = \left[(\mathbf{D}^e)^{-1} + \Delta\gamma\frac{\partial\mathbf{m}}{\partial\boldsymbol{\sigma}}\right]^{-1} \tag{4.74}$$

A concise algorithm is given in Box 4.1.

1. Compute the matrices $\mathbf{K}_{aa}$, $\mathbf{K}_{a\lambda}$, $\mathbf{K}_{\lambda a}$ and $\mathbf{K}_{\lambda\lambda}$, and forces f_e, f_a and f_λ, according to Equations (4.63) – (4.68)

2. Solve for $\mathrm{d}\mathbf{a}$ and $\mathrm{d}\bar{\boldsymbol{\Lambda}}$ using Equation (4.62)

3. Update the total increments $\Delta\mathbf{a}_{j+1} = \Delta\mathbf{a}_j + \mathrm{d}\mathbf{a}$, and $\Delta\boldsymbol{\Lambda}_{j+1} = \Delta\boldsymbol{\Lambda}_j + \mathrm{d}\boldsymbol{\Lambda}$.

4. Compute the following at each integration point:

   $\Delta\boldsymbol{\varepsilon}_{j+1} = \mathbf{B}\Delta\mathbf{a}_{j+1}$,

   $\Delta\bar{\lambda}_{j+1} = \mathbf{h}^{\mathrm{T}}\Delta\bar{\boldsymbol{\Lambda}}_{j+1}$,

   $\nabla^2(\Delta\lambda_{j+1}) = \mathbf{p}^{\mathrm{T}}\Delta\boldsymbol{\Lambda}_{j+1}$,

   $\bar{\kappa}_{j+1} = \bar{\kappa}_0 + \Delta\lambda_{j+1}$,

   $\nabla^2\bar{\kappa}_{j+1} = \nabla^2\bar{\kappa}_0 + \nabla^2(\Delta\bar{\lambda}_{j+1})$,

   compute ω_{j+1} according to adopted damage evolution law

   trial stress $\boldsymbol{\sigma}_t = \boldsymbol{\sigma}_0 + \mathbf{D}^e\Delta\boldsymbol{\varepsilon}_{j+1}$.

   If $F(\boldsymbol{\sigma}_t, \kappa_0, \bar{\kappa}_{j+1}) > 1 \times 10^{-6}$,

   then plastic state:

   compute $\mathbf{m}_t$ and $\Delta\gamma_{j+1}$

   $\kappa_{j+1} = \kappa_0 + \Delta\gamma_{j+1}$,

   compute the algorithmic stiffness operator $\mathbf{A}$

   update the trial stress update according to Equation 4.38

   else

   elastic state:

   $\mathbf{m}_t = \mathbf{0}$

   $\boldsymbol{\sigma}_{j+1} = \boldsymbol{\sigma}_t$

   $\mathbf{A} = \mathbf{D}^e$

5. Check the global convergence criterion. If not converged, go to 1.

$(\bullet)_0$ denotes value at previous converged load step and $(\bullet)_j$ indicates value at previous iteration.

Box 4.1. Algorithm for implicit gradient plasticity formulations (iteration $j+1$)

4.5 Interpolation requirements

Taking the order of interpolation for the nonlocal effective plastic strain measure to be an order lower than the displacement gives a balanced interpolation. It is useful to investigate the effect of the same orders of interpolation, because when using adaptive or hierarchical refinement, the same order of interpolation may be simpler to implement. Indeed, it has been argued that nonlocal gradient models are coupled problems and the interpolation orders of variables do not have to be balanced [129]. Finally, there are indications from calculations with the second-order explicit gradient plasticity model that stress oscillations can occur in spite of the use of different interpolation orders for the displacements and the plastic multiplier [105].

We consider a one-dimensional bar, which is fixed at one end and subjected to tension at the other end, see Figure 4.4. The bar has a length $L = 100\ \mathrm{mm}$, a Young's modulus $E = 20000\ \mathrm{N/mm^2}$, area $= 100\ \mathrm{mm^2}$ and an initial tensile strength $\sigma_{y,0} = 2\ \mathrm{N/mm^2}$. The tensile strength in the central part of the bar ($21.875\mathrm{mm}$) is reduced by 5% to trigger localisation. A length scale $\ell = 5\ \mathrm{mm}$ is used and the bar is discretised with 64 and 128 elements, respectively. Only the second-order implicit gradient plasticity formulation is considered in this section.

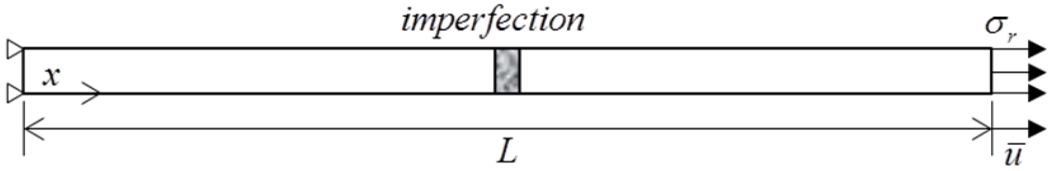

Figure 4.4: Tensile bar with imperfection

First, the effect of material parameters is studied for the tensile bar without imperfection. The load displacement curves are given in Figure 4.5 considering a linear damage evolution, Equation (4.8), with $H = 6000\ \mathrm{N/mm^2}$ and $\bar{\kappa}_i = 0$, and for an exponential damage evolution, Equation (4.53), with $H = 6000\ \mathrm{N/mm^2}$. The critical nonlocal effective plastic strain at full damage $\bar{\kappa}_u$ shows a significant influence on the linear relation, while β is the dominating parameter when using the exponential relation, cf. [45].

All subsequent simulations are for the tensile bar with an imperfection. The load-displacement curves are shown in Figure 4.6 for a quadratic interpolation of the nonlocal plastic multiplier and a cubic interpolation of the displacement. The parameters $H = 2000\ \mathrm{N/mm^2}$, $\bar{\kappa}_i = 0$ and $\bar{\kappa}_u = 0.001$ are used for linear damage evolution, while $H = 9000\ \mathrm{N/mm^2}$ and $\beta = 4300$ are adopted for exponential damage evolution. It is clear that mesh-objective results are obtained, since the curves are identical for both discretisations (64 and 128 elements). The evolution of nonlocal effective plastic strain has been plotted in Figure 4.7. The load-displacement curves as well as the nonlocal effective plastic strain profiles converge throughout the loading history. No visible mesh dependency exists.

Next, we consider the same interpolation order for the displacements and for the nonlocal effective plastic strain, using an exponential damage evolution. The load-displacement curves as well as the nonlocal strain profiles converge upon refinement of the discretisation. For 128 elements, the results are compared in Figure 4.8 for quadratic/quadratic, cubic/cubic and cubic/quadratic interpolations. There seems to be no visible differences among the results. The axial stress and the yield stresses are shown in Figures 4.9 and again, there seems to be no significant differences, which supports the assertion that gradient formulations are coupled problems and the interpolation functions of different variables that have to be discretised are not necessarily related [129]. Oscillations in the axial stress persist for all interpolations, which is ascribed to the weak satisfaction of the yield condition, similar to results obtained for the second-order explicit gradient plasticity model [105].

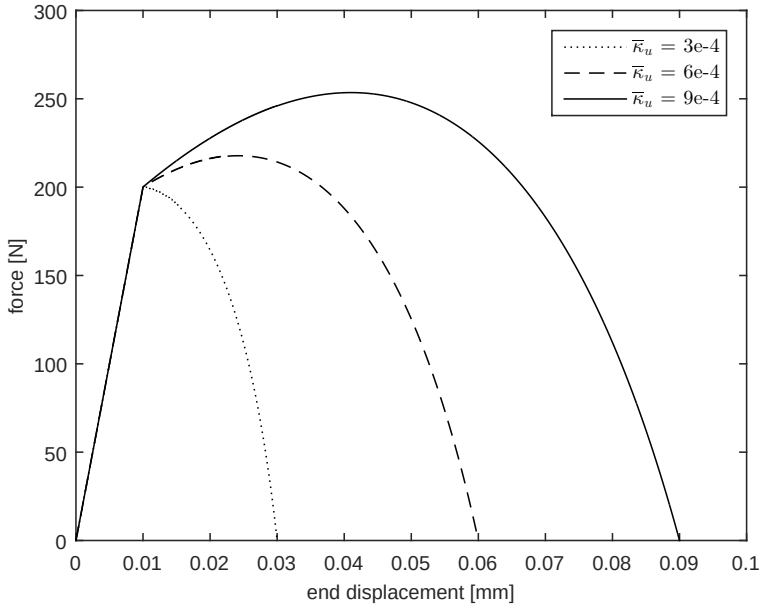

(a)

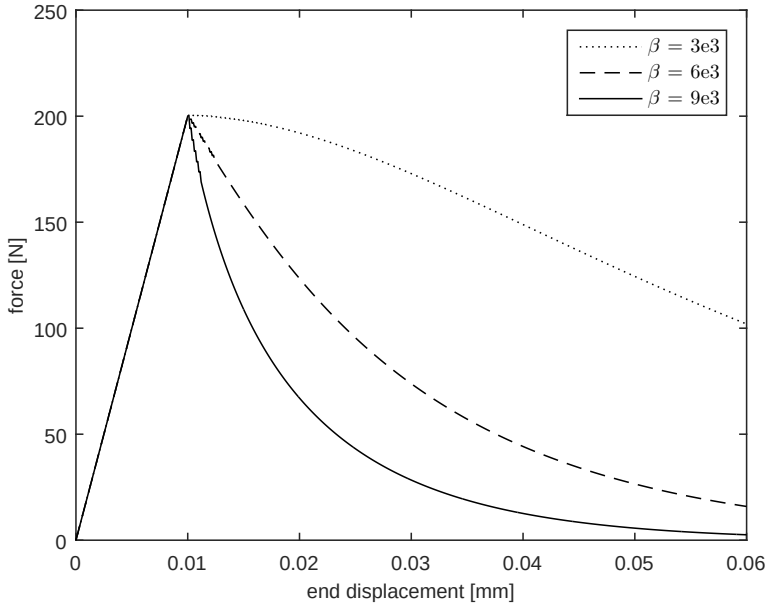

(b)

Figure 4.5: Influence of material parameters for bar without imperfection discretised with 64 elements using linear (a) and exponential (b) damage evolution law. Results are shown for an interpolation order $p = 2$ of the nonlocal plastic multiplier and $p = 3$ of the displacement.

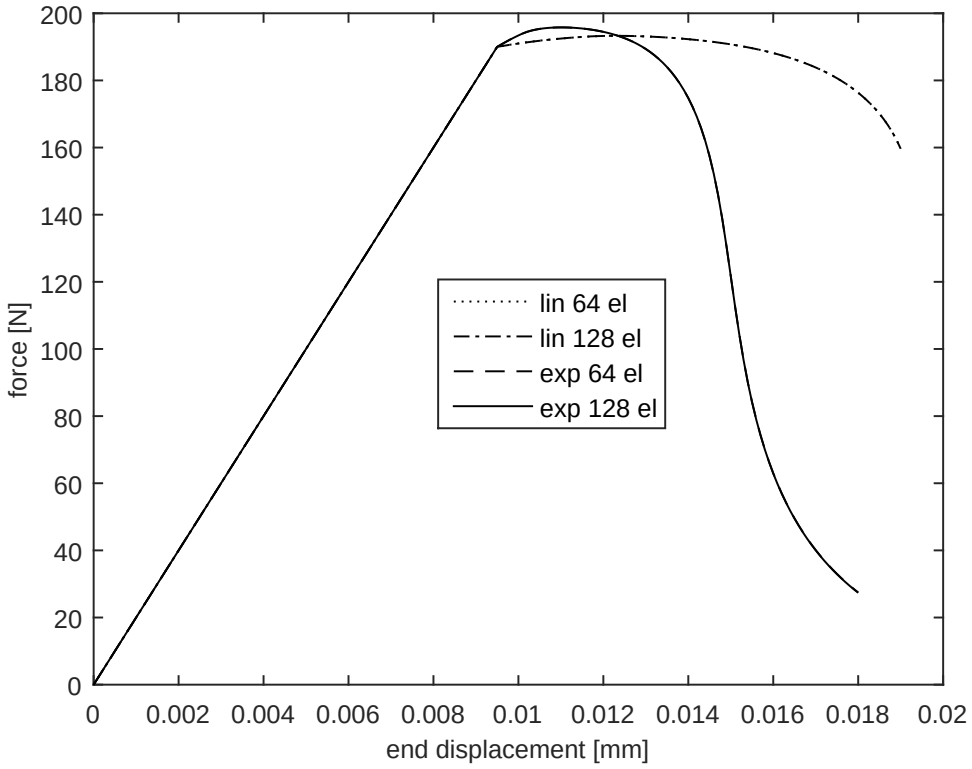

Figure 4.6: Load-displacement curves using an interpolation order $p = 2$ for the non-local plastic multiplier and $p = 3$ for the displacements. Results are shown for linear and exponential damage evolution relations, with 64 and 128 elements. The lines for the two meshes coincide and are thus indistinguishable.

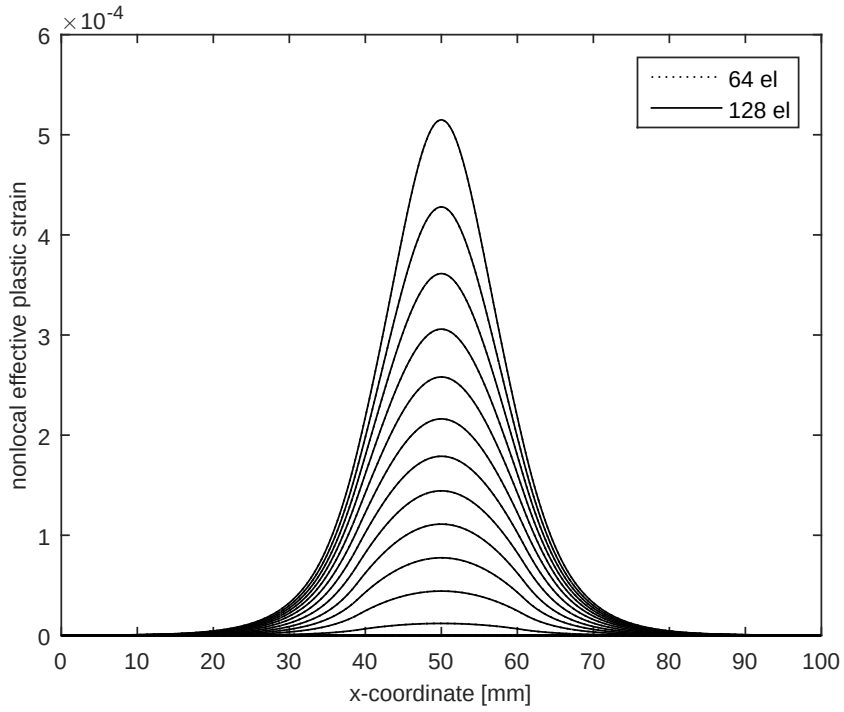

(a)

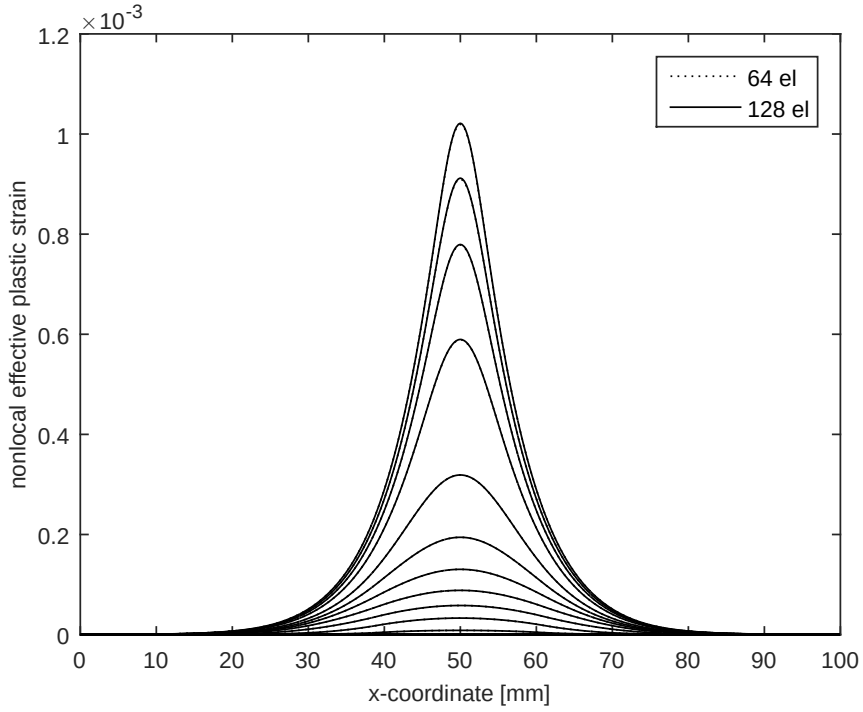

(b)

Figure 4.7: Evolution of the nonlocal effective plastic strain for linear (a) and exponential (b) damage evolution law with 64 and 128 elements. Results are shown for an interpolation order $p = 2$ of the nonlocal plastic multiplier and $p = 3$ of the displacement. The lines for the two meshes coincide and are thus indistinguishable.

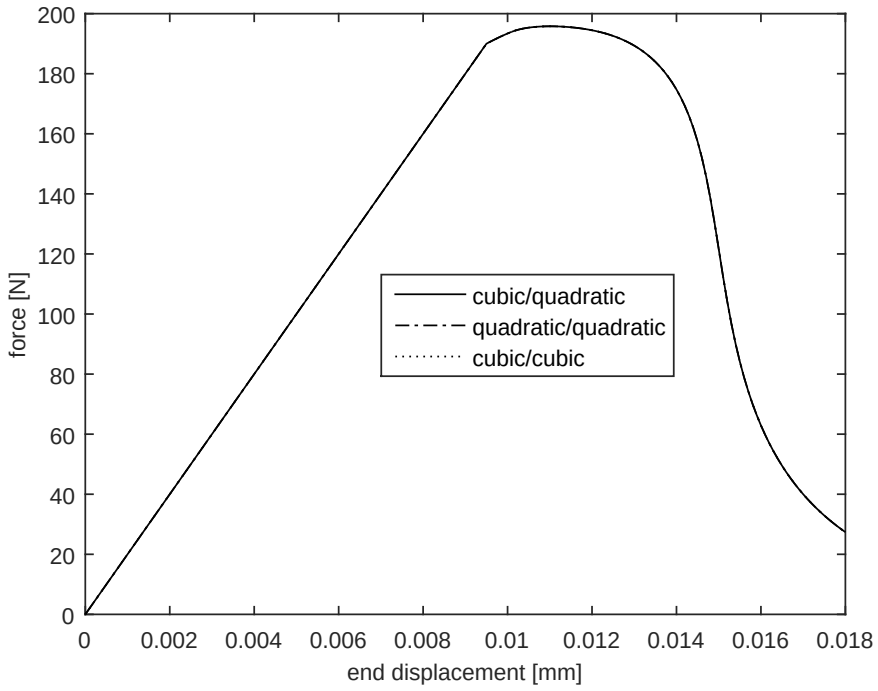

(a)

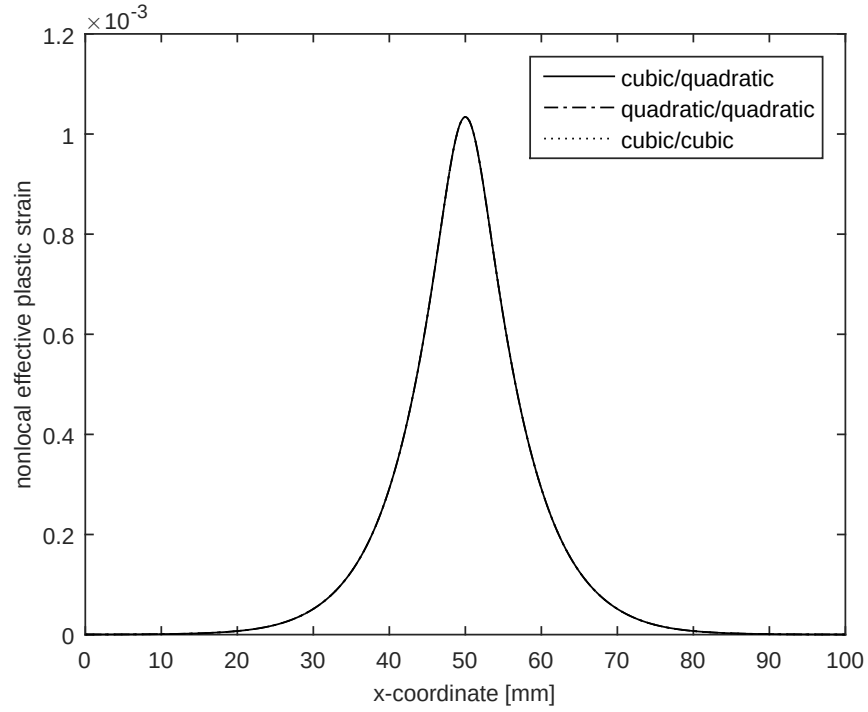

(b)

Figure 4.8: Load-displacement curves (a) and nonlocal effective plastic strain profiles (b) for different and same interpolation orders for the displacement/nonlocal effective plastic strain. Discretisation with 128 elements and an exponential damage evolution is adopted. The lines for all discretisations coincide and are thus indistinguishable.

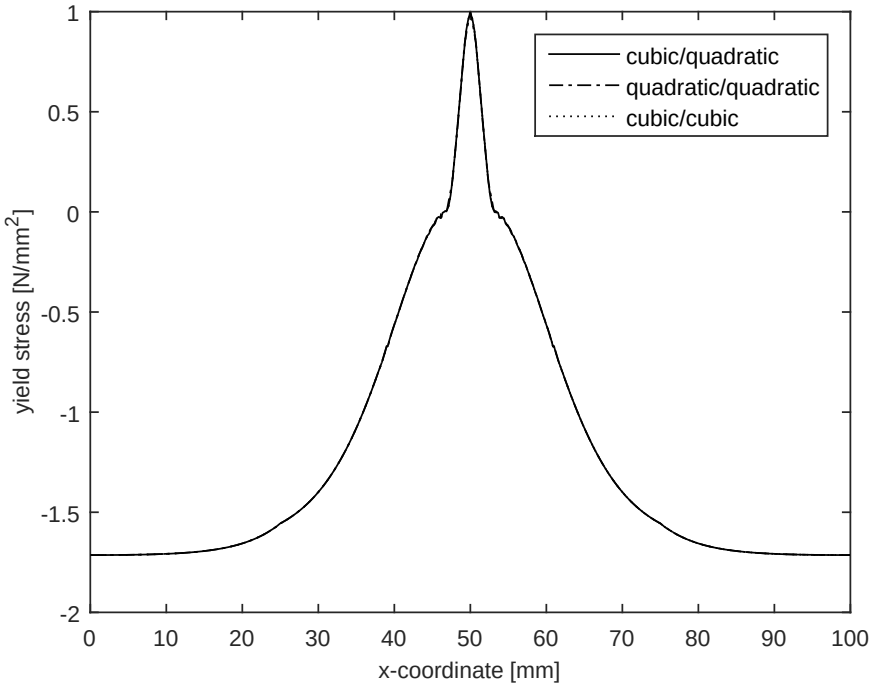

(a)

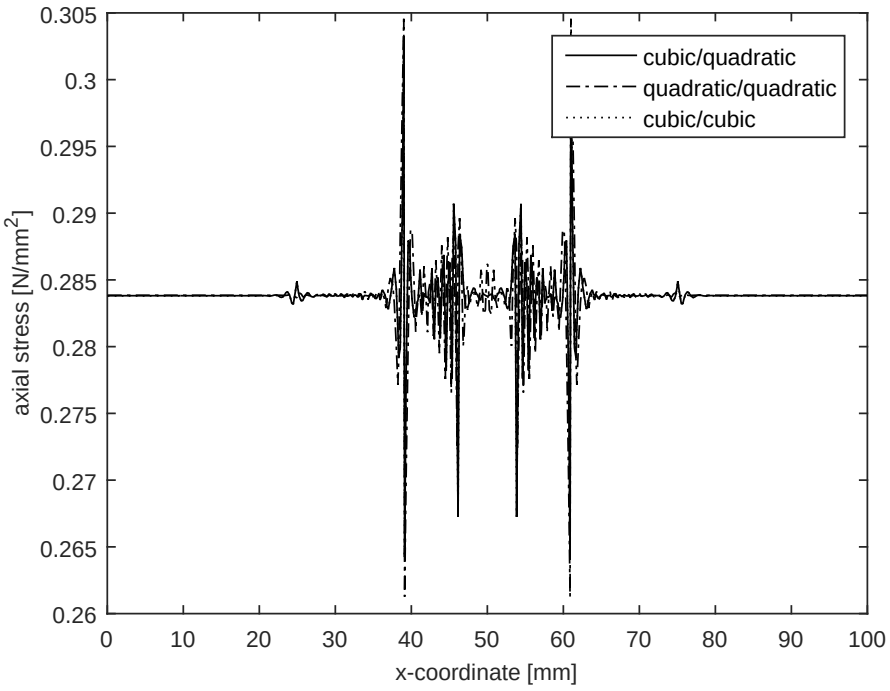

(b)

Figure 4.9: Yield stress (a) and axial stress (b) for different and same interpolation orders for the displacement/nonlocal effective plastic strain. Discretisation is with 128 elements and a exponential damage evolution is adopted. The lines for all discretisations nearly coincide and are thus indistinguishable.

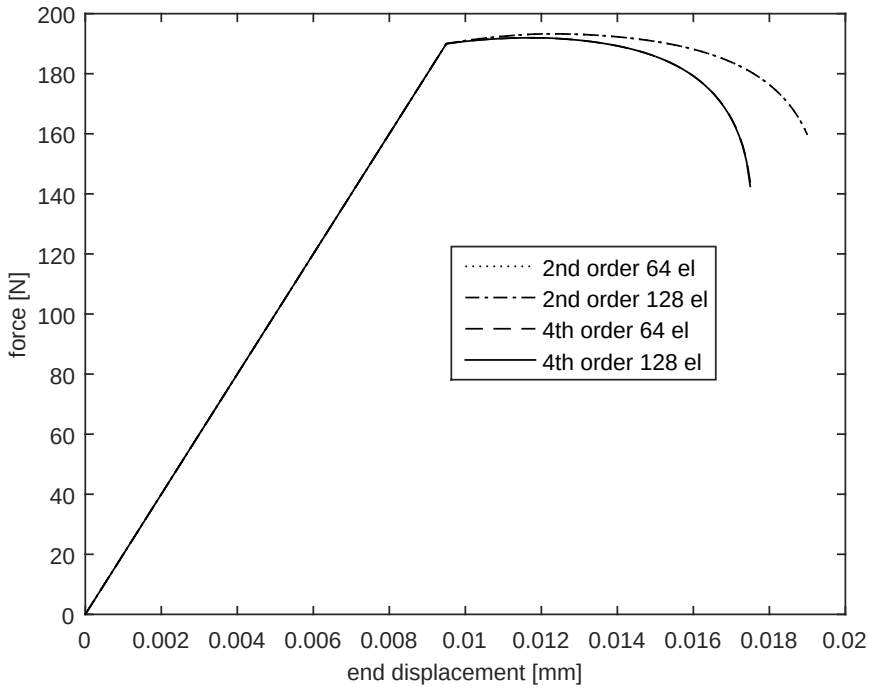

(a)

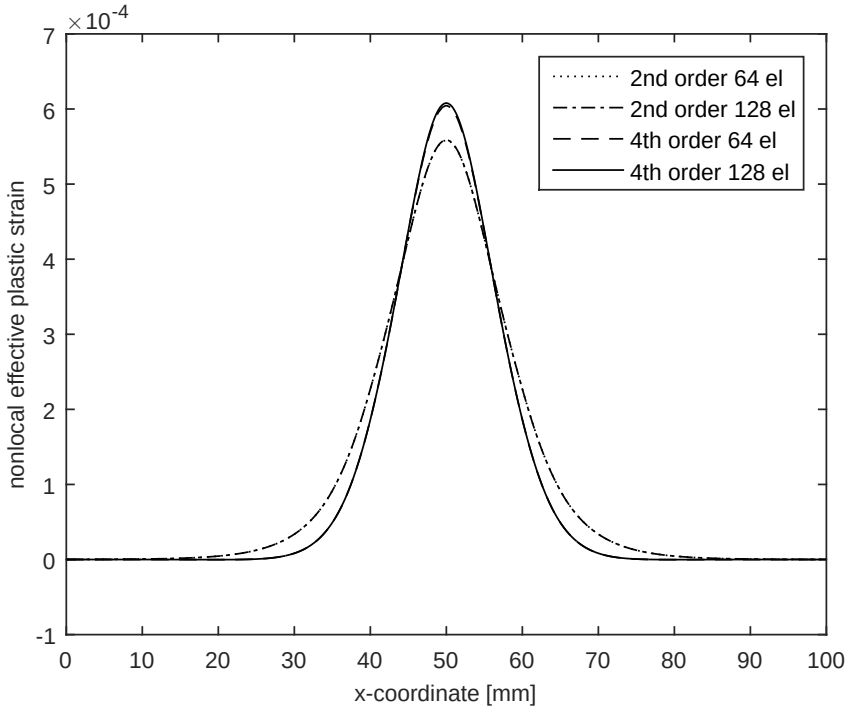

(b)

Figure 4.10: Tensile bar: Load-displacement curves (a) and nonlocal effective plastic strain profiles (b) for the second-order and fourth-order formulations discretised with different number of elements. The lines for the two meshes coincide and are thus indistinguishable.

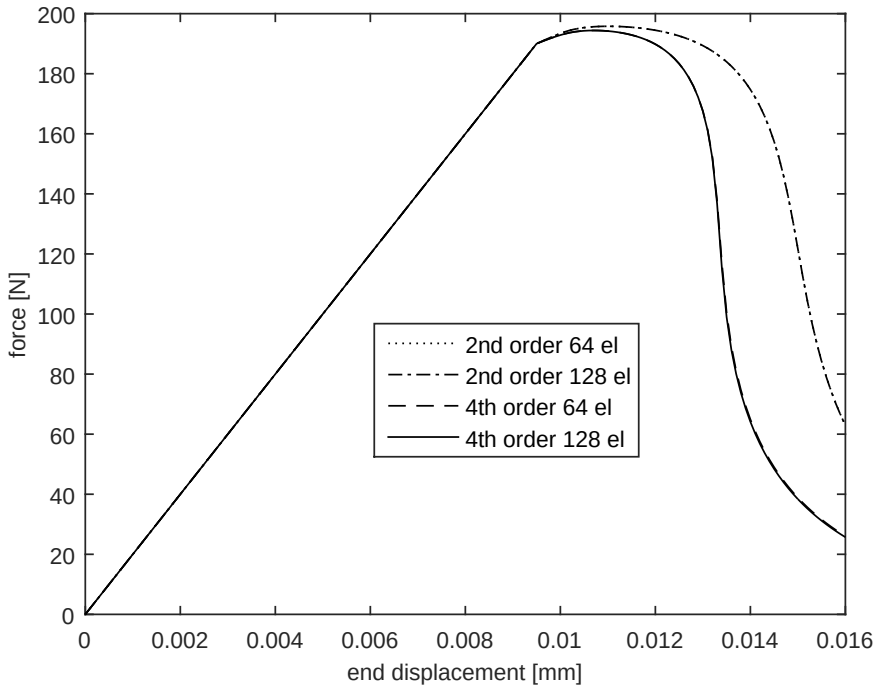

(a)

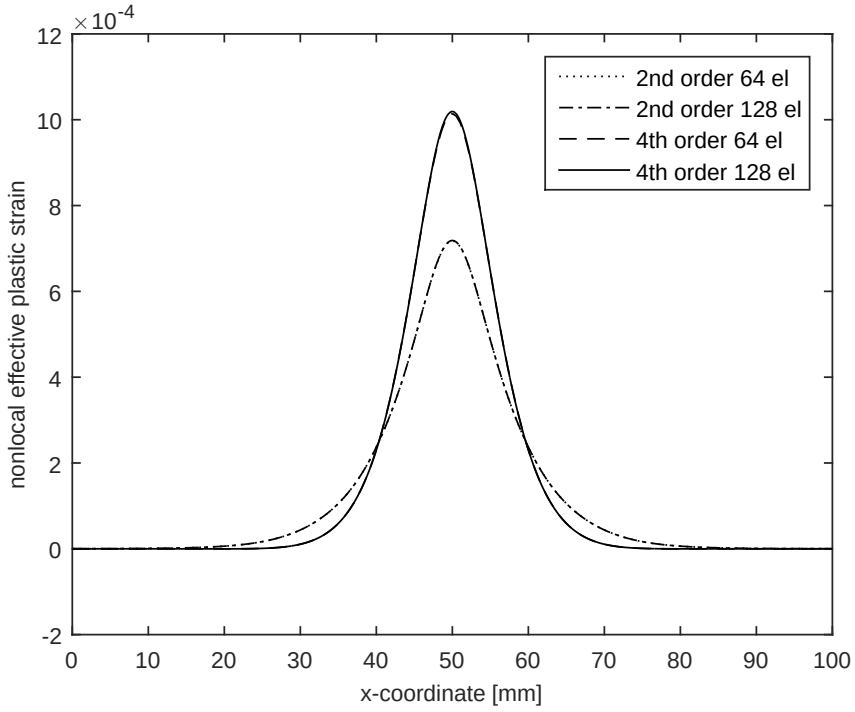

(b)

Figure 4.11: Tensile bar: Load-displacement curves (a) and nonlocal effective plastic strain profiles (b) for second-order and fourth-order gradient formulations discretised with different number of elements. An exponential damage evolution relation is adopted. The lines for the two meshes coincide and are thus indistinguishable.

4.6 Comparison of second-order and fourth-order gradient formulations

4.6.1 One-dimensional bar in tension

We revisit the problem of an imperfect bar subjected to tension discussed in the previous section (Figure 4.4). We now consider the second-order and the fourth-order implicit gradient plasticity formulations using a cubic interpolation for the displacements and a quadratic interpolation for the nonlocal effective plastic strain. We recall that for the second-order gradient formulation, $c_a = \ell^2$, $c_b = 0$, and that for the fourth-order formulation $c_a = \ell^2/2$, $c_b = \ell^4/8$. The load-displacement curves and nonlocal effective plastic strain profiles are shown in Figure 4.10 for a linear damage evolution.

Convergence is achieved in all cases, but significant differences occur between both formulations. The second-order implicit gradient formulation shows a more ductile response and a broader localisation band than the fourth-order formulation. This supports the results of the dispersion analysis, Figure 4.2, which point at a broader localisation band for the second-order formulation. The additional term due to the non-zero coefficient c_b in the fourth-order formulation leads to a higher peak of the nonlocal effective plastic strain in the fourth-order formulation, see Figure 4.10(b). The same trend is observed for the exponential damage evolution law, see Figure 4.11.

4.6.2 Square plate under uniaxial tension

Next, the two-dimensional panel is considered as shown in Figure 4.12. The left side is fixed in the x direction and the midpoint of this side is fixed in the y direction as well. A displacement $\bar{u}$ is imposed on the right side. Regarding the panel dimensions $L = 10$ mm, and the material properties are $E = 20000$ $\mathrm{N/mm^2}$, $H = 2000$ $\mathrm{N/mm^2}$, and $\sigma_{y,0} = 2$ $\mathrm{N/mm^2}$. An exponential damage evolution is assumed with $\beta = 3500$ and a length scale $\ell = 0.7$ mm. The yield strength is reduced by 5% at the bottom left corner of the panel to trigger localisation. Three uniformly refined meshes are considered with 256, 1,024 and 4,096 elements, respectively, see Figure 4.13, with a cubic interpolation for the displacements and a quadratic interpolation for the pressure.

The load-displacement curves are shown in Figure 4.14 for different meshes. The results show no mesh dependency indicating that regularisation is achieved. The con-

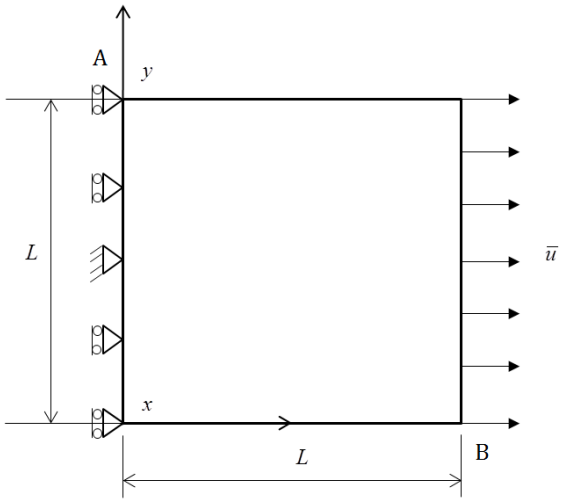

Figure 4.12: Geometry and boundary conditions of two-dimensional panel subjected to uniaxial tension

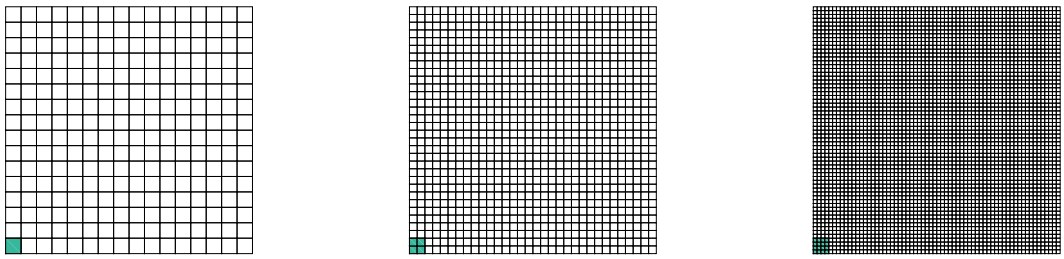

Figure 4.13: Meshes of square panel indicating weakened elements: (a) 256 elements; (b) 1,024 elements; (c) 4,096 elements

tours of the nonlocal effective plastic strain are given in Figure 4.15, while Figure 4.16 shows its distribution along the diagonal AB (Figure 4.12). The second-order formulation shows a wider localisation band. This is similar to the findings for implicit second-order and fourth-order gradient damage formulations [14]. Moreover, this corroborates the results of the dispersion analysis which indicate that the second-order formulation has a bigger band width. Conversely, for explicit gradient plasticity formulations, shear localisation analyses [91, 143] show a broader localisation band for an explicit fourth-order gradient model compared to an explicit gradient model with

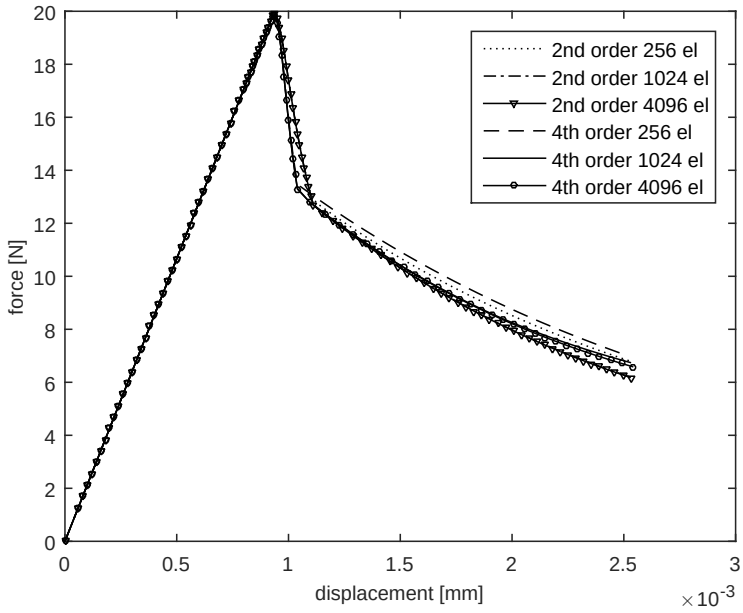

Figure 4.14: Load-displacement curves for square panel.

second-order gradients.

Figure 4.17 presents the evolution of the local and the nonlocal effective plastic strains. The second-order formulation with a mesh of 256 elements is employed. After localisation at $\bar{u} = 0.00096$ mm, further localisation within the band is observed in Figures 4.17(e) and 4.17(f). This is in agreement with results from standard finite element simulations [45].

Figures 4.15 and 4.17 indicate that the localisation zone first propagates along the vertical boundary before evolving into a shear band. This is consistent with earlier calculations for explicit and implicit gradient plasticity models using meshless methods [105] and isogeometric analysis [78] as shown in chapter 3. The results using standard finite elements are not presented very clearly [45]. This initial propagation along the vertical boundary can be due to the physical effect of damage since simulations using damage show the same trend [116]. More importantly, a study of non-local averaging models [130] has shown that due to the non-local averaging, a non-stationary shear-band evolves sometimes leading to incorrect or unrealistic failure patterns. It was also stated that such effect is not only valid for damage but for other dissipation mech-

anisms like plasticity. Further investigation into this is warranted. The angle of the shear band is lower than 45° which is the theoretical solution for a shear band when using a Tresca plasticity model. Unlike for the Tresca yield function, the intermediate principal stress enters the Von Mises yield condition, and this results in a different condition for the onset of localisation, including the angle of shear bands, cf. [122]. It is finally noted that the curving upward of the shear band near the free boundary is related to the emergence of stationary Rayleigh waves [99], and has been observed in other simulations as well [38].

4.6.3 Biaxially compressed specimen

To further assess the capability of the model, a biaxially compressed plane-strain specimen is considered, Figure 4.18, cf. [36, 45]. The width $L = 10\ \mathrm{mm}$. All material parameters are as in the previous section except that now $\beta = 2500$ and $\nu = 0.3$. The elements with reduced yield strength (by 5%) are shown in Figure 4.19.

The load-displacement curves are shown in Figure 4.20. It is noted that for the second-order formulation, the load-displacement curve (after the cusp) has not fully converged with 200 elements. This is because the smallest element size ($1\ \mathrm{mm}$) is larger than the length scale considered [78]. However, the fourth-order formulation shows convergence, which may suggest a stronger regularisation property for the fourth-order formulation. The nonlocal effective plastic strains are plotted in Figure 4.21. No mesh dependency is observed.

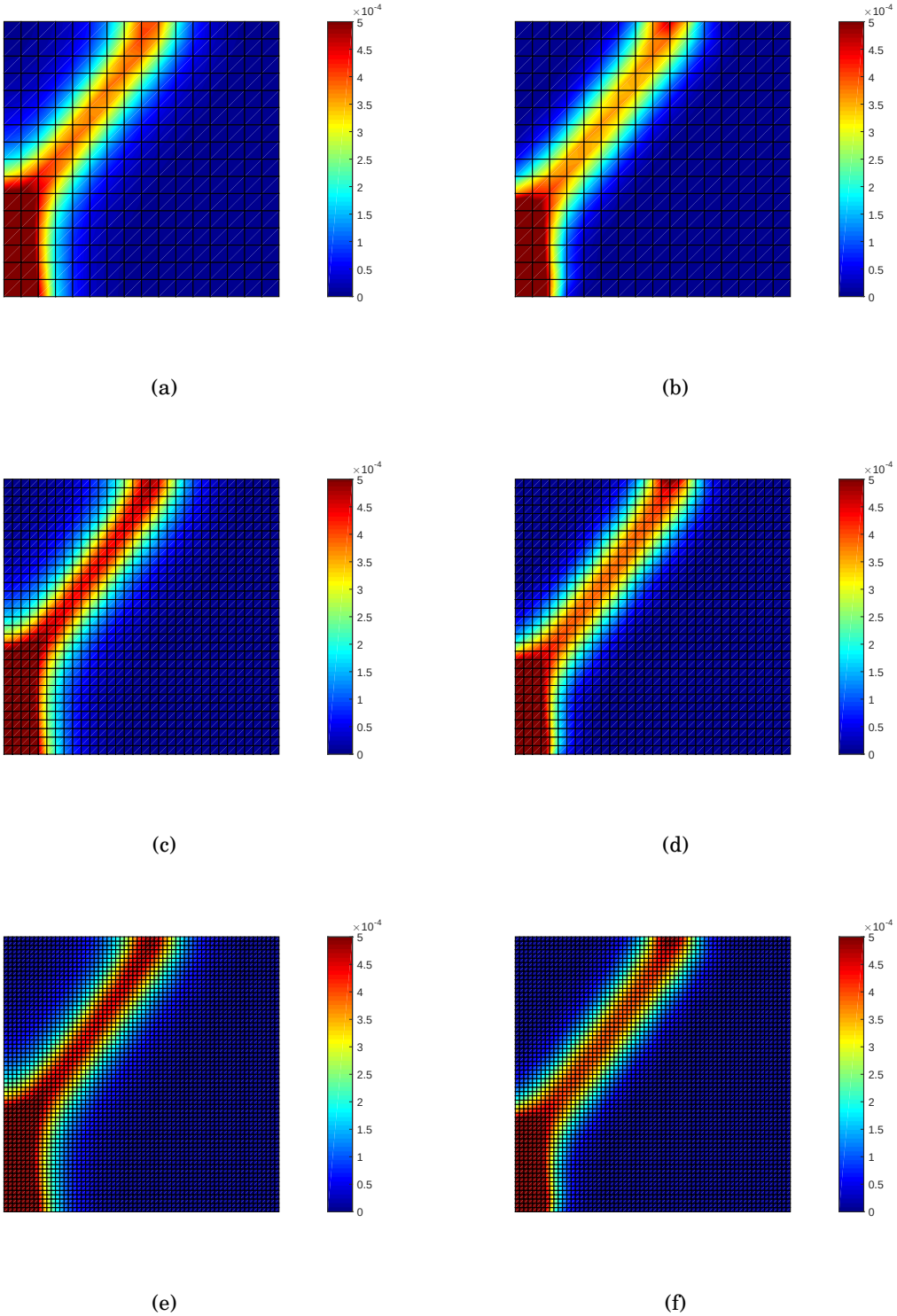

Figure 4.15: Square panel: Distribution of nonlocal effective plastic strain for the second-order (*left*) and fourth-order (*right*) formulations

.

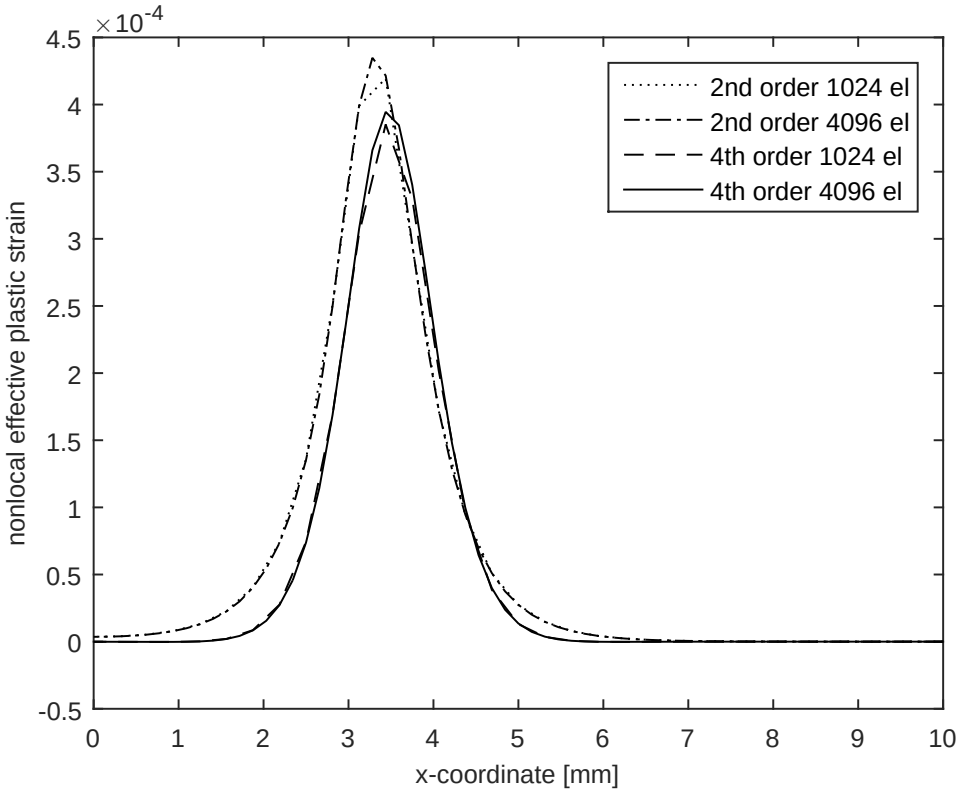

Figure 4.16: Distribution of nonlocal effective plastic strain along the diagonal AB, cf. Figure 4.12

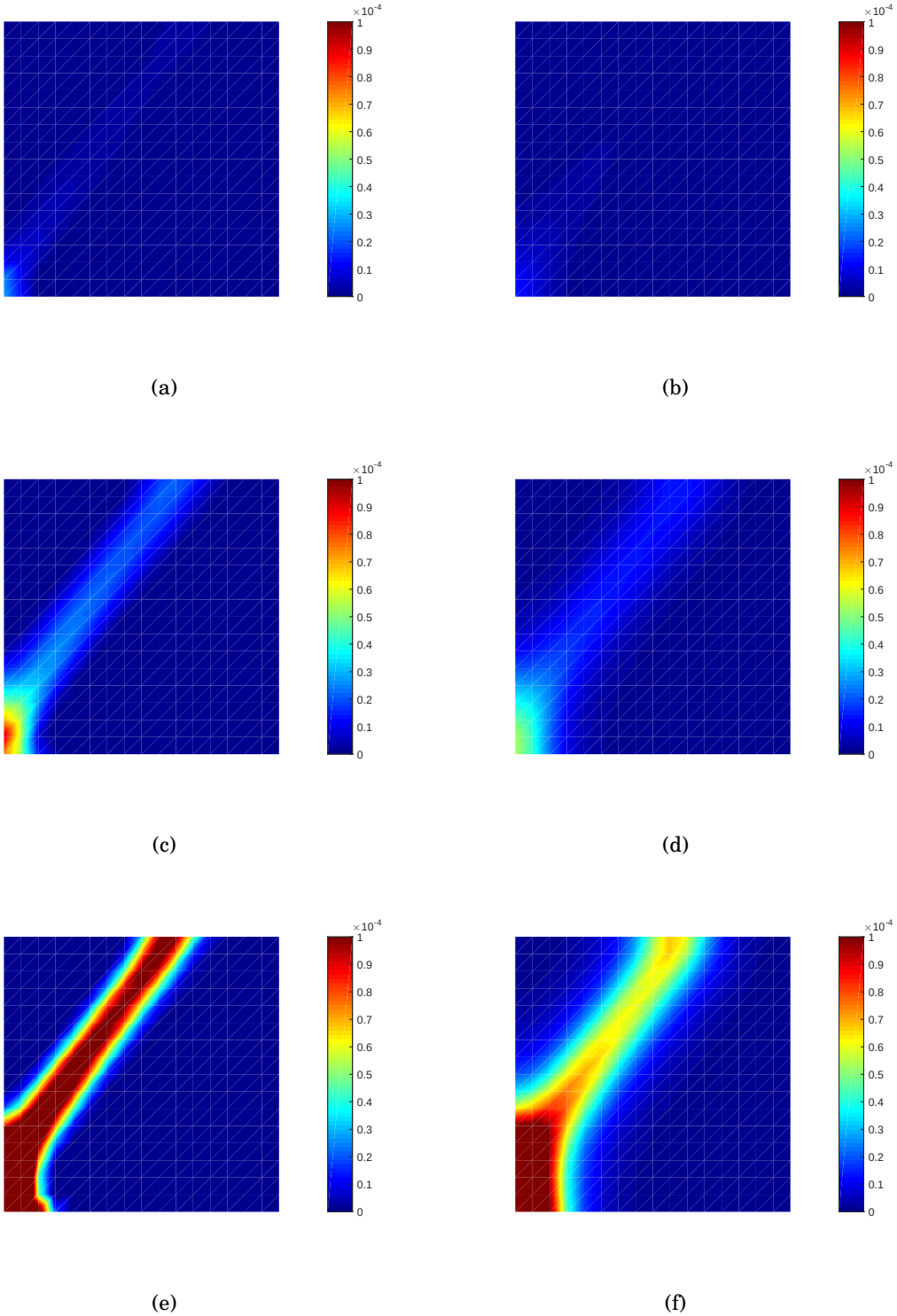

Figure 4.17: Evolution of the local (*left*) and the nonlocal (*right*) effective plastic strain at maximum displacement: $\bar{u} = 0.00093$ mm – (a), (b); $\bar{u} = 0.00096$ mm – (c), (d); $\bar{u} = 0.001$ mm – (e), (f)

.

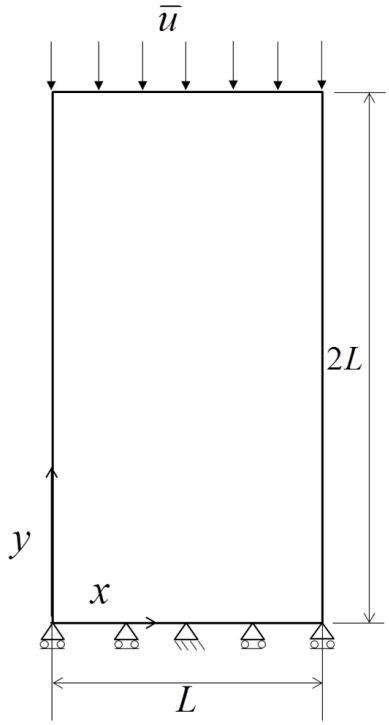

Figure 4.18: Biaxially compressed specimen: Geometry and boundary.

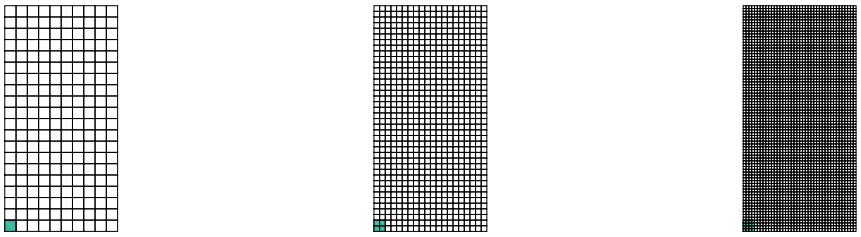

(a) (b) (c)

Figure 4.19: Mesh sizes and weakened elements for biaxially compressed specimen: (a) 200 elements; (b) 800 elements; (c) 3200 elements

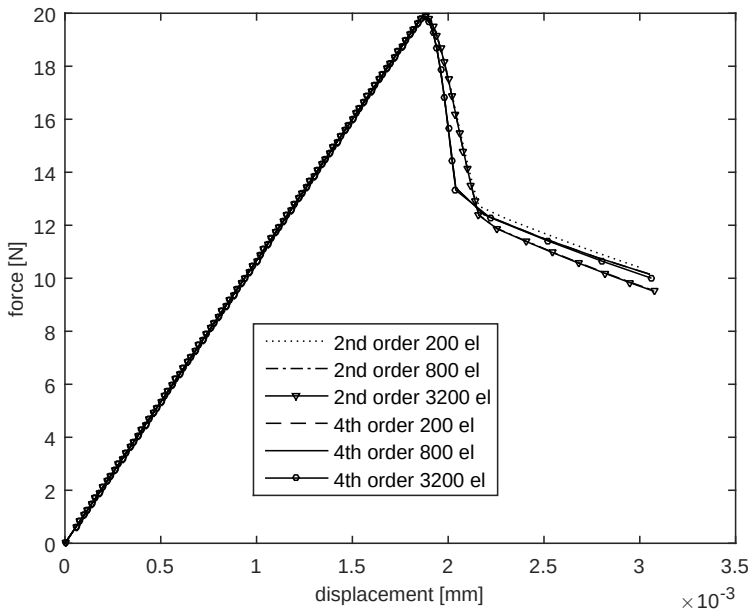

Figure 4.20: Load-displacement curves for biaxial compression test.

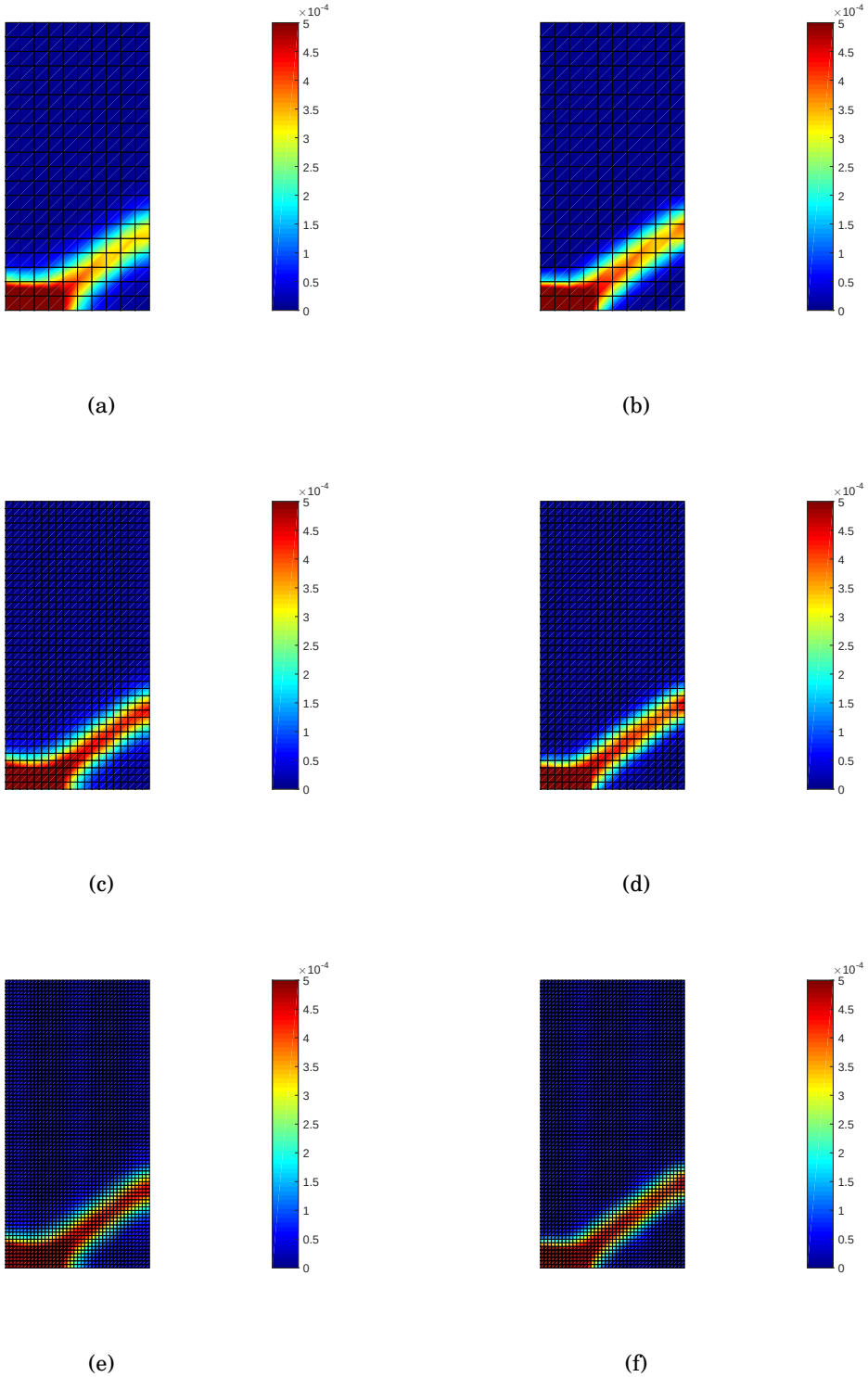

Figure 4.21: Biaxial compression: Distribution of nonlocal effective plastic strain for the second-order (*left*) and fourth-order (*right*) formulations.

.

4.7 Concluding remarks

The introduction of strain softening in plasticity models leads to a loss of well-posedness of the boundary value problem. Various approaches to regularise the problem exist, such as the use of nonlocal models, either in an integral sense by spatial averaging, or in a differential sense, by including higher-order spatial gradients of a history variable. It is now well established that both approaches are closely related [113].

Computationally, the addition of gradients is preferred, since in this approach a sparse, banded stiffness matrix is preserved, and it is possible to retain symmetry of the tangential stiffness matrix, which is different from nonlocal integral approaches [115]. Explicit second-order gradient plasticity models properly regularise the boundary value problem, as has been shown by dispersion analyses, and one-dimensional and two-dimensional finite element analyses of localisation. However, in explicit gradient plasticity the interpolation of the plastic multiplier must satisfy $\mathcal{C}^1$-continuity, since this is a necessary condition at the moving, internal elasto-plastic boundary [35]. This degree of continuity is difficult to satisfy using finite element approaches, and alternative formulations have been put forward [36, 78, 105].

The use of a second-order implicit gradient plasticity model, in which the nonlocal plastic strain is interpolated [45], is an alternative way to solve this issue since a $\mathcal{C}^0$-continuous interpolation for the nonlocal plastic equivalent strain suffices. However, it does not rigorously regularise the boundary value problem [117]. In this chapter we have explored the use of a fourth-order implicit gradient plasticity model. A dispersion analysis and one-dimensional and two-dimensional numerical analyses show that a regularisation, with mesh-independent results, can be obtained. Unfortunately, as with the explicit second-order gradient plasticity model, this requires a $\mathcal{C}^1$-continuous interpolation, now for the nonlocal plastic strain. Herein, it has been proposed to exploit isogeometric finite element analysis to meet this requirement.

It depends on the chosen damage relation whether the width of the localisation band tends to zero, thus resulting in a sharp crack, but also in a local loss of ellipticity. This is not different from the situation for second-order implicit gradient plasticity, but marks a clear difference with that for the second-order explicit gradient-plasticity

model.

Finally, it is noted that for the present class of problems, an equal-order interpolation for both types of variables, displacements and (nonlocal) equivalent plastic strains, is sufficient, with the advantages that come when considering adaptive or hierarchical meshing. The implicit gradient plasticity formulation allows for a steeper load-displacement curve without losing convergence. This makes it more stable than the explicit gradient formulation. In the next chapter, the second-order implicit gradient plasticity formulation is adopted with an equal order of interpolation for both discretised variables.

Chapter 5

STRAIN-GRADIENT ELASTICITY AND GRADIENT-DEPENDENT PLASTICITY WITH HIERARCHICAL REFINEMENT OF NURBS[1]

5.1 Introduction

Isogeometric analysis has been proposed as a means to integrate engineering design and analysis [63]. Essentially, the spline-based basis functions used in design - such as the widely-used Non-Uniform Rational B-splines (NURBS) - are used in analysis as well. This eliminates geometrical approximation errors in converting a geometry to a standard finite element mesh based on Lagrange polynomial functions. Furthermore, NURBS have a natural higher-order character. This has motivated their use in higher-order gradient models where higher-order continuity is needed [50, 69, 74, 139]. In these models, a length scale is incorporated in order to capture size effects and/or maintain a mesh-objective solution after the onset of softening.

Incorporating a length scale makes gradient elasticity models capable of resolving stress singularities at crack tips [11]. In problems associated with softening such as gradient plasticity and damage, localisation of deformation can develop. To accurately capture localisation bands and geometrical singularities, and in areas with strong gradients, there is need for a finer mesh in certain regions of the geometry [39, 151]. However, NURBS have a tensor-product nature which makes this local refinement a non-trivial task. Truncated-Hierarchical B-Splines (THB) and NURBS have been developed to address this [55]. More recently, THB splines have been expressed in a convenient element-wise data structure via Beziér extraction, thereby eliminating the

[1]This is an article in preparation

need for explicit truncation of bases [29, 60].

Several works have addressed adaptive refinement of generalized or gradient continua in the standard finite element context including the associated transfer of variables, e.g. [65, 68, 70, 104, 114]. In the context of hierarchical NURBS, Hennig et al. [59] explored various transfer operators and applied them to both linear and nonlinear problems. However, adaptive refinement of gradient-plasticity using hierarchical NURBS still remains to be addressed. If strain-gradient continua are to be widely adopted for analyses, the use of adaptive refinement techniques is a *conditio sine qua non*. Herein, strain-gradient models, gradient elasticity and gradient plasticity specifically, are explored using adaptive meshing techniques to efficiently capture failure and/or geometrical singularities.

We start by giving an overview of the gradient formulations considered in this chapter - Aifantis' gradient elasticity formulation [2, 6] and the implicit gradient plasticity formulation [45]. The weak forms and discretisation in the isogeometric analysis context are outlined next. The next section highlights hierarchical basis functions and their implementation via inter-level subdivision operators. Section 5.5 discusses the adaptive hierarchical refinement procedure including element marking and the transfer of variables between levels. We proceed with a section on numerical examples. First, for gradient elasticity and classical plasticity, for which exact solutions exist, and then gradient plasticity. The energy norm of the error is used in the former case, while a largely heuristic marking strategy is used for the latter. A concluding section ends the chapter.

5.2 Strain-gradient formulations

5.2.1 Aifantis' gradient elasticity

The gradient elasticity theory of Aifantis [2, 6] is considered here. In this theory, the Laplacian of the strain is introduced into the classical linear elastic constitutive relations as follows:

$$\boldsymbol{\sigma} = \mathbf{D}^e(\boldsymbol{\varepsilon} - \ell^2\nabla^2\boldsymbol{\varepsilon}) \tag{5.1}$$

where $\boldsymbol{\sigma} = [\sigma_{xx}, \sigma_{yy}, \sigma_{zz}, \sigma_{xy}, \sigma_{yz}, \sigma_{zx}]^{\mathrm{T}}$ is the stress vector, ℓ is a length scale parameter, $\boldsymbol{\varepsilon} = [\varepsilon_{xx}, \varepsilon_{yy}, \varepsilon_{zz}, \tau_{xy}, \tau_{yz}, \tau_{zx}]^{\mathrm{T}}$ is the strain vector, and $\mathbf{D}^e$ is the material elastic stiffness matrix given by

$$\mathbf{D}^e = \begin{bmatrix} \lambda+2\mu & \lambda & \lambda & 0 & 0 & 0 \\ \lambda & \lambda+2\mu & \lambda & 0 & 0 & 0 \\ \lambda & \lambda & \lambda+2\mu & 0 & 0 & 0 \\ 0 & 0 & 0 & \mu & 0 & 0 \\ 0 & 0 & 0 & 0 & \mu & 0 \\ 0 & 0 & 0 & 0 & 0 & \mu \end{bmatrix}. \tag{5.2}$$

for an isotropic linear elastic material where λ and μ are the Lamé constants. The accompanying equilibrium equations are:

$$\mathbf{L}^T\boldsymbol{\sigma} = \mathbf{0} \tag{5.3}$$

where body forces have been neglected and $\mathbf{L}$ is the differential operator:

$$\mathbf{L} = \begin{bmatrix} \frac{\partial}{\partial x} & 0 & 0 & \frac{\partial}{\partial y} & \frac{\partial}{\partial z} & 0 \\ 0 & \frac{\partial}{\partial y} & 0 & \frac{\partial}{\partial x} & 0 & \frac{\partial}{\partial z} \\ 0 & 0 & \frac{\partial}{\partial z} & 0 & \frac{\partial}{\partial x} & \frac{\partial}{\partial y} \end{bmatrix}^{\mathrm{T}}. \tag{5.4}$$

Substituting the stress-strain relation, eq.(5.1), and assuming small displacement gradients,

$$\boldsymbol{\varepsilon} = \mathbf{L}\mathbf{u}, \tag{5.5}$$

the following fourth-order partial differential equation results:

$$\mathbf{L}^T\mathbf{D}^e\mathbf{L}(\mathbf{u} - \ell^2\nabla^2\mathbf{u}) = \mathbf{0} \tag{5.6}$$

where $\mathbf{u} = [u_x, u_y, u_z]^{\mathrm{T}}$ is the displacement vector and $\nabla^2 \equiv \nabla^T \cdot \nabla$ is the Laplacian operator with $\nabla = [\frac{\partial}{\partial x}, \frac{\partial}{\partial y}, \frac{\partial}{\partial z}]^T$.

5.2.2 Implicit gradient plasticity

We adopt the implicit gradient plasticity formulation [45]. As in the previous section, limiting our scope to small deformations with no body forces, the problem is defined by the equilibrium equation:

$$\mathbf{L}^{\mathrm{T}}\boldsymbol{\sigma} = \mathbf{0} \tag{5.7}$$

the kinematic relation

$$\boldsymbol{\varepsilon} = \mathbf{L}\mathbf{u} \tag{5.8}$$

and the following incremental constitutive equations

$$\mathrm{d}\boldsymbol{\sigma} = \mathbf{D}^e(\, \mathrm{d}\boldsymbol{\varepsilon} - \mathrm{d}\boldsymbol{\varepsilon}^p) \tag{5.9}$$

$$\mathrm{d}\boldsymbol{\varepsilon}^p = \mathrm{d}\lambda \mathbf{m}, \quad \mathbf{m} = \frac{\partial F}{\partial \boldsymbol{\sigma}} \tag{5.10}$$

where an associated plasticity flow rule has been adopted for the yield function F. In equations (5.7)-(5.10), $\boldsymbol{\sigma}$, $\boldsymbol{\varepsilon}$, $\mathbf{u}$, $\mathbf{D}^e$ and $\mathbf{L}$ are as defined for gradient elasticity, $\mathrm{d}\boldsymbol{\varepsilon}^p$ is the plastic strain increment vector, $\mathrm{d}\lambda$ is a non-negative plastic multiplier, and $\mathbf{m}$ is a vector that defines the direction of plastic flow relative to F. The yield function F is given by [45]:

$$F(\boldsymbol{\sigma}, \kappa, \bar{\kappa}) = \sigma_e(\boldsymbol{\sigma}) - (1 - \omega(\bar{\kappa}))\, \sigma_y(\kappa) \tag{5.11}$$

$$\sigma_y = \sigma_{y,0} + H\kappa \tag{5.12}$$

$$\omega(\bar{\kappa}) = 1 - e^{-\beta\bar{\kappa}} \tag{5.13}$$

$$\mathrm{d}\kappa = \mathrm{d}\lambda \tag{5.14}$$

subject to the constraints

$$\mathrm{d}\lambda \geq 0, \quad F \leq 0, \quad F\mathrm{d}\lambda = 0 \tag{5.15}$$

where $\sigma_e(\boldsymbol{\sigma})$ is the Von Mises equivalent stress, κ is the local effective plastic strain measure or hardening parameter, $\bar{\kappa}$ is the nonlocal effective plastic strain measure, σ_y is the yield or flow stress, $\sigma_{y,0}$ is the initial yield strength, $H > 0$ is the hardening modulus, $\omega \in [0, 1]$ is a nonlocal damage variable, and β is a material constant. The strain-hardening hypothesis has been adopted to obtain a relation for the hardening parameter increment $\mathrm{d}\kappa$ in eq.(5.14).

The nonlocal effective plastic strain measure, $\bar{\kappa}(\mathbf{x})$, is defined as the volume average of the local effective plastic strain measure, $\kappa = \kappa(\boldsymbol{\varepsilon}^p)$. The ensuing formulation can be approximated as [45]:

$$\bar{\kappa}(\mathbf{x}) - \ell^2 \nabla^2 \bar{\kappa}(\mathbf{x}) = \kappa(\mathbf{x}) \tag{5.16}$$

where ℓ is the length scale that sets the averaging volume. The length scale, which can be correlated with micro-properties of a material, sets requirements on the mesh. In

localisation problems, the mesh size needs to be at least three times smaller than $2\pi\ell$ for sufficient accuracy to be achieved [35, 78, 115].

The strain-hardening hypothesis is assumed to also hold for $\bar{\kappa}$. For a state variable $\bar{\lambda}$ defined as

$$\bar{\lambda}(t) = \max\{\bar{\kappa}(\tau)|0 \leq \tau \leq t\} \tag{5.17}$$

the following constraints apply:

$$\mathrm{d}\bar{\lambda} \geq 0, \quad \bar{\kappa} - \bar{\lambda} \leq 0, \quad \mathrm{d}\bar{\lambda}\left[\bar{\kappa} - \bar{\lambda}\right] = 0 \tag{5.18}$$

Standard static and kinematic boundary conditions are adopted on the body surface S:

$$\boldsymbol{\Upsilon}\mathbf{n}_s = \mathbf{t}, \quad \mathbf{u} = \mathbf{u}_s \tag{5.19}$$

where $\boldsymbol{\Upsilon}$ is the stress tensor in matrix form, $\mathbf{n}_s$ is the outward normal to the surface S, and $\mathbf{t}$ is the boundary traction vector. Natural boundary conditions are assumed to apply on the derivative of $\bar{\kappa}$ [14]:

$$(\mathbf{n}_s^{\mathrm{T}}\nabla)\bar{\kappa} = 0. \tag{5.20}$$

Eq.(5.16) has to be satisfied in addition to the equilibrium equation, and thus, two equations have to be discretised and solved at each load step.

To update the stress, the trial yield function is evaluated at every iteration $j+1$ using [45]:

$$F_t = F(\boldsymbol{\sigma}_t, \kappa_0, \bar{\kappa}_{j+1}) = \sigma_{e,t} - \sigma_{y,0}\big(1 - \omega_{j+1}\big) \tag{5.21}$$

where $\sigma_{e,t} = \sigma_e(\boldsymbol{\sigma}_t)$ is the Von Mises equivalent stress evaluated with the trial stress, $\boldsymbol{\sigma}_t$:

$$\boldsymbol{\sigma}_t = \boldsymbol{\sigma}_0 + \mathbf{D}^e\Delta\boldsymbol{\varepsilon}_{j+1}. \tag{5.22}$$

and $(\bullet)_0$ indicates value at previous converged load step. When $F_t \leq 0$, there is an elastic state and the stress is simply updated as $\boldsymbol{\sigma}_{j+1} = \boldsymbol{\sigma}_t$. When $F_t > 0$, the state is plastic and is updated using [35, 117]:

$$\boldsymbol{\sigma}_{j+1} = \boldsymbol{\sigma}_t - \Delta\gamma_{j+1}\mathbf{D}^e\mathbf{m}_t \tag{5.23}$$

where $\mathbf{m}_t$ is given by Equation $(5.10)_2$, and $\Delta\gamma_{j+1}$ is the amount of plastic strain for the current iteration, given by [45],

$$\Delta\gamma_{j+1} = \frac{F_t}{H\left[1 - \omega_{j+1}\right]\left[\frac{\partial\kappa}{\partial\bar{\lambda}}\right] + \frac{3E}{2(1+\nu)}} \tag{5.24}$$

in which E is the Young's modulus and ν is the Poisson ratio.

5.3 Isogeometric finite element discretisation

Refer to section 2.3 and section 4.4 for the weak forms and the spatial discretisations of the gradient elasticity and implicit gradient plasticity formulations respectively.

5.4 Hierarchical refinement of NURBS

In hierarchical refinement, a multi-level mesh is used after determining the appropriate active elements across different hierarchical levels. Here, an element-wise approach conforming with the Beziér extraction framework is adopted.

5.4.1 Hierarchical bases

We consider a univariate B-spline in a parametric domain $\mathbf{\Omega}_d$ with knot vector $\mathbf{\Xi}$ and polynomial degree p. A hierarchy of P levels is constructed by successive uniform knot insertions from an initial knot vector $\mathbf{\Xi}^0$ until $\mathbf{\Xi}^{P-1}$ within $\mathbf{\Omega}_d$. Hence, nested parametric domains $\mathbf{\Omega}_d^i \subset \mathbf{\Omega}_d^{i+1}$ and nested knot vectors $\mathbf{\Xi}^i \subset \mathbf{\Xi}^{i+1}$ arise. The NURBS basis functions $\mathbf{N}^i = \left\{N_j^i\right\}_{j=1}^{n_i}$, defined by the knot vector of each level $\mathbf{\Xi}^i$ $(i = 0, 1, \ldots, P-1)$, form a nested approximation space $\mathcal{N}^i$. The basis function of each hierarchical level i can be expressed as a linear combination of each higher level j due to the nested nature of $\mathcal{N}^i$:

$$\mathbf{N}^i = \mathbf{S}^{i,j}\mathbf{N}^j = \prod_{l=i}^{j-1} \mathbf{S}^{L,L+1}\mathbf{N}^{L+1} \tag{5.25}$$

where $\mathbf{S}^{L,L+1}$ is the refinement or subdivision operator given by:

$$S_{IJ}^{L,L+1} = \frac{w_I^L}{w_J^{L+1}} M_{IJ}^{L,L+1} \tag{5.26}$$

in which $M_{IJ}^{L,L+1}$ is an entry in the linear subdivision operator for the B-spline shape functions between the hierarchical levels L and $L+1$. The B-spline shape functions of the hierarchical levels L and $L+1$ are defined by knot vectors $\mathbf{\Xi}^L$ and $\mathbf{\Xi}^{L+1}$ respectively, using a weight factor $w = 1$. w_I^L represents the weight factor of the Ith shape function on hierarchical level L.

The hierarchical basis function space $\mathcal{A}$ is defined as

$$\mathcal{A} = \bigcup_{L=0}^{P-1} \mathcal{A}_a^L \quad \text{with} \quad \mathcal{A}_a^L = \mathcal{A}^L \backslash \mathcal{A}_-^L \tag{5.27}$$

where "\" is the logic NOT and $\mathcal{A}_a^L$ are the active basis functions of hierarchical level L. $\mathcal{A}^L$ is the union of basis functions defined over the active elements on hierarchical level L. $\mathcal{A}_-^L$ denotes the shape functions in $\mathcal{A}^L$ with support over the active elements on coarser hierarchical levels. Another shape function variable $\mathcal{A}_+^L$ denotes those with support over active elements on finer hierarchical levels. Succinctly, we have the following set of basis functions:

$$\begin{aligned}
\mathcal{A}^L &= \left\{ N_j^L \in \mathcal{N}^L : \ \mathrm{sup} N_j^L \bigcap E_A^L \neq \emptyset \right\} \\
\mathcal{A}_+ &= \bigcup_{L=0}^{P-1} \mathcal{A}_+^L \quad \text{with} \quad \mathcal{A}_+^L = \left\{ N_j^L \in \mathcal{A}^L : \ \mathrm{sup} N_j^L \bigcap \mathbf{\Omega}_d^{L+} \neq \emptyset \right\} \\
\mathcal{A}_- &= \bigcup_{L=0}^{P-1} \mathcal{A}_-^L \quad \text{with} \quad \mathcal{A}_-^L = \left\{ N_j^L \in \mathcal{A}^L : \ \mathrm{sup} N_j^L \bigcap \mathbf{\Omega}_d^{L-} \neq \emptyset \right\}
\end{aligned} \tag{5.28}$$

where E_A^L is the parametric domain of all active elements on hierarchical level L and belongs to the parametric domain of active elements:

$$\mathbf{\Omega}_d = \bigcup_{L=0}^{P-1} E_A^L \quad \text{with} \quad E_A^L = \bigcup_e \mathbf{\Omega}_d^{e,L} \tag{5.29}$$

where $\mathbf{\Omega}_d^{e,L}$ represents the parametric domain of element e on hierarchical level L. The parametric domains $\mathbf{\Omega}_d^{L+}$ and $\mathbf{\Omega}_d^{L-}$ are expressed as:

$$\mathbf{\Omega}_d^{L+} = \bigcup_{i=L+1}^{P-1} E_A^i \qquad\qquad \mathbf{\Omega}_d^{L-} = \bigcup_{i=0}^{L-1} E_A^i \tag{5.30}$$

As stated earlier, cf. eq. (5.25), the basis functions at level L can be expressed as a linear combination of the bases at level $L+1$. When lower level bases are eliminated, the truncated hierarchical basis function space is obtained as:

$$\mathcal{A}_T = \bigcup_{L=0}^{P-1} \mathcal{A}_{T,a}^L \quad \text{with} \quad \mathcal{A}_{T,a}^L = \left\{ \tau_j^L \in \mathcal{A}_a^L : \ \sup \tau_i^L \not\subseteq E_A^{L+1} \right\} \tag{5.31}$$

where

$$\tau_i^L = \left\{ \tau_i^L \in \mathcal{N}^L : \ \tau_i^L = \sum S_{ij}^{L,L+1} N_j^{L+1} \right\} \tag{5.32}$$

Truncated hierarchical bases give a better conditioning of the system of equations and fulfill the partition of unity property [29, 60].

5.4.2 Multi-level implementation of hierarchical bases

Using Beziér extraction, the active elements are used in assembling the stiffness matrix for all levels which results in a global system of equations. In gradient elasticty for example, the resulting system of equations is:

$$\mathbf{K}\mathbf{b} = \mathbf{f} \tag{5.33}$$

where $\mathbf{K} = \mathbf{K}_1 + \mathbf{K}_2$, cf. eq. (2.26). b (which equals a for gradient elasticity) includes the degrees of freedom for control points from each hierarchical level and $\mathbf{K}$ is a sparse matrix with submatrices $\mathbf{K}^L$ corresponding to each hierarchical level L. Since only active elements are considered, $\mathbf{K}^L$ is very sparse.

It is noted that $\mathbf{K}$ does not incorporate the interaction between different hierarchical levels. This is incorporated through the hierarchical subdivision or refinement operator:

$$\mathbf{M}_h = \begin{bmatrix} \mathbf{I}^0 & \hat{\mathbf{M}}^{0,1} & \hat{\mathbf{M}}^{0,2} & \dots & \hat{\mathbf{M}}^{0,P-1} \\ & \mathbf{I}^1 & \hat{\mathbf{M}}^{1,2} & \dots & \hat{\mathbf{M}}^{1,P-1} \\ & & \mathbf{I}^2 & \dots & \hat{\mathbf{M}}^{2,P-1} \\ & & & \ddots & \\ \mathbf{0} & & & & \mathbf{I}^{P-1} \end{bmatrix} \tag{5.34}$$

where

$$I_{IJ}^L = \begin{cases} 1 & \text{for} \quad I = J \quad \text{and} \quad N_I^L \in \mathcal{A}_a^L \\ 0 & \text{else} \end{cases} \tag{5.35}$$

and the entries $\hat{\mathbf{M}}^{L,k}$ are defined as follows for truncated hierarchical basis functions:

$$\hat{\mathbf{M}}^{L,k} = \begin{cases} S_{IJ}^{L,k} & \text{for} \quad N_I^L \in \mathcal{A}_+^L \quad \text{and} \quad N_J^K \in \mathcal{A}_-^L \\ 0 & \text{else} \end{cases} \tag{5.36}$$

in which $S_{IJ}^{L,k}$ is given in eq.(5.26). When the hierarchical subdivision operator $\mathbf{M}_h$ is used, the system of equations becomes:

$$\mathbf{K}_h\, \mathbf{b}_h = \mathbf{f}_h \quad \text{where} \quad \mathbf{K}_h = \mathbf{M}_h\, \mathbf{K}\mathbf{M}_h^T, \;\; \mathbf{f}_h = \mathbf{M}_h\, \mathbf{f}. \tag{5.37}$$

It is also noted that in a non-linear iteration procedure - e.g. in gradient plasticity, $\mathbf{K}$ is computed using b (and not $\mathbf{b}_h$) from the previous iteration. It is retrieved by using

$$\mathbf{b} = \mathbf{M}_h^T \mathbf{b}_h. \tag{5.38}$$

5.5 Adaptive hierarchical refinement

To perform adaptive isogeometric analysis using NURBS, the following procedure is followed:

1. Solve the hierarchical system of equations $\mathbf{K}_h \mathbf{b}_h = \mathbf{f}_h$.
   - For gradient elasticity, $\mathbf{K}_h = f(\mathbf{K}_1, \mathbf{K}_2, \mathbf{M}_h)$, $\mathbf{b}_h = f(\mathbf{M}_h, \mathbf{a})$ and $\mathbf{f}_h = f(\mathbf{M}_h, \mathbf{f}^{ext})$
   - For gradient plasticity, $\mathbf{K}_h = f(\mathbf{K}_{aa}, \mathbf{K}_{a\lambda}, \mathbf{K}_{\lambda a}, \mathbf{K}_{\lambda\lambda}, \mathbf{M}_h)$, $\mathbf{b}_h = f(\mathbf{M}_h, \mathrm{d}\mathbf{a}, \mathrm{d}\bar{\mathbf{\Lambda}})$ and $\mathbf{f}_h = f(\mathbf{M}_h, \mathbf{f}_e, \mathbf{f}_a, \mathbf{f}_\lambda)$
2. Project the solution on all active basis functions using $\mathbf{b} = \mathbf{M}_h^T \mathbf{b}_h$
3. Estimate the approximation error in each element
   - For gradient elasticity, the relative energy norm is used
   - For gradient plasticity, a measure of the plastic strain and the length scale are used
4. Mark elements to be refined according to step 3.
5. If some elements are marked for refinement,
   - Refine the elements
   - Transfer the state variables (gradient elasticity) and the history variables (gradient plasticity) from the old mesh to the new mesh
   - Return to step 1
6. If no elements are marked, stop the procedure

Clearly, the following are required: (I) marking of elements - mainly based on an error estimation technique; (II) a refinement strategy, and (III) data transfer between two consecutive levels/meshes.

5.5.1 Element marking

For gradient elasticity, the element error is estimated using the relative energy norm. The relative energy norm for each element, e, is calculated using the error in energy norm $\|e\|$ and the energy norm $\|U\|$ as follows [28]:

$$\phi_e = \frac{\|e\|_e}{\|U\|_e} = \frac{\sqrt{\frac{1}{2}\int_{\Omega_e}(\hat{\boldsymbol{\sigma}} - \boldsymbol{\sigma})^T \cdot (\mathbf{D}^e)^{-1} \cdot (\hat{\boldsymbol{\sigma}} - \boldsymbol{\sigma}) dS}}{\sqrt{\frac{1}{2}\int_{\Omega_e}\hat{\boldsymbol{\sigma}} \cdot (\mathbf{D}^e)^{-1} \cdot \hat{\boldsymbol{\sigma}} dS}} \tag{5.39}$$

where $\hat{\boldsymbol{\sigma}}$ represents the analytical solution, $\boldsymbol{\sigma}$ represents the approximate solution and $\mathbf{D}^e$ is the material elastic stiffness matrix. Only two-dimensional plane-strain problems are considered in this work, so that:

$$\mathbf{D}^e = \frac{E}{(1+\nu)(1-2\nu)} \begin{bmatrix} 1-\nu & \nu & 0 \\ \nu & 1-\nu & 0 \\ 0 & 0 & \frac{1-2\nu}{2} \end{bmatrix} \tag{5.40}$$

In practice, an error estimator such as a residual-based error estimator can be used such that the exact solution is not necessarily required. However, an appropriate error estimator is beyond the scope of this thesis. Therefore error indicators which require an exact solution are employed here for the purpose of developing a working framework. The exact solution is used when available, otherwise, a sufficiently finer mesh is used as reference. The element-wise errors (ϕ_Q), where Q is an element in mesh Ω with N number of elements, are arranged in descending order – for $\Omega = \{Q_1, \cdots, Q_N\}$, $\phi_{Q_1} \geq \cdots \geq \phi_{Q_N}$. A marking parameter $\eta \in [0, 1]$ is defined such that k elements are marked for refinement:

$$\mathcal{M} = Q_1, \cdots, Q_k \quad \text{with} \quad k = \text{ceil}(\eta N) \tag{5.41}$$

where the 'ceil()' function rounds up to the nearest integer. This approach is also referred to as the quantile marking strategy. It should be noted that when an element is already at the highest hierarchical level, it is *not* marked for refinement. Also, to ensure that the stiffness matrix $\mathbf{K}_h$ has a good condition number, elements adjacent to the marked elements are forced to be from the same level, or at most, two hierarchy levels [28].

According to Perić et al. [114], the relative energy norm can be used with classical elastoplasticity, as well as generalised plasticity models. Hence, we also adopt the error in energy norm with quantile marking for classical plasticity.

As stated earlier, for localisation problems using gradient plasticity, the length scale ℓ should be larger than the mesh size such that two to four elements lie within the localisation band. If this is not the case, the model will not properly offer the needed regularisation. In the case of gradient plasticity, we use the following parameter:

$$d = \frac{h_e}{\ell} \tag{5.42}$$

where h_e is the size of element e. The lower the value of d, the more capable the mesh is to capture a localisation band.

5.5.2 Refinement strategy

Hierarchical refinement is performed based on the concept of active and inactive elements. Thus, all elements in different hierarchy levels exist *a priori* before computation, but, the relevant elements to be activated are chosen successively such that at each instant, the whole geometry is fully covered. To this end, two indicator arrays, each of the same size as the number of elements, are defined and initialised as false:

- $\mathbf{E}_a$ - indicator of active elements. E_a^i is true when element i is active
- $\mathbf{E}_{ac}$ - indicator of active child elements. E_{ac}^i is true when the child elements of element i are active

Based on these two arrays, the indicators for the total number of basis functions across all levels are defined. The basis functions are defined as $\mathbf{N} = \{N^i\}$, $i = 1, 2, \cdots, n_b$ where n_b is the total number of basis functions. The following Boolean arrays are defined and initialised as false, see section 5.4:

- $\mathbf{A}_a$ - indicator of basis function in the hierarchical basis function space $\mathcal{A}$ or $\mathcal{A}_T$, cf. eq. (5.27) and eq. (5.31). A_a^i is true when $N^i \in \mathcal{A}$ or $\mathcal{A}_T$
- $\mathbf{A}_{\_}$ - indicator of basis function in the hierarchical basis function space $\mathcal{A}_{\_}$, cf. eq. (5.28). $A_{\_}^i$ is true when $N^i \in \mathcal{A}-$

- $\mathbf{A}_+$ - indicator of basis function in the hierarchical basis function space $\mathcal{A}_+$, cf. eq. (5.28). A_+^i is true when $N^i \in \mathcal{A}+$

Let some elements E_r be elements marked for refinement and E_{rc} be all child elements of E_r. To obtain the new list of active elements and active child elements, the following procedure is followed:

- Obtain the old list of $\mathbf{E}_a$ and $\mathbf{E}_{ac}$
- Set $\mathbf{E}_a(E_r) = \textbf{false}$ and $\mathbf{E}_{ac}(E_r) = \textbf{true}$
- Set $\mathbf{E}_a(E_{rc}) = \textbf{true}$ and $\mathbf{E}_{ac}(E_{rc}) = \textbf{false}$

5.5.3 Transfer of state vector and history variables

When moving from a time step t to time step $t + \Delta t$ where some elements have been marked for refinement, the old state vector ${}^t\mathbf{b}$ needs to be mapped onto the new state ${}^{t+\Delta t}\mathbf{b}$. We call this mapping transfer operation $\mathcal{T}^0$. This is done in a straightforward manner, as follows:

$$ {}^{t+\Delta t}\mathbf{b}^{L+1} = (\tilde{\mathbf{S}}^{L,L+1})^T \, {}^t\mathbf{b}^L \tag{5.43} $$

in which L is the hierarchical level and $\tilde{\mathbf{S}}^{L,L+1}$ is the modified refinement operator:

$$ \tilde{S}_{IJ}^{L,L+1} = \begin{cases} S_{IJ}^{L,L+1} & \text{for} \quad N_J^{L+1} \in {}^{t+\Delta t}\mathcal{A}^{L+1} \text{ or } {}^{t+\Delta t}\mathcal{A}_T^{L+1} \\ 0 & \text{else} \end{cases} \tag{5.44} $$

where ${}^{t+\Delta t}\mathcal{A}^{L+1}$ and ${}^{t+\Delta t}\mathcal{A}_T^{L+1}$ are hierarchical basis function spaces at hierarchical level $L+1$ and time step $t + \Delta t$. The transfer of the state vector from the old control points to the new control points suffices for gradient elasticity.

In the case of gradient plasticity, there are also history variables at the old integration points which need to be transferred to the integration points of the new mesh. This is done in three mapping steps:

1. $\mathcal{T}^1$ - the history variables from the old integration points are extrapolated to the control points of the old mesh;

2. $\mathcal{T}^2$ - these control variables on the old mesh are mapped to the control points of the new mesh, and

3. $\mathcal{T}^3$ - the history data is interpolated from the control points of the new mesh to the integration points of the new mesh

To perform $\mathcal{T}^1$, a global least-squares projection is used [78]. For any history variable, the control variables contained in a vector $\boldsymbol{\zeta}^c$ can be obtained from the values at the Gauss points contained in a vector $\boldsymbol{\zeta}^g$ by solving [95]:

$$\mathbf{M}\boldsymbol{\zeta}^c = \int_V \mathbf{h}^T \boldsymbol{\zeta}^g \mathrm{d}V \tag{5.45}$$

where M is the least-squares fit matrix or Gramm matrix given by:

$$\mathbf{M} = \int_V \mathbf{h}\mathbf{h}^T \mathrm{d}V \tag{5.46}$$

and h a vector that contains the NURBS shape functions used to discretise the relevant history variable (e.g. the plastic multiplier as in eq. (**??**)). $\mathcal{T}^2$ is done in a similar way as $\mathcal{T}^0$ for the state vector. $\mathcal{T}^3$ is performed by interpolation using the shape functions:

$$\boldsymbol{\zeta}^g = \mathbf{h}\boldsymbol{\zeta}^c. \tag{5.47}$$

It is noted that we transfer both the old history variables (at the previous, converged loadstep) and the current history variables.

5.6 Numerical examples

We consider three classes of problems: gradient elasticity, classical plasticity and gradient plasticity. A plane strain assumption is made in all cases.

5.6.1 Gradient elasticity

Two problems are addressed - a thick cylinder subjected to external pressure for which an exact solution exists, and an L-shaped beam subjected to tractions. In both problems, Young's modulus E = 8100 MPa, Poisson ratio ν = 0.35 and the length scale ℓ = 0.01 m. Meshes with 5 hierarchical levels have been used. At each level k ($k = 1, \cdots, 5$), $2^k \times 2^k$ elements are employed to discretise the domain.

Thick hollow cylinder subjected to external pressure

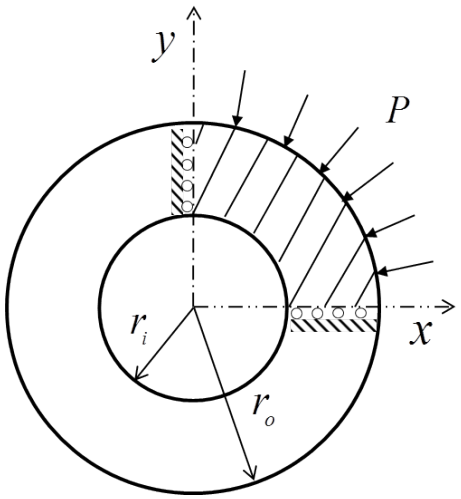

Figure 5.1: Geometry and dimensions of cylinder subjected to external pressure

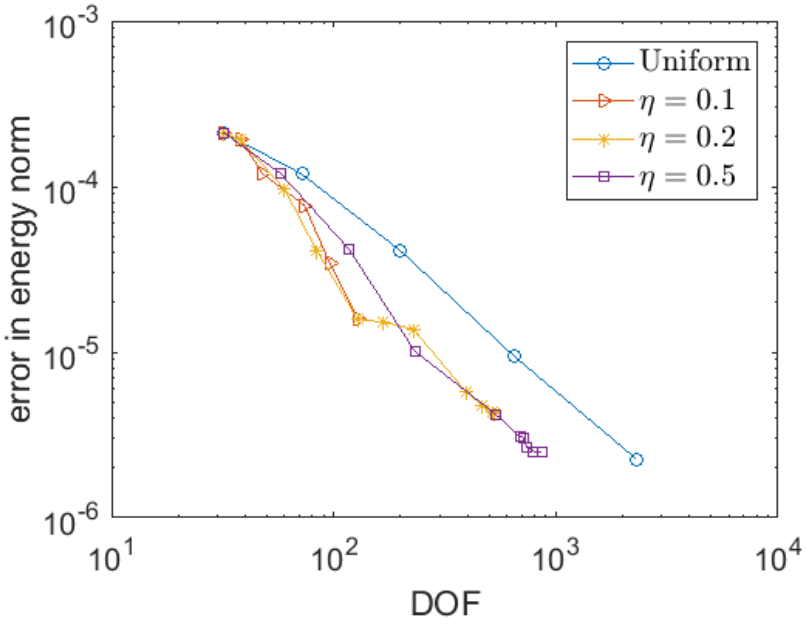

Figure 5.2: Convergence rates for different values of η. The results of hierarchical refinement and uniform refinement are shown.

The cylinder considered has an internal radius, r_i = 0.05 m and an external radius, r_o = 0.5 m. It is subjected to an external pressure P = 1 MPa. Only a quarter of the

cylinder is considered due to symmetry, see figure 5.1. The exact solution is given in [147]. The error in energy norm is used to mark elements for refinement using quantile marking. Three values of η are used - η = $\{0.1, 0.2, 0.5\}$. Uniform mesh refinement to the highest hierarchy level is also considered.

It is necessary to impose higher-order boundary conditions on the cylinder [147]. The set of control points immediately next to the boundaries are used as follows [50]:

$$\begin{aligned} &\frac{\partial u_y}{\partial x} = 0; \quad \text{enforced as} \quad u_y(2,j) = u_y(1,j) \quad \text{at the left boundary} \\ &\frac{\partial u_x}{\partial y} = 0; \quad \text{enforced as} \quad u_x(i,2) = u_x(i,1) \quad \text{at the bottom boundary} \end{aligned} \tag{5.48}$$

The boundary conditions have been imposed on control points across all hierarchy levels *a priori*.

The convergence rates are illustrated in figure 5.2. For uniform refinement, a convergence rate of $-P/2 = -1$ is obtained. It is clear that with hierarchical refinement, there is a reduction in the error. Hence, with less degrees of freedom, a higher accuracy, and therefore, a higher efficiency is obtained which is the main goal of adaptive analysis. The value of η does not seem to have a significant influence on the results.

The σ_{xy} plots and the relative error ϕ_e (cf. eq. (5.39)) in each element are shown in figures 5.3 and 5.4 respectively. The fact that there is no refinement close to the left and bottom boundaries is an indication that the boundary conditions have been imposed consistently. The error is concentrated at the inner boundary where the gradient of the strain is high. This is in line with results obtained in [50].

L-shaped panel subjected to traction

An L-shaped panel with dimension $a = 30$ m and subjected to a traction t = 1 MPa is considered next, figure 5.5. The top boundary is restricted in the vertical direction and the right boundary is constrained in the horizontal direction. To estimate the error, we use results of a mesh with $2^6 \times 2^6$ elements as the reference solution. Since the error estimation is now element-based, we use a slightly modified relation to calculate the relative error in each element [74]:

$$\hat{\phi}_e = \frac{\sqrt{\frac{1}{2}\sum_{i=1}^{4} (\hat{\boldsymbol{\sigma}} - \boldsymbol{\sigma})_i^T \cdot (\mathbf{D}^e)^{-1} \cdot (\hat{\boldsymbol{\sigma}} - \boldsymbol{\sigma})_i}}{\sqrt{\frac{1}{2}\sum_{i=1}^{4} \hat{\boldsymbol{\sigma}}_i \cdot (\mathbf{D}^e)^{-1} \cdot \hat{\boldsymbol{\sigma}}_i}} \tag{5.49}$$

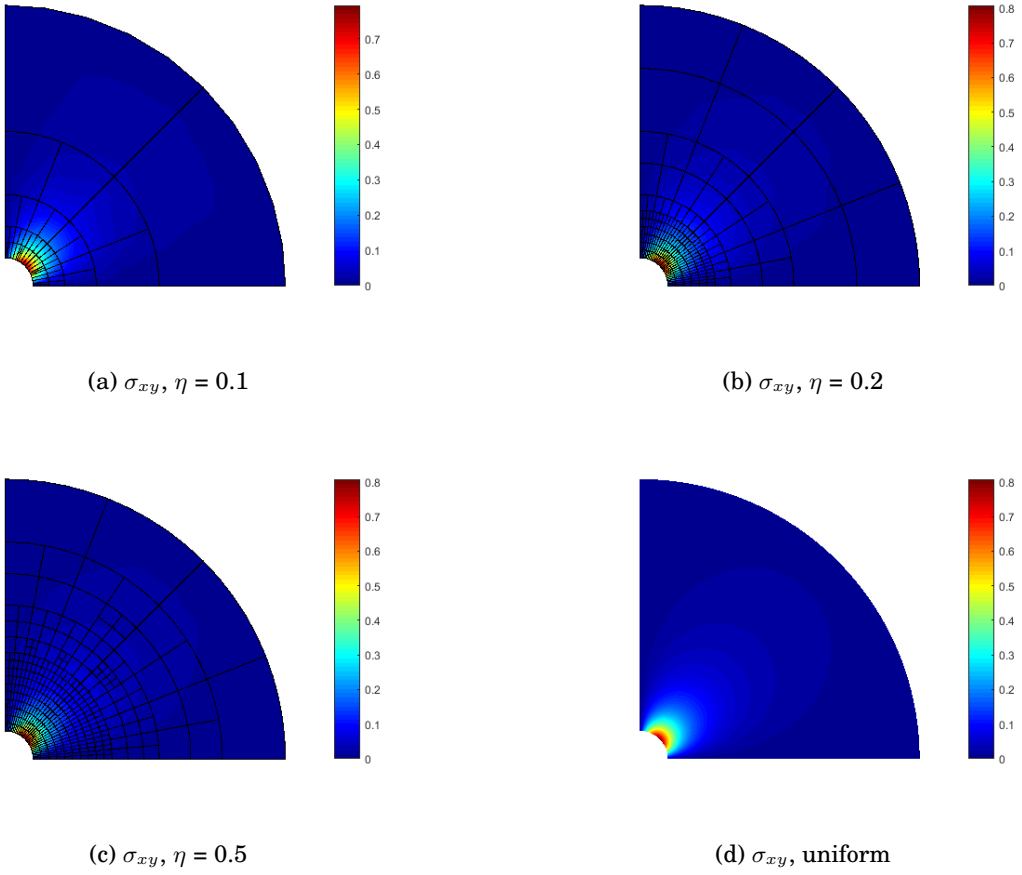

(a) σ_{xy}, η = 0.1

(b) σ_{xy}, η = 0.2

(c) σ_{xy}, η = 0.5

(d) σ_{xy}, uniform

Figure 5.3: σ_{xy} [MPa] components of the stress of each element for different values of η.

where summation is over the vertices; $\hat{\boldsymbol{\sigma}}_i$ and $\boldsymbol{\sigma}_i$ denote the stress at the vertex i for the reference solution and the numerical solution respectively.

The convergence plot is given in figure 5.6 but only serves as an indicator considering the reference solution employed. It again shows that hierarchical refinement reduces the error while maintaining minimal number of degrees of freedom. Quantile marking for element refinement is considered here with η values of 0.13 and 0.17. The σ_{xy} stress component as well as the relative error in each element are presented in figure 5.7 up to results for the highest hierarchical level.

It is clear from figure 5.7 that the stress concentration at the inner corner is captured well. The gradient elasticity effect in removing the stress singularity is also seen

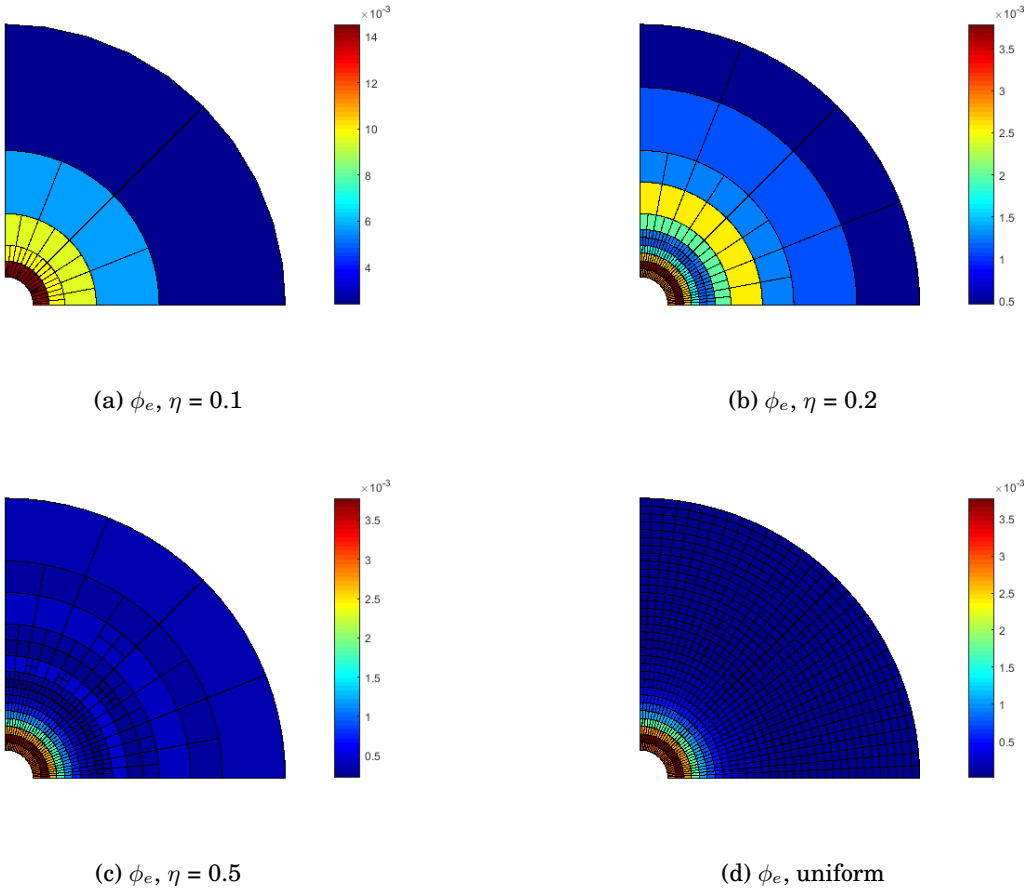

(a) ϕ_e, η = 0.1

(b) ϕ_e, η = 0.2

(c) ϕ_e, η = 0.5

(d) ϕ_e, uniform

Figure 5.4: Relative error norm ϕ_e of each element for different values of η.

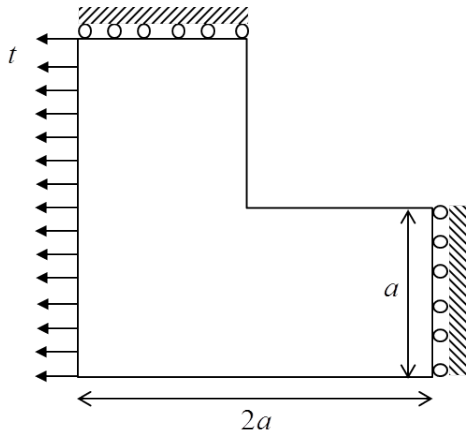

Figure 5.5: Geometry of L-shaped panel

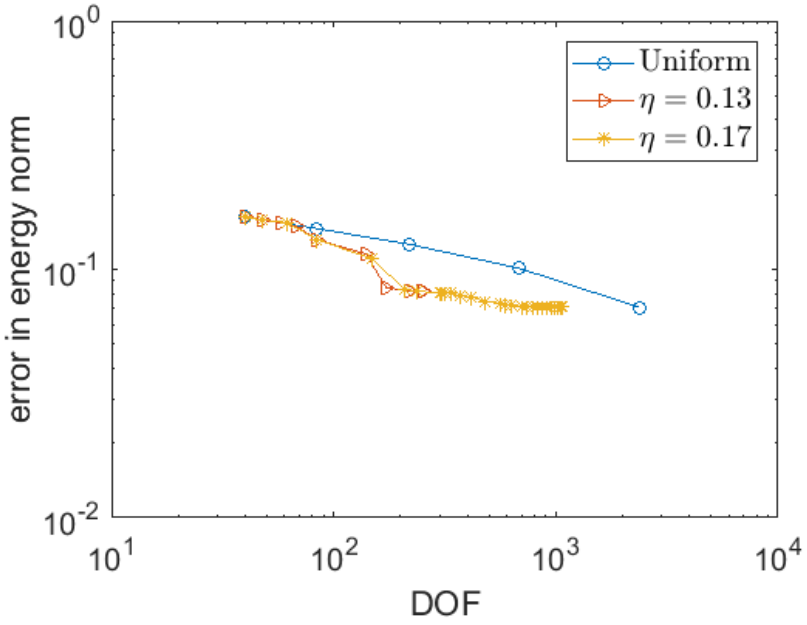

Figure 5.6: Indicative convergence for uniform and hierarchical refinement for L-shaped panel.

near the singularity.

5.6.2 Classical plasticity

In a step-wise manner, classical plasticity is considered as the first non-linear problem. We again consider a plane strain cylinder (a quarter of the geometry due to symmetry) but this time subjected to internal pressure P_i. The cylinder, with inner radius a and outer radius b, is assumed to be elastic-perfectly plastic using the Von Mises yield criterion. Beyond a certain critical pressure P_{cr}, there is a region of plastic deformation, $a \leq r \leq c$, defined by the radius r and the elastic-plastic boundary c. The value of c is determined by solving the following equation numerically [40]:

$$P_i = k\left(\ln\left(\frac{c}{a}\right) + \frac{1}{2}\left(1 - \frac{c^2}{b^2}\right)\right) \tag{5.50}$$

where $k = \sigma_y/\sqrt{3}$ and σ_y is the yield stress. The critical pressure is calculated using:

$$P_{cr} = \frac{k}{2}\left(1 - \frac{c^2}{b^2}\right) \tag{5.51}$$

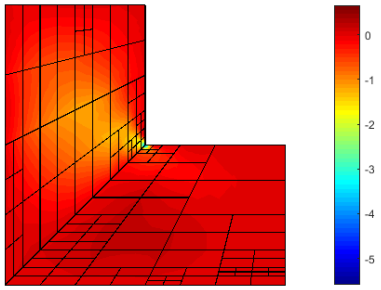

(a) η = 0.13

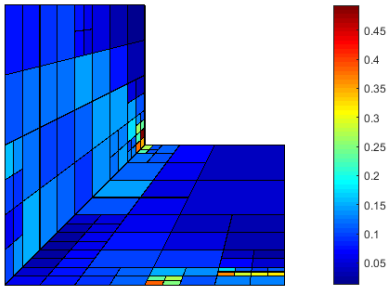

(b) η = 0.13

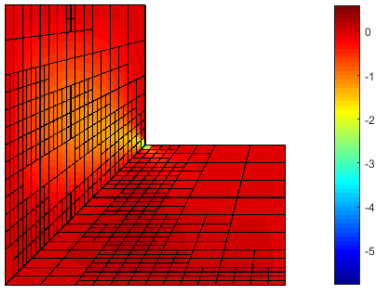

(c) η = 0.17

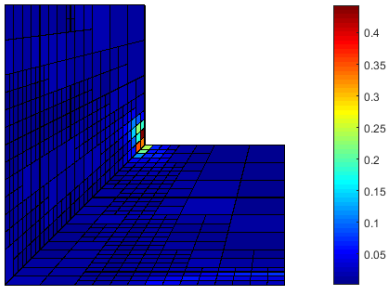

(d) η = 0.17

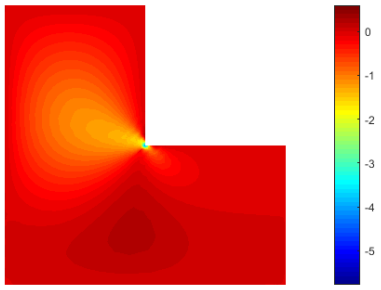

(e) uniform

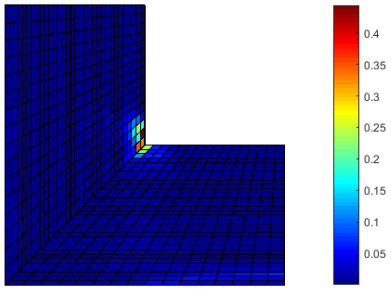

(f) uniform

Figure 5.7: σ_{xy} [MPa] components of the stress (left) and relative error norm ϕ_e (right) of each element for different values of η.

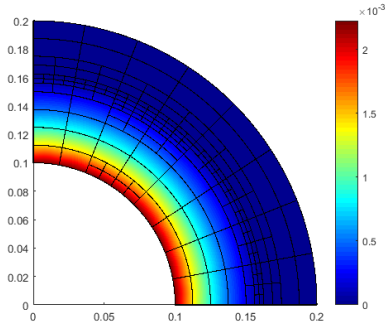

(a) plastic strain

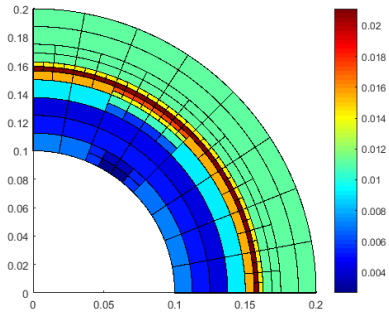

(b) error in energy norm

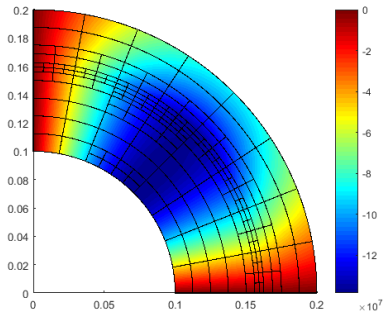

(c) σ_{xy}

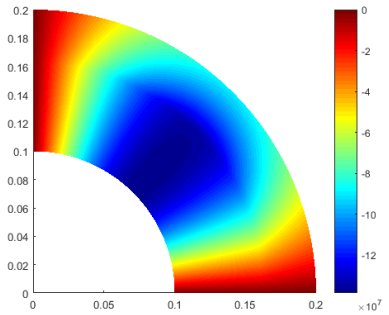

(d) σ_{xy} uniform

Figure 5.8: Plastic strain, error in energy norm, σ_{xy} [MPa] as well as its analytical solution for elastic-perfectly plastic cylinder.

For a cylinder with a = 0.1 m, b = 0.2 m, ν = 0.3, σ_y = 0.24 GPa and E = 210 GPa, P_{cr} = 0.10375 GPa. For an applied pressure of 0.18 GPa($> P_{cr}$), c = 0.15979 m. In the plastic region, the stresses are ($\sigma_{r\theta} = 0$):

$$\sigma_r = -k\left(1 - \frac{c^2}{b^2} + \ln\frac{c^2}{r^2}\right), \quad \sigma_\theta = k\left(1 + \frac{c^2}{b^2} - \ln\frac{c^2}{r^2}\right); \quad \text{for } a < r < c \tag{5.52}$$

In the elastic region, they are computed as

$$\sigma_r = -k\left(1 - \frac{c^2}{b^2} + \ln\frac{c^2}{r^2}\right), \quad \sigma_\theta = k\left(1 + \frac{c^2}{b^2} - \ln\frac{c^2}{r^2}\right); \quad \text{for } c < r < b \tag{5.53}$$

The problem is solved using adaptive isogeometric analysis. Similar to gradient elasticity, the relative error in energy norm is adopted with quantile marking using $\eta = 0.2$. The plots of the plastic strain and the σ_{xy} component of the stress are presented in figure 5.8. σ_{xy} is retrieved as $\sigma_{xy} = (\sigma_r - \sigma_\theta)(xy/r^2)$. A good match with the reference

result is obtained, which indicates that the hierarchical refinement model works well and that the variables are transferred properly. Moreover, from the plot of the plastic strain in figure 5.8a, the radius c at the elastic-plastic boundary is close to the analytical value of 0.16. The relative error in energy norm is also plotted and it is clear that the error is highest at the elastic-plastic boundary.

5.6.3 Gradient plasticity

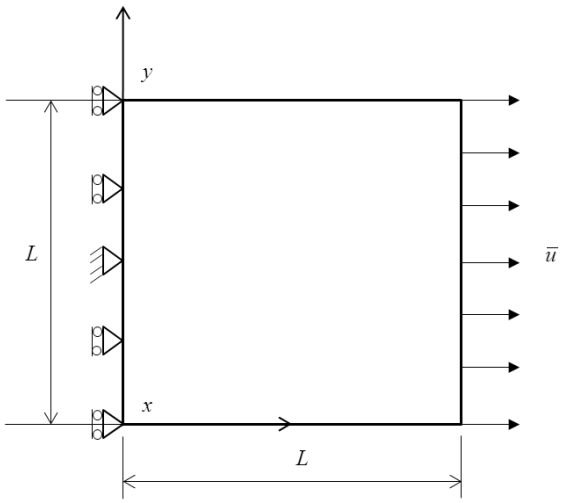

Figure 5.9: Geometry of square plate under uniaxial tension.

Finally, a localisation problem is considered using implicit gradient plasticity [77], see chapter 4. The problem is illustrated in figure 5.9. A square panel of length L = 10 m is constrained on the left side and uniaxial tension is applied on the opposite side. For the material parameters, E = 20000 N/mm^2, H = 2000 N/mm^2, $\sigma_{y,0}$ = 2 N/mm^2, $\beta = 3500$ and $\ell = 0.7$ mm. A mesh with four levels is considered. At each level k ($k = 1, \cdots, 4$), $2^{k+1} \times 2^{k+1}$ elements are employed to discretise the domain. To trigger localisation, the bottom left element in the coarsest mesh and all children down the hierarchy are weakened by assuming a 5% reduction in the yield strength.

Elements are marked for refinement only after the nonlocal plastic strain has become non-zero. Let κ_{max} be the maximum plastic strain. Elements with up to 9% of κ_{max} are marked for refinement and refinement is continued until $d < 0.5$ (cf. (5.42)).

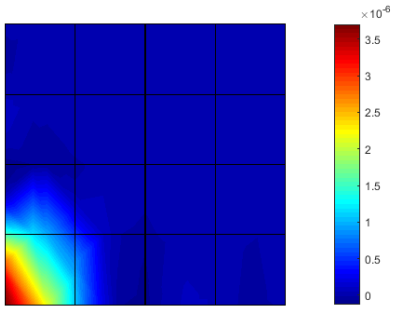

(a) $\bar{u} = 0.00091$ mm

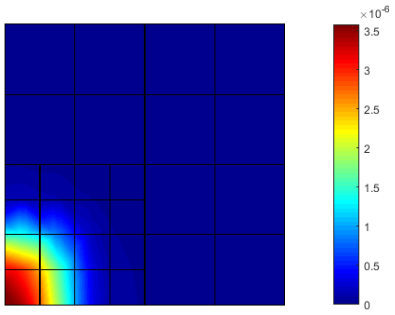

(b) $\bar{u} = 0.00091$ mm

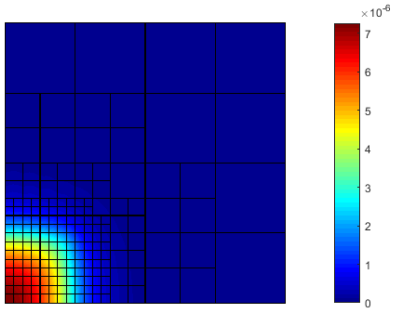

(c) $\bar{u} = 0.00093$ mm

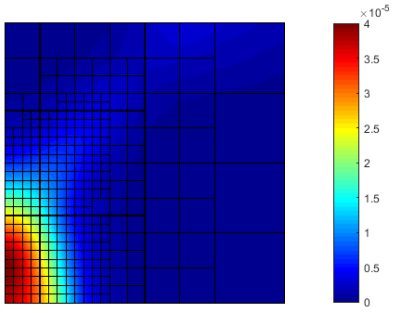

(d) $\bar{u} = 0.00100$ mm

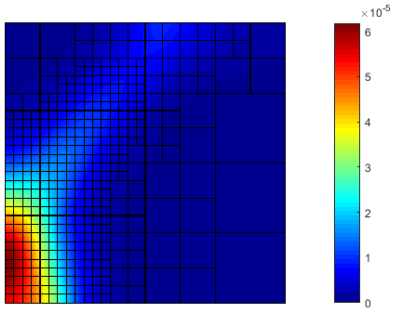

(e) $\bar{u} = 0.00101$ mm

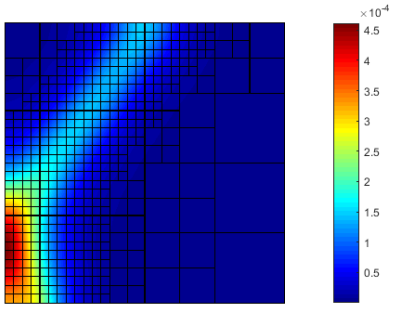

(f) $\bar{u} = 0.00114$ mm

Figure 5.10: Nonlocal effective plastic strain: Adaptive refinement as localisation band progresses.

Hence, there is progressive refinement as the deformation localises. This is clear from the results which are shown in figure 5.10.

Here, the robustness of the scheme is also apparent since we start with elements that would normally not allow the shearband to develop. This is particularly seen in the first case (in figure 5.10) when localisation starts. With further refinement, the band propagates smoothly. It is important to ensure that the presented results are similar to those obtained from a standard uniformly refined mesh in the literature [45, 77] as well as chapter 4. A comparison is shown for the local and nonlocal effective plastic strain (figure 5.11). Further confirmation is pursued by comparing the force-

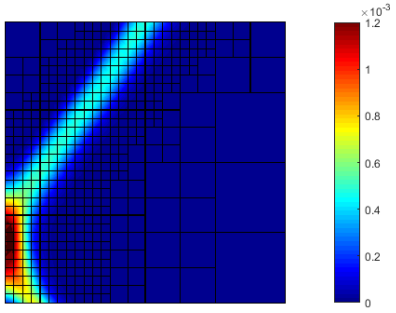

(a) local, hierarchical

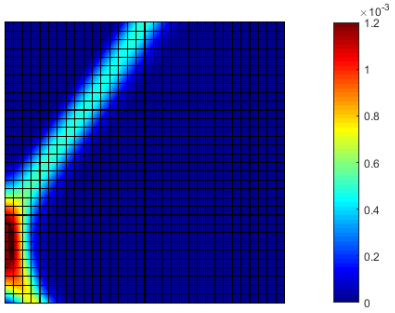

(b) local, uniform

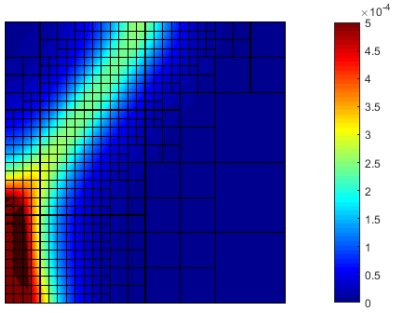

(c) nonolocal, hierarchical

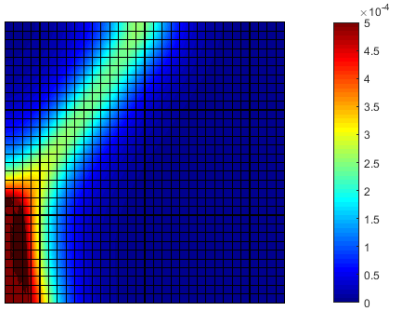

(d) nonlocal, uniform

Figure 5.11: Comparison of local and nonlocal effective plastic strains for standard and adaptive implicit gradient plasticity, $\bar{u} = 0.0012$ mm. The local measure has a less pronounced nonlocal or smearing effect.

displacement curves which show also very good agreement, see figure 5.12. Moreover in terms of computational time, about half of the time required for the fine mesh (figure 5.11 (b) and (d)) is needed in the case of adaptive refinement (figure 5.11 (a) and (c)).

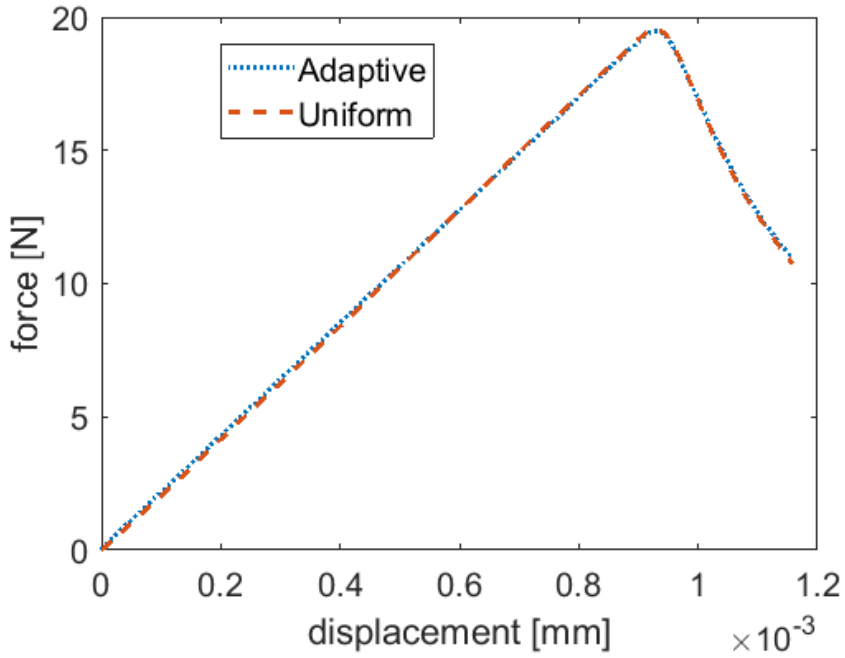

Figure 5.12: Force-displacement curves for uniform and adaptive implicit gradient plasticity analyses.

5.7 Conclusion

This work has extended adaptive isogeometric analysis to strain-gradient continuum models - gradient elasticity and gradient plasticity. Hierarchical refinement using truncated multi-level basis functions which interact through a subdivision operator has been adopted within the Beziér element framework. Elements are marked for refinement using the relative error in energy norm for gradient elasticity. For gradient plasticity, a measure of the effective plastic strain is used to mark and refine elements which need to better capture the localising deformation. Refinement is based on the concept of elements and their child elements which are activated or deactivated accordingly. When an element is refined, the current as well as the old history variables

are transferred from the integration points of the old mesh to its control points using global least-squares approximation. Next, they are transferred to the control points of the new mesh using a modified subdivision operator. They are finally transferred to the integration points of the new mesh by shape function interpolation. The results have been verified against benchmarks in the literature.

Chapter 6

CONCLUSION AND FUTURE PROSPECTS

6.1 Conclusion

6.1.1 Research objectives addressed

This work aimed at developing an efficient computational framework that incorporates gradient-enhanced elasticity and gradient-enhanced plasticity based on isogeometric analysis. The first objective is the development, implementation and assessment of an isogeometric analysis framework for gradient elasticity and gradient plasticity. This was achieved by:

- development of an isogeometric analysis framework for gradient elasticity considering direct and staggered discretisation, as well as NURBS and T-splines.
- convergence analysis and comparison of both solution approaches using L_2 error norm of the displacements and stresses
- development of an isogeometric analysis framework for explicit and implicit second-order gradient plasticity models
- development of a fourth-order implicit gradient plasticity model using the Gaussian weight function
- dispersion analysis of the explicit and implicit gradient plasticity models

The second objective of this work is the development of an adaptive scheme to enable efficient computations. This was achieved by:

- development of a hierarchical refinement framework for gradient elasticity based on error in energy norm

- development of a hierarchical refinement framework for gradient plasticity using the length scale and nonlocal plastic strain measure

6.1.2 Summary

Gradient elasticity

The *size effect* is a phenomenon observed in several engineering materials and it occurs due to heterogenities of the material at the micro-scale. The usual classical continuum theories cannot account for it because of a macro-scale assumption. By introducing an internal length scale into the constitutive equations, this problem is solved. For materials that deform elastically, the Laplacian of the strain is used to modify the constitutive relations so that a *gradient elasticity* model results. If this equation is to be solved *monolithically*, the continuity requirements for the discretisation of this model move from $\mathcal{C}^0$ to $\mathcal{C}^1$. This is not easily achieved with traditional finite elements. In this work, *isogeometric analysis* has been employed to meet the discretisation requirements. This approach to analysis has the advantage that the specimen geometry is exact because it eliminates the extra step (in standard finite elements) where the geometry is approximated before analysis. Isogeometric analysis adopts spline shape functions (like the widely-adopted Non-Uniform Rational B-Splines - NURBS) which are usually used for design, and thus both design and analysis employ the same functions. One particular edge that isogeometric analysis has over other discretisation methods is that splines are naturally higher-order, and therefore, higher-order continuity is only a matter of choice.

In an effort to proffer alternatives to the higher-order continuity requirement for gradient elasticity, a *staggered* solution scheme has been proposed, where the differential equation is solved in two steps. This can be achieved with standard $\mathcal{C}^0$-continuous finite elements. A convergence analysis was carried out in this thesis for both the monolithic and staggered approaches. In short,

- Slight differences were observed in the results for cases where boundary conditions need to be imposed. This suggests that the staggered approach, *strictly speaking*, only applies to infinite problems where there is no need to im-

pose any boundary conditions.

- For the monolithic approach, theoretical convergence rates were retrieved for splines of polynomial order three and above. For polynomial order of two, sub-optimal convergence rate was observed, confirming earlier studies for another fourth-order partial differential equation, the *Cahn-Hilliard* equation.

The restrictive tensor-product nature of NURBS motivated a further study of gradient elasticity with the more flexible T-splines. Local refinement was performed based on T-splines and good results were obtained.

Gradient plasticity

For *softening* materials that deform plastically, a spurious dependency of the solution on the mesh used for analysis is observed. This is nonphysical because the force-displacement curve, which represents the energy dissipated during deformation, should remain constant. Making the yield function dependent on the Laplacian of the plastic strain solves this problem but gives rise to an additional partial differential equation (for the plastic multiplier) that needs to be solved. This is referred to as the *explicit gradient plasticity formulation*. Appropriate boundary conditions need to be imposed on the moving elastic-plastic boundary. To avoid tracking the moving boundary, $\mathcal{C}^1$ continuity condition is required for discretising the plastic multiplier. To consistently discretise the problem with $\mathcal{C}^1$-continuous shape functions for the plastic multiplier and $\mathcal{C}^2$-continuous shape functions for the displacements, again splines were adopted. A nice property of the isogeometric analysis approach adopted in this thesis is that the standard finite element data structure is maintained. This is achieved through *Beziér extraction* which decomposes NURBS or T-spline basis functions using Bernstein polynomials. To facilitate the cubic-quadratic interpolation of variables and ensure conforming meshes, *Beziér projection* was employed. In a nutshell,

- The results obtained were in agreement with the available analytical solution for a tensile bar in one dimension

- Problems in both one and two dimensions were addressed and results confirmed

earlier reports of the need for the finite element size to be smaller than the length scale

- Compared with finite element approaches that use Hermitian shape functions for the plastic multiplier or mixed finite element approaches, isogeometric analysis has the distinct advantage that no interpolation of derivatives is required. This advantage showed up especially in the boundary conditions, where no nonphysical constraints had to be imposed.

- Explicit gradient plasticity works fine, but convergence is not guaranteed. Convergence was achieved only for a low ratio of the hardening modulus H to elastic modulus E and was difficult for higher ratios.

A more stable computational framework was achieved by using the Laplacian of the *nonlocal* plastic strain in the yield function. This is the *implicit gradient plasticity formulation*. However, in this formulation, the yield function has to be modified further to achieve full *regularisation*. One way of doing this, which was considered in this work, is to multiply the yield function by a damage function. However, the damage variable can potentially have some physical effects. Incorrect failure patterns can also arise due to the non-local averaging of the implicit formulation [130]. Succinctly,

- Both second-order and fourth-order implicit gradient formulations were considered with unequal as well as equal orders of interpolation. The former was formulated using a Green's weighting function, while in the latter, a Gaussian weighting function was used.

- Although the fourth-order implicit gradient formulation has higher regularisation potential, the second-order formulation also gives good regularisation. The shear band of the second-order formulation is also slightly wider, corroborating the results from dispersion analysis.

- An upward curving of the shear band near the free boundary was observed for the implicit gradient formulations. This is related to the emergence of stationary

Rayleigh waves, and has been observed in other simulations as well.

- While the length scale sets the localisation band width, the yield function adopted influences the orientation of the shearband

- The study on equal and unequal orders of interpolation revealed the same results for both cases. This asserts that gradient formulations are coupled problems and the interpolation functions of different variables that have to be discretised are not necessarily related.

Largely due to the computational stability of the implicit gradient formulation, it was chosen for further development within the spline-based framework developed.

Adaptivity for gradient elasticity and gradient plasticity

Good accuracy requires the finite element size employed in simulations to be smaller than the internal length scale. This can incur high computational cost especially when considering large structures. Hence, adaptive refinement, particularly close to the localisation area, becomes an attractive option. NURBS have a tensor-product nature which makes adaptive refinement non-trivial. This thesis adopted the truncated hierarchical NURBS bases, cast in the Beziér extraction framework, for refinement. Refinement was performed based on a multi-level mesh with element-wise hierarchical basis functions interacting through an inter-level subdivision operator. Concisely,

- The error in energy norm was adopted for gradient elasticity and classical plasticity and this gave very promising results along with the quantile marking strategy.

- The heuristic marking of elements using the effective plastic strain measure and the length scale enabled analysis even with a mesh size well above the length scale, which is then refined accordingly when needed. This significantly improved efficiency.

- Standard transfer operations for history variables between the integration points of the old mesh to the integration points of the new mesh gave good results.

- A *robust computational framework* for engineering analysis materialised, combining the flexibility, exact geometry representation, and expedited design-through-analysis of *isogeometric analysis*, size-effect capabilities and mesh-objective results of *gradient enhanced continua*, the standard convenient data structure of *finite element analysis* and the improved efficiency of *adaptive hierarchical refinement*.

6.1.3 Contributions

The contributions of this work can be outlined as follows:

- New insight from the convergence analysis of the monolithic gradient-elastic formulation and limitations of the staggered scheme
- Development of an isogeometric analysis framework for explicit gradient plasticity
- Development of an isogeometric analysis framework for implicit gradient plasticity formulations
- Development of a fourth-order implicit gradient plasticity model and associated dispersion analyses
- New deductions from the results of the implicit gradient plasticity formulations
- New observations into computational stability of explicit vs implicit gradient plasticity formulations
- Development of a hierarchical refinement framework based on isogeometric analysis for gradient-elasticity and gradient-plasticity

6.2 Future prospects

The aims of this work have been achieved, nevertheless, there remain various avenues for future exploration.

- The computational framework has been put in place. A natural progression would be to apply the approach towards more practical engineering problems. Some further work might be required in using the framework in a practical context. For example, for gradient elastic problems, the exact solution is not ideally available. Thus other error estimators such as those based on residuals or superconvergent patch recovery can be used [25].

- The evolution of the effective plastic strain in the implicit formulation considered assumes that the interaction domain increases with plastic deformation. This can lead to incorrect failure patterns [130]. A contrary view where the interaction domain decreases with plastic deformation can be considered. This might give a more realistic evolution of the plastic strain as has been shown for damage models [116].

- Another possibility is adaptive gradient plasticity through state variable transfer. For both explicit and implicit gradient plasticity formulations, an additional partial differential equation which necessitates the discretisation of the local or nonlocal plastic strains, respectively, comes into play. This might eliminate the need to transfer any history variable. Transfer can be limited to state variables, and then history variables are re-computed from them.

- Various transfer operators have been proposed for variable transfer between two consecutive mesh levels, e.g. [59]. It might be worthy to employ other transfer operators that might result in better efficiency and/or accuracy.

- The problems considered in this thesis were limited to two-dimensional small-strain analyses. Full three-dimensional analyses that allow large deformations would make the framework more versatile. A little more work may be required for three-dimensional hierarchical refinement.

- An initial study based on the Von Mises yield criterion suggested influence of the yield function on the shearband orientation. It will be useful to consider various yield functions and compare the results with experiments.

- Only simple geometries have been considered in this work. More practical engineering problems would require multi-patch geometries in the isogeometric analysis framework. Adopting an appropriate technique for multi-patch analysis would be worth-while.

BIBLIOGRAPHY

[1] R. Abdollahi and B. Boroomand. Nonlocal elasticity defined by Eringen's integral model: Introduction of a boundary layer method. *International Journal of Solids and Structures*, 51(9):1758–1780, 2014.

[2] E. C. Aifantis. On the role of gradients in the localization of deformation and fracture. *International Journal of Engineering Science*, 30(10):1279–1299, 1992.

[3] E. C. Aifantis. Strain gradient interpretation of size effects. *International Journal of Fracture*, 95(1-4):299, 1999.

[4] R. K. A. Al-Rub. *Material length scales in gradient-dependent plasticity / damage and size effects: theory and computation*. PhD thesis, Louisiana State University, 2004.

[5] R. K. A. Al-Rub and G. Z. Voyiadjis. Analytical and experimental determination of the material intrinsic length scale of strain gradient plasticity theory from micro-and nano-indentation experiments. *International Journal of Plasticity*, 20(6):1139–1182, 2004.

[6] B. Altan and E. Aifantis. On some aspects in the special theory of gradient elasticity. *Journal of the Mechanical Behavior of Materials*, 8(3):231–282, 1997.

[7] E. Amanatidou and N. Aravas. Mixed finite element formulations of strain-gradient elasticity problems. *Computer Methods in Applied Mechanics and Engineering*, 191(15):1723–1751, 2002.

[8] A. Arsenlis and D. Parks. Crystallographic aspects of geometrically-necessary and statistically-stored dislocation density. *Acta materialia*, 47(5):1597–1611, 1999.

[9] H. Askes. *Advanced spatial discretisation strategies for localised failure-mesh adaptivity and meshless methods*. TU Delft, Delft University of Technology, 2000.

[10] H. Askes and E. C. Aifantis. Numerical modeling of size effects with gradient elasticity-formulation, meshless discretization and examples. *International Journal of Fracture*, 117(4):347–358, 2002.

[11] H. Askes and E. C. Aifantis. Gradient elasticity in statics and dynamics: An overview of formulations, length scale identification procedures, finite element implementations and new results. *International Journal of Solids and Structures*, 48(13):1962–1990, 2011.

[12] H. Askes and M. A. Gutiérrez. Implicit gradient elasticity. *International Journal for Numerical Methods in Engineering*, 67(3):400–416, 2006.

[13] H. Askes, I. Morata, and E. C. Aifantis. Finite element analysis with staggered gradient elasticity. *Computers & Structures*, 86(11):1266–1279, 2008.

[14] H. Askes, J. Pamin, and R. de Borst. Dispersion analysis and element-free Galerkin solutions of second-and fourth-order gradient-enhanced damage models. *International Journal for Numerical Methods in Engineering*, 49:811–832, 2000.

[15] Autodesk Inc., 2011. http://www.tsplines.com/products/tsplines-for-rhino.html.

[16] C. Bagni and H. Askes. Unified finite element methodology for gradient elasticity. *Computers & Structures*, 160:100–110, 2015.

[17] Z. Bažant and F.-B. Lin. Non-local yield limit degradation. *International Journal for Numerical Methods in Engineering*, 26:1805–1823, 1988.

[18] Z. P. Bažant, T. B. Belytschko, and T.-P. Chang. Continuum theory for strain-softening. *Journal of Engineering Mechanics*, 110:1666–1692, 1984.

[19] Z. P. Bažant and M. Jirásek. Nonlocal integral formulations of plasticity and damage: Survey of progress. *Journal of Engineering Mechanics*, 128(11):1119–1149, 2002.

[20] Z. P. Bažant and B. H. Oh. Crack band theory for fracture of concrete. *Matériaux et construction*, 16(3):155–177, 1983.

[21] Z. P. Bazant and J. Planas. *Fracture and Size Effect in Concrete and other Quasibrittle Materials*. CRC Press, Boca Raton, 1997.

[22] E. Benvenuti and A. Simone. One-dimensional nonlocal and gradient elasticity: Closed-form solution and size effect. *Mechanics Research Communications*, 48:46–51, 2013.

[23] L. Berger-Vergiat, C. McAuliffe, and H. Waisman. Isogeometric analysis of shear bands. *Computational Mechanics*, 54(2):503–521, 2014.

[24] M. J. Borden, M. A. Scott, J. A. Evans, and T. J. R. Hughes. Isogeometric finite element data structures based on Bézier extraction of NURBS. *International Journal for Numerical Methods in Engineering*, 87:15–47, 2011.

[25] Ü. H. Çalık-Karaköse and H. Askes. A recovery-type a posteriori error estimator for gradient elasticity. *Computers & Structures*, 154:204–209, 2015.

[26] P. Casal. La capillarité interne. *Cahier du groupe Français de rhéologie, CNRS VI*, 3:31–37, 1961.

[27] N. Challamel and C. Wang. The small length scale effect for a non-local cantilever beam: A paradox solved. *Nanotechnology*, 19(34):345703, 2008.

[28] L. Chen and R. de Borst. Adaptive refinement of hierarchical T-splines. *Computer Methods in Applied Mechanics and Engineering*, 337:220–245, 2018.

[29] L. Chen, E. J. Lingen, and R. de Borst. Adaptive hierarchical refinement of NURBS in cohesive fracture analysis. *International Journal for Numerical Methods in Engineering*, 112(13):2151–2173, 2017.

[30] F. Cirak, M. Ortiz, and P. Schroder. Subdivision surfaces: A new paradigm for thin-shell finite-element analysis. *International Journal for Numerical Methods in Engineering*, 47(12):2039–2072, 2000.

[31] E. Cosserat and F. Cosserat. *Théorie des Corps Déformables*. Hermann et fils, Paris, 1909.

[32] J. A. Cottrell, T. J. Hughes, and Y. Bazilevs. *Isogeometric Analysis: Toward Integration of CAD and FEA*. John Wiley & Sons, Chichester, 2009.

[33] R. de Borst. Simulation of strain localization: A reappraisal of the Cosserat continuum. *Engineering Computations*, 8(4):317–332, 1991.

[34] R. de Borst, M. A. Crisfield, J. J. C. Remmers, and C. V. Verhoosel. *Non-linear Finite Element Analysis of Solids and Structures*. John Wiley & Sons, Chichester, second edition, 2012.

[35] R. de Borst and H.-B. Mühlhaus. Gradient-dependent plasticity: Formulation and algorithmic aspects. *International Journal for Numerical Methods in Engineering*, 35(3):521–539, 1992.

[36] R. de Borst and J. Pamin. Some novel developments in finite element procedures for gradient-dependent plasticity. *International Journal for Numerical Methods in Engineering*, 39(14):2477–2505, 1996.

[37] R. de Borst, J. Pamin, R. H. J. Peerlings, and L. J. Sluys. On gradient-enhanced damage and plasticity models for failure in quasi-brittle and frictional materials. *Computational Mechanics*, 17:130–141, 1995.

[38] R. de Borst, J. Réthoré, and M. A. Abellan. A numerical approach for arbitrary cracks in a fluid-saturated medium. *Archive of Applied Mechanics*, 75:595–606, 2006.

[39] R. de Borst, L. Sluys, H.-B. Mühlhaus, and J. Pamin. Fundamental issues in finite element analyses of localization of deformation. *Engineering Computations*, 10(2):99–121, 1993.

[40] E. A. de Souza Neto, D. Perić, and D. R. Owen. *Computational Methods for Plasticity: Theory and Applications*. John Wiley & Sons, Chichester, 2011.

[41] G. Di Luzio and Z. P. Bažant. Spectral analysis of localization in nonlocal and over-nonlocal materials with softening plasticity or damage. *International Journal of Solids and Structures*, 42:6071–6100, 2005.

[42] Dynaflow Research Group. Jive v2.2, 2016. http://www.jem-jive.com/.

[43] T. Elguedj and T. J. Hughes. Isogeometric analysis of nearly incompressible large strain plasticity. *Computer Methods in Applied Mechanics and Engineering*, 268:388–416, 2014.

[44] R. A. B. Engelen, N. A. Fleck, R. H. J. Peerlings, and M. G. D. Geers. An evaluation of higher-order plasticity theories for predicting size effects and localisation. *International Journal of Solids and Structures*, 43:1857–1877, 2006.

[45] R. A. B. Engelen, M. G. D. Geers, and F. P. T. Baaijens. Nonlocal implicit gradient-enhanced elasto-plasticity for the modelling of softening behaviour. *International Journal of Plasticity*, 19:403–433, 2003.

[46] A. C. Eringen. On differential equations of nonlocal elasticity and solutions of screw dislocation and surface waves. *Journal of Applied Physics*, 54(9):4703–4710, 1983.

[47] A. C. Eringen and B. S. Kim. Stress concentration at the tip of crack. *Mechanics Research Communications*, 1(4):233–237, 1974.

[48] A. C. Eringen, C. Speziale, and B. Kim. Crack-tip problem in non-local elasticity. *Journal of the Mechanics and Physics of Solids*, 25(5):339–355, 1977.

[49] A. C. Eringen and E. Suhubi. Nonlinear theory of simple micro-elastic solids–I. *International Journal of Engineering Science*, 2(2):189–203, 1964.

[50] P. Fischer, M. Klassen, J. Mergheim, P. Steinmann, and R. Müller. Isogeometric analysis of 2D gradient elasticity. *Computational Mechanics*, 47(3):325–334, 2011.

[51] N. Fleck, G. Muller, M. Ashby, and J. Hutchinson. Strain gradient plasticity: Theory and experiment. *Acta Metallurgica et Materialia*, 42(2):475–487, 1994.

[52] P. Fredriksson, P. Gudmundson, and L. P. Mikkelsen. Finite element implementation and numerical issues of strain gradient plasticity with application to metal matrix composites. *International Journal of Solids and Structures*, 46(22):3977–3987, 2009.

[53] X.-L. Gao and S. Park. Variational formulation of a simplified strain gradient elasticity theory and its application to a pressurized thick-walled cylinder problem. *International Journal of Solids and Structures*, 44(22):7486–7499, 2007.

[54] M. Geers, R. de Borst, W. Brekelmans, and R. Peerlings. Validation and internal length scale determination for a gradient damage model: Application to short glass-fibre-reinforced polypropylene. *International Journal of Solids and Structures*, 36(17):2557–2583, 1999.

[55] C. Giannelli, B. Jüttler, and H. Speleers. THB-splines: The truncated basis for hierarchical splines. *Computer Aided Geometric Design*, 29(7):485–498, 2012.

[56] H. Gómez, V. M. Calo, Y. Bazilevs, and T. J. Hughes. Isogeometric analysis of the Cahn–Hilliard phase-field model. *Computer Methods in Applied Mechanics and Engineering*, 197(49):4333–4352, 2008.

[57] P. L. Gould. *Introduction to Linear Elasticity*. Springer, New York, 3 edition, 2013.

[58] W. Han and X. Meng. Some studies of the reproducing kernel particle method. In *Meshfree Methods for Partial Differential Equations*, pages 193–210. Springer, 2003.

[59] P. Hennig, M. Ambati, L. De Lorenzis, and M. Kästner. Projection and transfer operators in adaptive isogeometric analysis with hierarchical B-splines. *Computer Methods in Applied Mechanics and Engineering*, 334:313–336, 2018.

[60] P. Hennig, S. Müller, and M. Kästner. Bézier extraction and adaptive refinement of truncated hierarchical NURBS. *Computer Methods in Applied Mechanics and Engineering*, 305:316–339, 2016.

[61] K. Höllig. *Finite Element Methods with B-Splines*. SIAM, Philadelphia, 2003.

[62] A. Huerta and G. Pijaudier-Cabot. Discretization influence on regularization by two localization limiters. *Journal of Engineering Mechanics*, 120(6):1198–1218, 1994.

[63] T. J. R. Hughes, J. A. Cottrell, and Y. Bazilevs. Isogeometric analysis: CAD, finite elements, NURBS, exact geometry and mesh refinement. *Computer Methods in Applied Mechanics and Engineering*, 194:4135–4195, 2005.

[64] K. Jakata and A. Every. Determination of the dispersive elastic constants of the cubic crystals Ge, Si, GaAs, and InSb. *Physical Review B*, 77(17):174301, 2008.

[65] H. Javani, R. Peerlings, and M. Geers. Consistent remeshing and transfer for a three dimensional enriched mixed formulation of plasticity and non-local damage. *Computational Mechanics*, 53(4):625–639, 2014.

[66] M. Jirásek and S. Rolshoven. Comparison of integral-type nonlocal plasticity models for strain-softening materials. *International Journal of Engineering Science*, 41:1553–1602, 2003.

[67] M. Jirásek and S. Rolshoven. Localization properties of strain-softening gradient plasticity models. Part II: Theories with gradients of internal variables. *International Journal of Solids and Structures*, 46:2239–2254, 2009.

[68] X. Ju and R. Mahnken. Goal-oriented adaptivity for linear elastic micromorphic continua based on primal and adjoint consistency analysis. *International Journal for Numerical Methods in Engineering*, 112(8):1017–1039, 2017.

[69] M. Kästner, P. Metsch, and R. de Borst. Isogeometric analysis of the Cahn–Hilliard equation–a convergence study. *Journal of Computational Physics*, 305:360–371, 2016.

[70] A. Khoei, S. Gharehbaghi, A. Tabarraie, and A. Riahi. Error estimation, adaptivity and data transfer in enriched plasticity continua to analysis of shear band localization. *Applied Mathematical Modelling*, 31(6):983–1000, 2007.

[71] J. Kiendl, K.-U. Bletzinger, J. Linhard, and R. Wüchner. Isogeometric shell analysis with Kirchhoff–Love elements. *Computer Methods in Applied Mechanics and Engineering*, 198(49):3902–3914, 2009.

[72] I. Kolo, R. K. Abu Al-Rub, and R. L. Sousa. Computational modelling of fracture

propagation in rocks using a coupled elastic-plasticity-damage model. *Mathematical Problems in Engineering*, 2016, 2016.

[73] I. Kolo, R. K. Abu Al-Rub, R. L. Sousa, M. Sassi, and M. Sirat. Numerical modelling of fold-related fractures. In *13th ISRM International Congress of Rock Mechanics*. International Society for Rock Mechanics and Rock Engineering, 2015.

[74] I. Kolo, H. Askes, and R. de Borst. Convergence analysis of Laplacian-based gradient elasticity in an isogeometric framework. *Finite Elements in Analysis and Design*, 135:56–67, 2017.

[75] I. Kolo, H. Askes, and R. de Borst. Higher-order gradient continua: An isogeometric approach. In *Proceedings of the 25th Conference on Computational Mechanics UKACM 2017*, pages 122–125. UKACM, 2017.

[76] I. Kolo, L. Chen, and R. de Borst. Strain-gradient continua with hierarchical refinement of NURBS. Presented at the *6th European Conference on Computational Mechanics (Solids, Structures and Coupled Problems) (ECCM 6) and the 7th European Conference on Computational Fluid Dynamics (ECFD 7), ECCM-ECFD 2018*, Glasgow, 2018.

[77] I. Kolo and R. de Borst. Dispersion and isogeometric analyses of second-order and fourth-order implicit gradient-enhanced plasticity models. *International Journal for Numerical Methods in Engineering*, 114(4):431–453, 2018.

[78] I. Kolo and R. de Borst. An isogeometric analysis approach to gradient-dependent plasticity. *International Journal for Numerical Methods in Engineering*, 113(2):296–310, 2018.

[79] E. Lale, X. Zhou, and G. Cusatis. Isogeometric implementation of high-order microplane model for the simulation of high-order elasticity, softening, and localization. *Journal of Applied Mechanics*, 84(1):011005, 2017.

[80] D. C. C. Lam, F. Yang, A. Chong, J. Wang, and P. Tong. Experiments and theory in strain gradient elasticity. *Journal of the Mechanics and Physics of Solids*, 51(8):1477–1508, 2003.

[81] A. Lasalmonie and J. Strudel. Influence of grain size on the mechanical behaviour of some high strength materials. *Journal of Materials Science*, 21(6):1837–1852, 1986.

[82] M. Lazar and D. Polyzos. On non-singular crack fields in Helmholtz type enriched elasticity theories. *International Journal of Solids and Structures*, 62:1–7, 2015.

[83] T. Liebe, A. Menzel, and P. Steinmann. Theory and numerics of geometrically non-linear gradient plasticity. *International Journal of Engineering Science*, 41(13):1603–1629, 2003.

[84] J. Liu, L. Dedè, J. A. Evans, M. J. Borden, and T. J. Hughes. Isogeometric analysis of the advective Cahn–Hilliard equation: Spinodal decomposition under shear flow. *Journal of Computational Physics*, 242:321–350, 2013.

[85] X. Lu, J.-P. Bardet, and M. Huang. Spectral analysis of nonlocal regularization in two-dimensional finite element models. *International Journal for Numerical and Analytical Methods in Geomechanics*, 36:219–235, 2012.

[86] M. Malagù, E. Benvenuti, C. Duarte, and A. Simone. One-dimensional nonlocal and gradient elasticity: Assessment of high order approximation schemes. *Computer Methods in Applied Mechanics and Engineering*, 275:138–158, 2014.

[87] R. Maranganti and P. Sharma. A novel atomistic approach to determine strain-gradient elasticity constants: Tabulation and comparison for various metals, semiconductors, silica, polymers and the (ir) relevance for nanotechnologies. *Journal of the Mechanics and Physics of Solids*, 55(9):1823–1852, 2007.

[88] T. Matsushima, R. Chambon, and D. Caillerie. Large strain finite element analysis of a local second gradient model: Application to localization. *International Journal for Numerical Methods in Engineering*, 54(4):499–521, 2002.

[89] S. May, J. Vignollet, and R. de Borst. Powell-Sabin B-splines and unstructured standard T-splines for the solution of Kichhoff-Love plate theory using Bézier extraction. *International Journal for Numerical Methods in Engineering*, 107:205–233, 2016.

[90] C. McAuliffe and H. Waisman. Mesh insensitive formulation for initiation and growth of shear bands using mixed finite elements. *Computational Mechanics*, 51(5):807–823, 2013.

[91] A. Menzel and P. Steinmann. On the continuum formulation of higher gradient plasticity for single and polycrystals. *Journal of the Mechanics and Physics of Solids*, 48:1777–1796, 2000.

[92] C. Miehe, F. Aldakheel, and S. Mauthe. Mixed variational principles and robust finite element implementations of gradient plasticity at small strains. *International Journal for Numerical Methods in Engineering*, 94(11):1037–1074, 2013.

[93] R. Mindlin and N. Eshel. On first strain-gradient theories in linear elasticity. *International Journal of Solids and Structures*, 4(1):109–124, 1968.

[94] R. D. Mindlin. Micro-structure in linear elasticity. *Archive for Rational Mechanics and Analysis*, 16(1):51–78, 1964.

[95] T. J. Mitchell, S. Govindjee, and R. L. Taylor. A method for enforcement of Dirichlet boundary conditions in isogeometric analysis. In *Recent Developments and Innovative Applications in Computational Mechanics*, pages 283–293. Springer, 2011.

[96] J. L. Mroginski and G. Etse. A finite element formulation of gradient-based plasticity for porous media with C1 interpolation of internal variables. *Computers and Geotechnics*, 49:7–17, 2013.

[97] H. Mühlhaus and I. Vardoulakis. The thickness of shear bands in granular materials. *Geotechnique*, 37(3):271–283, 1987.

[98] H.-B. Mühlhaus and E. Alfantis. A variational principle for gradient plasticity. *International Journal of Solids and Structures*, 28(7):845–857, 1991.

[99] A. Needleman and M. Ortiz. Effect of boundaries and interfaces on shear-band localization. *International Journal of Solids and Structures*, 28:859–877, 1991.

[100] T. H. A. Nguyen, T. Q. Bui, and S. Hirose. Smoothing gradient damage model with evolving anisotropic nonlocal interactions tailored to low-order finite elements. *Computer Methods in Applied Mechanics and Engineering*, 328:498–541, 2018.

[101] J. Niiranen, S. Khakalo, V. Balobanov, and A. H. Niemi. Variational formulation and isogeometric analysis for fourth-order boundary value problems of gradient-elastic bar and plane strain/stress problems. *Computer Methods in Applied Mechanics and Engineering*, 308:182–211, 2016.

[102] T. Okabe and N. Takeda. Size effect on tensile strength of unidirectional CFRP composites–experiment and simulation. *Composites Science and Technology*, 62(15):2053–2064, 2002.

[103] M. Ortiz and J. B. Martin. Symmetry-preserving return mapping algorithms and incrementally extremal paths: A unification of concepts. *International Journal for Numerical Methods in Engineering*, 28:1839–1854, 1989.

[104] M. Ortiz and J. Quigley IV. Adaptive mesh refinement in strain localization problems. *Computer Methods in Applied Mechanics and Engineering*, 90(1-3):781–804, 1991.

[105] J. Pamin, H. Askes, and R. de Borst. Two gradient plasticity theories discretized with the element-free Galerkin method. *Computer Methods in Applied Mechanics and Engineering*, 192:2377–2403, 2003.

[106] J. K. Pamin. *Gradient-dependent plasticity in numerical simulation of localization phenomena*. TU Delft, Delft University of Technology, 1994.

[107] S.-A. Papanicolopulos, F. Gulib, and A. Marinelli. A novel efficient mixed formulation for strain-gradient models. *International Journal for Numerical Methods in Engineering*, 117(8):926–937, 2019.

[108] S.-A. Papanicolopulos, A. Zervos, and I. Vardoulakis. A three-dimensional C1 finite element for gradient elasticity. *International Journal for Numerical Methods in Engineering*, 77(10):1396–1415, 2009.

[109] J. Peddieson, G. R. Buchanan, and R. P. McNitt. Application of nonlocal continuum models to nanotechnology. *International Journal of Engineering Science*, 41(3):305–312, 2003.

[110] R. Peerlings, R. de Borst, W. Brekelmans, and J. de Vree. Gradient enhanced damage for quasi-brittle materials. *International Journal for Numerical Methods in Engineering*, 39(19):3391–3403, 1996.

[111] R. Peerlings and N. Fleck. Computational evaluation of strain gradient elasticity constants. *International Journal for Multiscale Computational Engineering*, 2(4), 2004.

[112] R. H. J. Peerlings, R. de Borst, W. A. M. Brekelmans, J. H. P. de Vree, and I. Spee. Some observations on localisation in non-local and gradient damage models. *European Journal of Mechanics A: Solids*, 15:937–953, 1996.

[113] R. H. J. Peerlings, M. G. D. Geers, R. de Borst, and W. A. M. Brekelmans. A critical comparison of nonlocal and gradient-enhanced softening continua. *International Journal of Solids and Structures*, 38:7723–7746, 2001.

[114] D. Perić, J. Yu, and D. Owen. On error estimates and adaptivity in elastoplastic solids: Applications to the numerical simulation of strain localization in classical and Cosserat continua. *International Journal for Numerical Methods in Engineering*, 37(8):1351–1379, 1994.

[115] G. Pijaudier-Cabot and A. Huerta. Finite element analysis of bifurcation in nonlocal strain softening solids. *Computer Methods in Applied Mechanics and Engineering*, 90:905–919, 1991.

[116] L. H. Poh and G. Sun. Localizing gradient damage model with decreasing interactions. *International Journal for Numerical Methods in Engineering*, 110(6):503–522, 2017.

[117] L. H. Poh and S. Swaddiwudhipong. Gradient-enhanced softening material models. *International Journal of Plasticity*, 25:2094–2121, 2009.

[118] T. Rabczuk. Computational methods for fracture in brittle and quasi-brittle solids: State-of-the-art review and future perspectives. *ISRN Applied Mathematics*, 2013, 2013.

[119] L. F. Richardson. The approximate arithmetical solution by finite differences of physical problems involving differential equations, with an application to the stresses in a masonry dam. *Philosophical Transactions of the Royal Society of London. Series A*, 210:307–357, 1911.

[120] A. Rodríguez-Ferran, T. Bennett, H. Askes, and E. Tamayo-Mas. A general framework for softening regularisation based on gradient elasticity. *International Journal of Solids and Structures*, 48(9):1382–1394, 2011.

[121] C. Ru and E. Aifantis. A simple approach to solve boundary-value problems in gradient elasticity. *Acta Mechanica*, 101(1-4):59–68, 1993.

[122] J. W. Rudnicki and J. R. Rice. Conditions for the localization of deformation in pressure-sensitive dilatant materials. *Journal of the Mechanics and Physics of Solids*, 23:371–394, 1975.

[123] S. Rudraraju, A. van der Ven, and K. Garikipati. Three-dimensional isogeometric solutions to general boundary value problems of Toupin's gradient elasticity theory at finite strains. *Computer Methods in Applied Mechanics and Engineering*, 278:705–728, 2014.

[124] M. Scott, X. Li, T. Sederberg, and T. Hughes. Local refinement of analysis-suitable T-splines. *Computer Methods in Applied Mechanics and Engineering*, 213:206–222, 2012.

[125] M. A. Scott, M. J. Borden, C. V. Verhoosel, T. W. Sederberg, and T. J. Hughes. Isogeometric finite element data structures based on Bézier extraction of T-splines. *International Journal for Numerical Methods in Engineering*, 88(2):126–156, 2011.

[126] T. W. Sederberg, J. Zheng, A. Bakenov, and A. Nasri. T-splines and T-NURCCs. *ACM Transactions on Graphics*, 22(3):477–484, 2003.

[127] J. Y. Shu, W. E. King, and N. A. Fleck. Finite elements for materials with strain gradient effects. *International Journal for Numerical Methods in Engineering*, 44(3):373–391, 1999.

[128] A. Simone. *Continuous-discontinuous modelling of failure*. TU Delft, Delft University of Technology, 2003.

[129] A. Simone, H. Askes, R. H. J. Peerlings, and L. J. Sluys. Interpolation requirements for implicit gradient-enhanced continuum damage models. *International Journal for Numerical Methods in Biomedical Engineering*, 19:563–572, 2003.

[130] A. Simone, H. Askes, and L. J. Sluys. Incorrect initiation and propagation of failure in non-local and gradient-enhanced media. *International Journal of Solids and Structures*, 41(2):351–363, 2004.

[131] P. Skalka, P. Navrátil, and M. Kotoul. Novel approach to FE solution of crack problems in the Laplacian-based gradient elasticity. *Mechanics of Materials*, 95:28–48, 2016.

[132] L. Sluys. *Wave Propagation, Localisation and Dispersion in Softening Solids*. TU Delft, Delft University of Technology, 1992.

[133] L. J. Sluys and R. de Borst. Dispersive properties of gradient-dependent and rate-dependent media. *Mechanics of Materials*, 18:131–149, 1994.

[134] L. J. Sluys, R. de Borst, and H.-B. Mühlhaus. Wave propagation, localization and dispersion in a gradient-dependent medium. *International Journal of Solids and Structures*, 30:1153–1171, 1993.

[135] J. Stölken and A. Evans. A microbend test method for measuring the plasticity length scale. *Acta Materialia*, 46(14):5109–5115, 1998.

[136] J. Sulem and I. Vardoulakis. *Bifurcation Analysis in Geomechanics*. CRC Press, Glasgow, 2004.

[137] R. A. Toupin. Elastic materials with couple-stresses. *Archive for Rational Mechanics and Analysis*, 11(1):385–414, 1962.

[138] M. R. van Vliet and J. G. van Mier. Size effect of concrete and sandstone. *HERON-ENGLISH EDITION-*, 45(2):91–108, 2000.

[139] C. V. Verhoosel, M. A. Scott, T. J. R. Hughes, and R. de Borst. An isogeometric analysis approach to gradient damage models. *International Journal for Numerical Methods in Engineering*, 86:115–134, 2011.

[140] J. Vignollet, S. May, and R. de Borst. Isogeometric analysis of fluid-saturated porous media including flow in the cracks. *International Journal for Numerical Methods in Engineering*, 108(9):990–1006, 2016.

[141] G. Z. Voyiadjis and R. K. A. Al-Rub. Gradient plasticity theory with a variable length scale parameter. *International Journal of Solids and Structures*, 42(14):3998–4029, 2005.

[142] W. Wang, L. Sluys, and R. de Borst. Viscoplasticity for instabilities due to strain softening and strain-rate softening. *International Journal for Numerical Methods in Engineering*, 40(20):3839–3864, 1997.

[143] X.-B. Wang. Adiabatic shear localization for steels based on Johnson-Cook model and second- and fourth-order gradient plasticity models. *Journal of Iron and Steel Research, International*, 14:56–61, 2007.

[144] G. B. Whitham. *Linear and Nonlinear Waves*. John Wiley & Sons, New York, 1974.

[145] Y. Yang and A. Misra. Higher-order stress-strain theory for damage modeling implemented in an element-free Galerkin formulation. *CMES-Computer Modeling in Engineering & Sciences*, 64(1):1–36, 2010.

[146] A. Zervos. Finite elements for elasticity with microstructure and gradient elasticity. *International Journal for Numerical Methods in Engineering*, 73(4):564–595, 2008.

[147] A. Zervos, S.-A. Papanicolopulos, and I. Vardoulakis. Two finite-element discretizations for gradient elasticity. *Journal of Engineering Mechanics*, 135(3):203–213, 2009.

[148] Q. Zhang, W. Zhang, G. Xie, D. Louzguine-Luzgin, and A. Inoue. Stable flowing of localized shear bands in soft bulk metallic glasses. *Acta Materialia*, 58(3):904–909, 2010.

[149] X. Zhou and J. Lu. NURBS-based Galerkin method and application to skeletal muscle modeling. In *Proceedings of the 2005 ACM Symposium on Solid and Physical Modeling*, SPM '05, pages 71–78, New York, NY, USA, 2005. ACM.

[150] J. Zhu, Z. Taylor, and O. Zienkiewicz. *The Finite Element Method: Its Basis and Fundamentals*. Butterworth-Heinemann, Oxford, 7 edition, 2013.

[151] O. C. Zienkiewicz and J. Z. Zhu. A simple error estimator and adaptive procedure for practical engineerng analysis. *International Journal for Numerical Methods in Engineering*, 24(2):337–357, 1987.